Advanced Techniques for Target Discrimination Using Laser Speckle

Lyle G. Shirley, Emory D. Ariel, Gregory R. Hallerman, Harold C. Payson, and John R. Vivilecchia

A new high-resolution imaging technique known as *wavelength decorrelation* is demonstrated in the laboratory for measuring target shape and estimating surface-scattering properties. In these demonstrations, the target is flood illuminated with a frequency-scanning Ti:sapphire ring laser. As the laser frequency changes, the speckle pattern in the backscattered light appears to boil; the time-varying intensity at a point in this pattern carries information about the target's range-resolved laser radar cross section $U(z)$. A range resolution of better than 1 mm is demonstrated. A theoretical analysis of wavelength decorrelation is also presented, including the mathematical framework for predicting wavelength-decorrelation signatures. An additional technique known as *speckle tracking* is described for measuring a target's angular dynamics.

THE LASER SPECKLE LABORATORY at Lincoln Laboratory was established in 1990 to study high-resolution discrimination techniques based on laser speckle. These techniques allow us to obtain information about the size, shape, surface-scattering properties, and angular dynamics of a distant target. In particular, we can determine the target's range-resolved laser radar cross section with a range resolution better than 1 mm. (For comparison, the ALCOR K_a-band imaging radar has a range resolution of 25 cm [1].) We can also measure the target's projected spin axis to an accuracy better than $\pm 0.1°$, which allows us to estimate the target's angular dynamics by observing how the projected spin axis changes with time. Though still in the developmental stage, laser-speckle technology appears to offer greater discrimination capabilities than are currently attainable with other techniques.

Figure 1 is a schematic diagram of a laser radar system for observing speckle. A beam of light from a laser transmitter illuminates the target. Because the surface of the target is rough on the scale of the wavelength of light, large phase irregularities occur in the backscattered light coming from different scattering regions. Interference between the various contributions to the optical field produces a speckle pattern at the receiver. Thus speckle is inherent in laser radar measurements.

In the past, speckle has usually been considered a nuisance (e.g., it degrades the target images obtained when conventional microwave-radar imaging techniques such as range-Doppler imaging are applied to laser radars). However, the short wavelength of laser radars, which causes speckle, also results in important advantages over much longer-wavelength microwave radars. For example, the higher carrier frequency of a laser radar has the potential for extremely large frequency modulations, which in turn allow for high range resolutions. Another advantage is low beam divergence, which results in high angular resolution as well as the capability to place more of the transmitted power on a distant target.

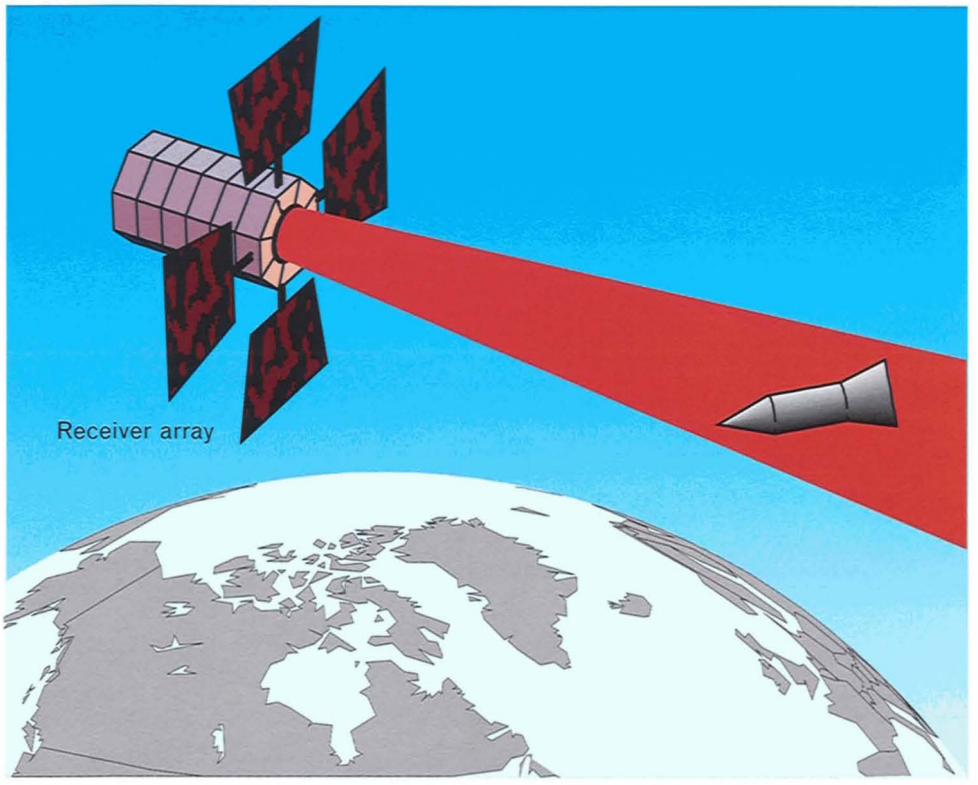

FIGURE 1. Schematic diagram of a laser radar system for observing speckle. Variations in the speckle intensity at the receiver plane carry information about the target's physical characteristics.

Because laser radars have the potential to provide a level of target detail unattainable through other techniques, and because speckle is inherent in the return signal from laser radars, we are led to take a more positive attitude toward speckle in our work. Rather than trying to eliminate it, we treat it as the signal, and we ask the question "What information does speckle carry about the scattering object?" To answer this question, we consider three general properties of speckle: (1) the spatial structure of the speckle pattern at the receiver, (2) the wavelength dependence of speckle associated with changing the operating frequency, or wavelength, of the laser, and (3) the effect on the speckle pattern of a translating or rotating target. The dependence of speckle on these three parameters provides us with three associated techniques for obtaining target information. Figure 2 illustrates these techniques, which are known as *imaging correlography*, *wavelength decorrelation*, and *speckle tracking*.

Imaging correlography constructs images of the target from spatial measurements of backscattered (non-imaged) speckle intensity patterns [2–5]. This technique has produced rough reconstructions of target images. Although we have concentrated our efforts at the Laser Speckle Laboratory on the other two methods, we discuss the basic principles for imaging correlography in the section entitled "Spatial Properties of Speckle." An understanding of these spatial properties will be useful in the discussions of wavelength decorrelation and speckle tracking that follow.

Researchers have known for nearly two decades that the wavelength dependence of speckle carries information about the physical properties of a target [6–19]. The contributions of the Laser Speckle Laboratory in this area have been to (1) express this relation in a simple and intuitive form, (2) develop methods for predicting target signatures, (3) perform the first wavelength-decorrelation measurements of range-resolved laser radar cross section, and (4) continue to develop and refine the wavelength-decorrelation measurement technique in the laboratory.

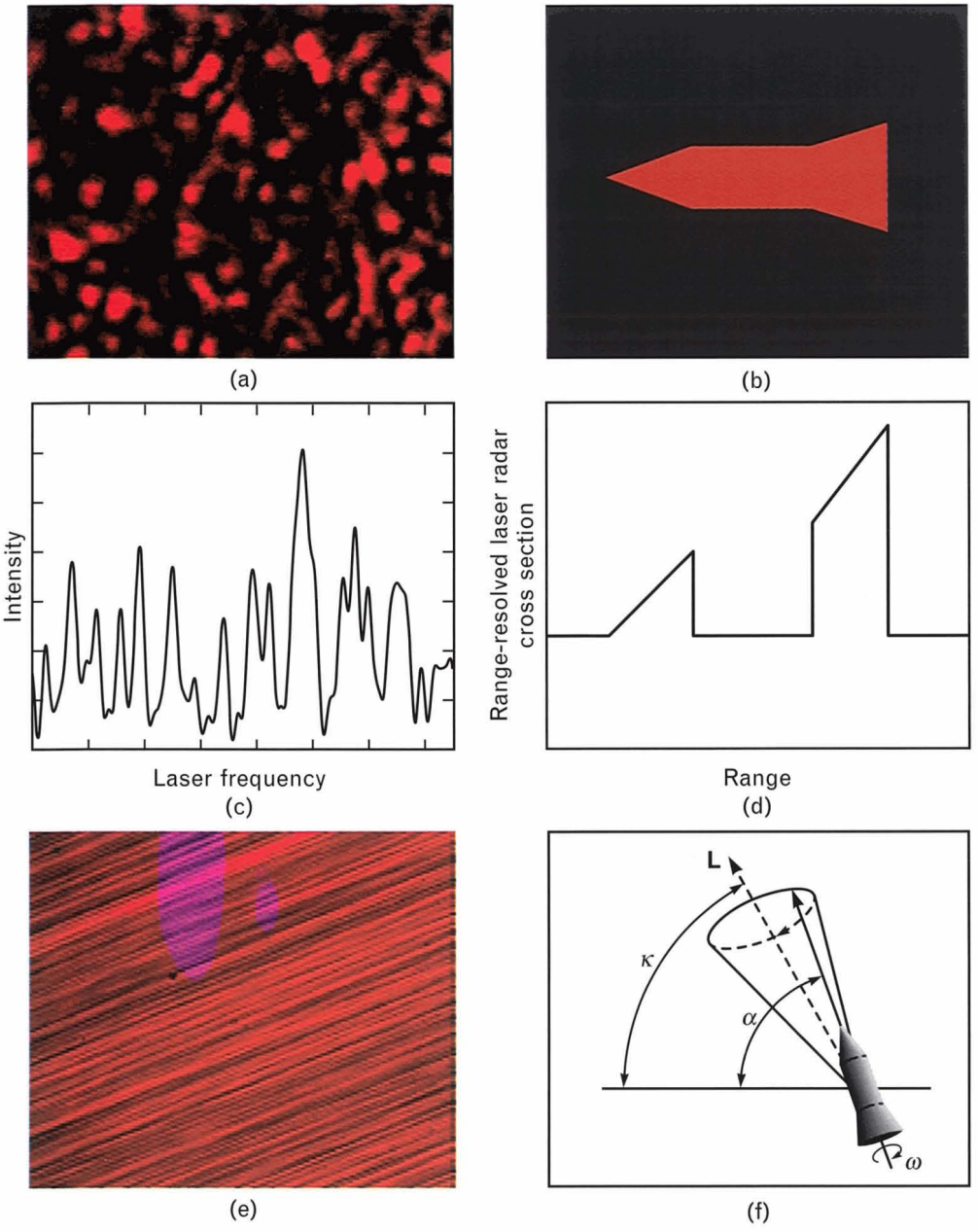

FIGURE 2. Three methods for obtaining target information from speckle intensity. *Imaging correlography* relates the statistics of the (a) speckle pattern to the (b) brightness distribution function of the target. *Wavelength decorrelation* relates the (c) fluctuations in speckle intensity resulting from changing the laser frequency to the (d) range-resolved laser radar cross section of the target. *Speckle tracking* utilizes (e) speckle motion to extract information about (f) angular target dynamics.

In the wavelength-decorrelation technique, the target is flood illuminated with a laser beam whose optical frequency is scanned in time. The associated fluctuations of the speckle intensity in the backscattered light are analyzed to yield information about the target's range-resolved laser radar cross section $U(z)$. The section entitled "Laser Radar Cross Section and Range-Resolved Laser Radar Cross Section" describes how the range-resolved laser radar cross section $U(z)$ and the laser radar cross section σ can be

calculated, given the shape of the target and a description of its surface-scattering properties.

Theoretical aspects of wavelength decorrelation are treated in the section entitled "Theory for Wavelength Decorrelation." The discussion begins with a derivation of the fundamental relation between the spectral density of the fluctuating speckle intensity and the autocorrelation function of the range-resolved laser radar cross section $U(z)$ of the target. Next, a random-process representation of the speckle signal is developed for the purpose of simplifying further statistical analysis of the wavelength-decorrelation technique. This random-process representation is then used to analyze coherent detection and bispectral signal processing of the speckle intensity, both of which provide a measurement of $U(z)$, not just the autocorrelation function of $U(z)$.

In the section entitled "Wavelength-Decorrelation Measurements," we reintroduce the fundamental concepts of wavelength decorrelation from a laboratory point of view and confirm the theoretical results. We demonstrate submillimeter range resolution and discuss some of the potential applications of wavelength decorrelation in target discrimination.

The speckle-tracking technique utilizes the fact that the speckle pattern at the receiver shifts as the target rotates. A spinning target produces a speckle pattern that rotates around the spin axis of the object (for small rotation angles). By observing how the direction and the speed of the speckle motion change with time, we can learn about the angular dynamics of a target [5, 20–24]. In the section entitled "Speckle Tracking" we introduce three methods for measuring the speckle motion; these methods are known as *spatial cross correlation*, *speckle streaking*, and *temporal cross correlation*.

In spatial cross correlation, two speckle patterns are acquired at the same location but separated by a time delay. The cross-correlation peak of these two frames indicates the direction and rate of speckle motion. With speckle streaking, the image of the speckle pattern is taken over a long exposure time compared with the time it takes a speckle lobe to sweep across the detector array. The long exposure produces a streaked pattern, and the direction of the streaks is perpendicular to the projected spin axis of the target. In temporal cross correlation, the time-varying signal at pairs of detectors is cross correlated. The advantage of the temporal method is that it can be implemented with as few as two detector elements. The section on speckle tracking also gives information on the dynamics of free-body motion and mechanical devices for simulating this motion.

Finally, at the end of the article we summarize results obtained to date and make recommendations for further development.

Spatial Properties of Speckle

The spatial structure of laser speckle is readily observed. Because speckle is an interference phenomenon between the contributions to the field that arise from different regions of the scattering surface, the exact detail of the speckle pattern is related to the microscopic structure of the surface. Usually we are not interested in microscopic surface detail but rather in the underlying shape of the object and in its general surface-scattering properties. Therefore, in this article we concentrate on the statistical properties of speckle rather than the details of specific speckle patterns.

Transverse Structure

Let us explore the relation between the physical properties of the scatterer and the transverse size and shape of the speckle pattern. A scalar treatment of the optical field is sufficient for these purposes. For simplicity, we begin by considering the speckle pattern in the far field of a rough surface having an underlying planar shape. If we assume that the illuminating laser beam is monochromatic with a wavelength λ, then the associated wave number k is $2\pi/\lambda$ and the optical frequency ν is c/λ, where c is the speed of light. Let the rough surface be located around the origin and lie in the x-y plane, as shown in Figure 3. The complex amplitude of the optical field $V(x, y, z)$ in the far field of this scatterer can be expressed in the form

$$V(x, y, z) = \frac{i \exp(-ikR)}{\lambda R} \frac{z}{R} \tilde{V}(f_x, f_y)\Big|_{f_x=-\frac{x}{\lambda R},\, f_y=-\frac{y}{\lambda R}}, \quad (1)$$

where R is the distance from the origin to the field

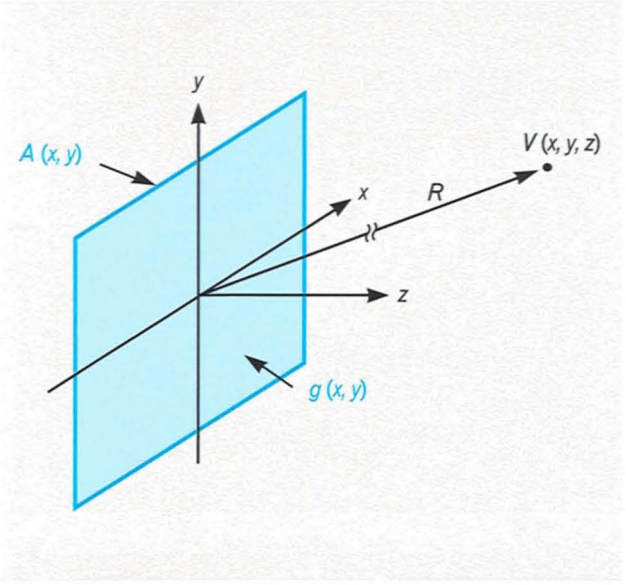

FIGURE 3. Coordinate system for analyzing the spatial properties of speckle.

point, and $\tilde{V}(f_x, f_y)$ is the two-dimensional Fourier transform of the optical field $V(x, y)$ at the x-y plane [25, 26]. A harmonic time dependence of $\exp(i2\pi\nu t)$ has been suppressed in Equation 1. The two-dimensional Fourier transform is defined as

$$\tilde{V}(f_x, f_y) = \int_{-\infty}^{\infty}\int_{-\infty}^{\infty} V(x, y) \exp\left[-i2\pi(f_x x + f_y y)\right] dx\, dy\,.$$

Equation 1 states that the optical far field is proportional to the two-dimensional Fourier transform $\tilde{V}(f_x, f_y)$ of the optical field $V(x, y)$ at the rough surface, and that the spatial-frequency arguments f_x and f_y of the Fourier transform correspond to scattering directions through $f_x = -x/\lambda R$ and $f_y = -y/\lambda R$. Aside from the z/R obliquity factor and the variations with direction associated with the Fourier transform, the far-field complex amplitude behaves as a spherical wave. Thus it is inversely proportional to R and contains a radial phase factor $\exp(-ikR)$. As usual, optical intensity, or irradiance, is proportional to the magnitude-squared of the complex amplitude of the optical field.

The above Fourier-transform relation can be used to explain the angular distribution of scattering and the transverse structure of speckle patterns [9, 27]. By the Fourier-transform relation, surfaces that induce higher spatial-frequency content on the reflected light scatter light into larger angles. Thus the microscopic detail of a rough surface determines the angular distribution of scattered light from the surface. Figure 4 illustrates this fact by comparing the radiation patterns from two types of surfaces. From the photographs (taken with a scanning electron microscope), we see that the etched-glass surface has a smooth height profile compared with the ground-glass surface. Consequently, the ground-glass surface induces a higher spatial-frequency content on the reflected light and scatters light into higher angles.

The transverse structure of the speckle pattern (for example, the average size and the average shape of the individual speckle lobes) depends mainly on the shape of the illuminated portion of the surface and on the overall variation of the intensity profile within the illuminating beam, not on the microscopic structure of the rough surface. This fact can be explained with Fourier transforms by thinking of the complex amplitude $V(x, y)$ of the optical field at $z = 0$ as the product of (1) the complex amplitude $g(x, y)$ that results from uniform illumination of the rough surface at the given angle, and (2) an aperture function $A(x, y)$ that accounts for the actual size and shape of the illuminated portion of the scattering surface and for spatial variations in the strength of the illuminating beam.

By the convolution theorem, the Fourier transform of a product is the convolution of the Fourier transforms of the two factors. This relation can be written in two dimensions as

$$\int_{-\infty}^{\infty}\int_{-\infty}^{\infty} g(x, y)\, A(x, y) \exp\left[-i2\pi(f_x x + f_y y)\right] dx\, dy = \tilde{g}(f_x, f_y) * \tilde{A}(f_x, f_y)\,,$$

where the asterisk denotes a two-dimensional convolution, defined as

$$\tilde{g}(f_x, f_y) * \tilde{A}(f_x, f_y) = \int_{-\infty}^{\infty}\int_{-\infty}^{\infty} \tilde{g}(f_x', f_y')\, \tilde{A}(f_x - f_x', f_y - f_y')\, df_x'\, df_y'\,. \quad (2)$$

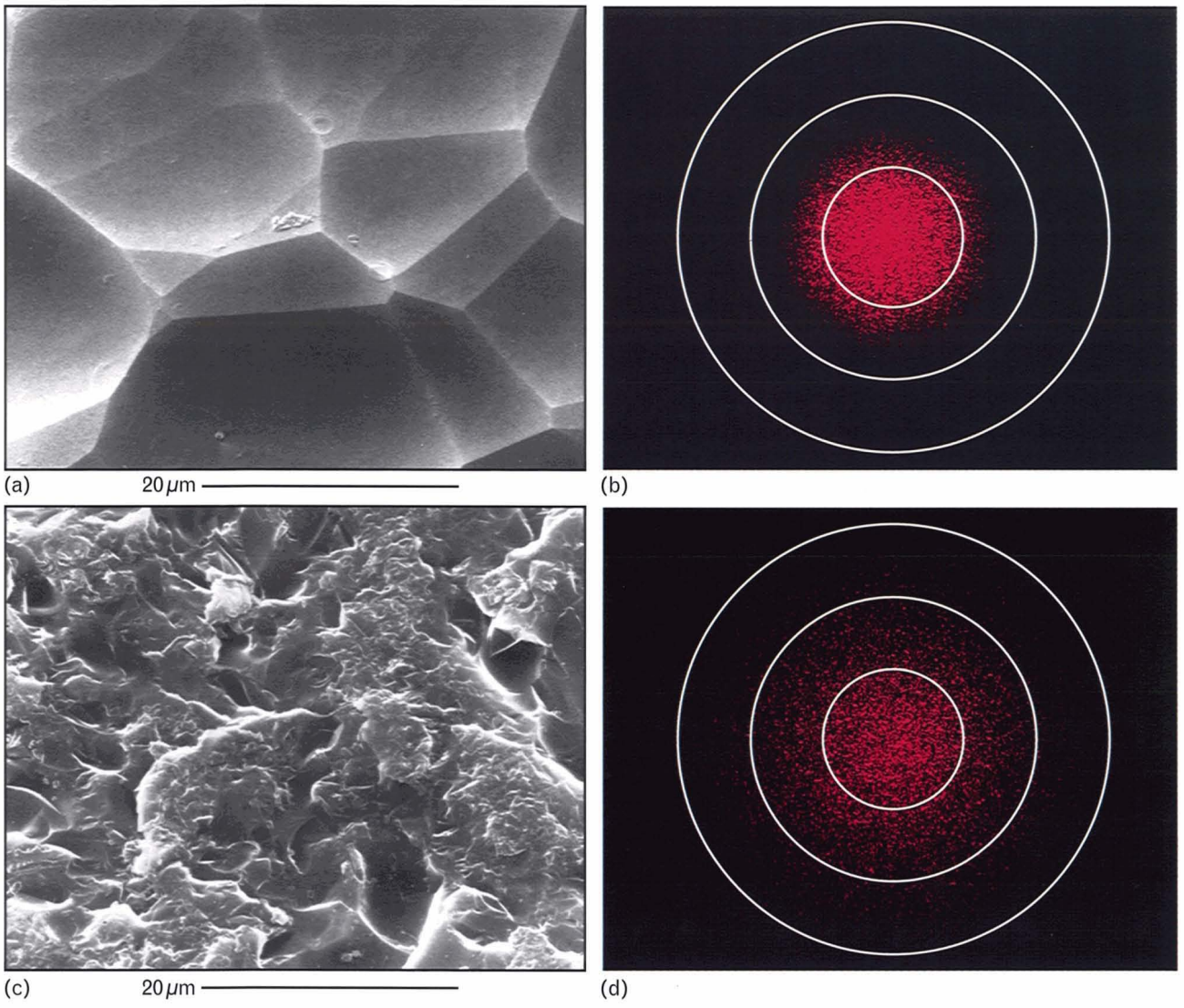

FIGURE 4. Scanning-electron-microscope photographs and associated radiation patterns for two diffusers with markedly different surface structure. (a) The etched-glass diffuser produces (b) a radiation pattern with a narrow angular distribution. (c) The ground-glass diffuser produces (d) a radiation pattern with a much broader angular distribution.

As described above, the Fourier transform of the optical field $g(x, y)$ corresponding to the uniformly illuminated rough surface is a function that is distributed over a wide range of spatial frequencies, or directions, but that varies rapidly locally because of interference. The Fourier transform of the window function $A(x, y)$, however, is a much more localized function of spatial frequencies. It corresponds to the diffraction pattern that would be obtained if the rough surface were replaced by a perfect mirror and illuminated at normal incidence. Because the complex amplitude in the far field is proportional to the two-dimensional Fourier transform of the complex amplitude in the x-y plane, then, by the convolution theorem, the far-field complex amplitude can be written as the convolution of the two Fourier transforms, as shown in Equation 2.

This convolution can also be considered a two-dimensional moving average of the rapidly varying field component $\tilde{g}(f_x, f_y)$ arising from the rough surface. The size and shape of the moving function that determines the region contributing to the average is given by the diffraction pattern $\tilde{A}(f_x, f_y)$ of the aperture function. Therefore, the optical field at a

given value of spatial frequencies is made up of contributions contained within a patch whose size is determined by $\tilde{A}(f_x, f_y)$. If the distance between two spatial-frequency points, or two directions, is smaller than this patch size, then the optical fields at these points are correlated because they contain overlapping contributions. The size and shape of this correlation patch provides a measure of the average size and the average shape of a speckle lobe.

We can use the above principles to obtain a simple rule of thumb for the average speckle size. If D represents the size of the window function along a given direction, then as a result of the Fourier-transform relation, the average speckle size $d_\perp$ in this direction is given by $d_\perp = \lambda R/D$. We see that the speckle size is proportional to the wavelength and the propagation distance, but inversely proportional to the aperture size. This relation is a basic and well-known result in related fields. For example, an antenna array with a longer baseline will have a more localized central lobe.

The above expression for the average speckle size $d_\perp$ also applies to nonplanar objects if we interpret D as the transverse object size. Consequently, if the object is elongated in one direction, the speckle is elongated in the other direction, and the statistics of the speckle pattern not only provide a measure of the size of the object but also carry information about its transverse shape. The basic physical quantity associated with the speckle shape is the brightness distribution function $B(x, y)$ of the object; this function is essentially the two-dimensional unspeckled image of the object for the given aspect angle. For a planar object, the illumination and observation angles are nearly constant over the entire surface. Hence the value of $B(x, y)$ at a particular point is simply proportional to the irradiance, or power per unit area, incident on the object at that point. Because the irradiance is obtained by squaring the magnitude of the aperture function, $B(x, y)$ is proportional to the magnitude-squared of $A(x, y)$.

For a three-dimensional object, the situation is more complicated. Here the aperture function is a projection onto the x-y plane, and the illumination and observation angles on the surface of the target vary as a function of position. This variation in angle affects the magnitude of $B(x, y)$ through the angular dependence of the surface scattering (which is determined by the statistical properties associated with the microscopic surface detail). Although the magnitude of $B(x, y)$ is affected by the microscopic surface details, the general size and shape of $B(x, y)$ is determined by the object's size and shape.

The following section on laser radar-cross-section calculations describes more fully the manner in which the angular distribution associated with the surface roughness of the object enters into speckle calculations. Basically, the surface roughness is accounted for through the bidirectional reflectance distribution function (BRDF) of the surface material. This separation of the underlying surface shape from the microscopic details of the surface allows for simple and intuitive calculations of target signatures.

Figure 5 shows the relation between the speckle shape and the brightness distribution function for three different objects. For the triconic, the individual speckles are elongated in the direction perpendicular to the axis of the triconic. For the sphere, the speckles appear to wrap around one another like worms in a bucket. No direction is preferred, and the speckle shape is symmetric on average. For the ring, the individual speckles are slightly elongated but with random orientations. We can define the average speckle size mathematically by taking the two-dimensional autocorrelation function of the speckle pattern, which is displayed at the bottom of the figure for the three different objects. (Actually, we show the average of the autocorrelation for forty separate realizations of the speckle pattern for each object. The different realizations are obtained by rotating the object slightly.) Note that the autocorrelation function of the elongated speckle from the triconic is also elongated and that the autocorrelation functions of the rotationally symmetric objects are rotationally symmetric.

We can investigate the relation between the speckle shape and the brightness distribution function further by continuing our discussion on Fourier transforms. The quantity we measure in the laboratory is the intensity of the speckle pattern, which is proportional to the magnitude-squared of the complex amplitude of the optical field. If we represent the intensity pattern as a function of spatial-frequency

coordinates and ignore proportionality constants, then by squaring Equation 1 we can represent the intensity as the square of the magnitude of $\tilde{V}(f_x, f_y)$.

By the autocorrelation theorem, the inverse Fourier transform of this magnitude-squared is the autocorrelation function $R_V(x, y)$ of the field $V(x, y)$ at the x-y plane; i.e.,

$$\int_{-\infty}^{\infty}\int_{-\infty}^{\infty}\left|\tilde{V}(f_x, f_y)\right|^2 \exp\left[i2\pi(f_x x + f_y y)\right] df_x\, df_y = R_V(x, y)\,, \tag{3}$$

where the autocorrelation function is defined as

$$R_V(x, y) = \int_{-\infty}^{\infty}\int_{-\infty}^{\infty} V^*(x', y')\, V(x + x', y + y')\, dx'\, dy'\,. \tag{4}$$

Thus by measuring the optical intensity as a function of spatial frequencies and inverse Fourier transforming, we could in principle estimate the two-dimensional autocorrelation function of the complex amplitude of the optical field at the x-y plane. Because of the large phase fluctuations induced by the surface roughness, this optical field oscillates rapidly and has zero mean. Consequently, the autocorrelation function also oscillates rapidly. Averaging the autocorrelation function would not help because the average would vanish, except in the neighborhood of the origin. There is insufficient information to recover the complex amplitude of the optical field from its autocorrelation function.

Rather than attempting to reconstruct the complex amplitude of the field, we can try to reconstruct the brightness distribution function (the magnitude-squared of the aperture function in our planar-object illustration). Thus we would like to relate the intensity of the speckle pattern to $B(x, y)$. To accomplish this goal, the next step is to square the magnitude of the Fourier transform in Equation 3 to obtain a positive function. This step provides a speckled estimate of the two-dimensional spectral density of the speckle pattern. Ensemble averaging now reduces the speckle fluctuations without averaging out the desired signal. We can show that this ensemble-averaged spectral density provides the autocorrelation function of the brightness distribution function $B(x, y)$, plus a dc spike [2]. The spike can be eliminated by subtracting the dc component of the speckle intensity before Fourier transforming.

The relation between the spectral density of the speckle pattern and the autocorrelation of the brightness distribution function forms the basis for imaging correlography. By definition, the spectral density is an ensemble average over an infinite number of realizations of the speckle pattern. In practice, our estimate of the spectral density improves as we take more averages. Figure 6 shows estimates of the spectral density for the triconic, the sphere, and the ring pictured in Figure 5. We use the same forty realizations of the speckle pattern for each object that we used to calculate the autocorrelation functions in Figure 5. Note that the estimate of the spectral density is quite jagged, even for forty averages, but that the autocorrelation functions are smooth.

Again, we can use Fourier transforms to help explain this phenomenon. By the autocorrelation theorem, the unaveraged autocorrelation and the unaveraged spectral density for each speckle frame form a two-dimensional Fourier-transform pair. Because Fourier transforms are linear, the averaged autocorrelation, shown in Figure 5, and the averaged spectral density, shown in Figure 6, also form a Fourier-transform pair. The autocorrelation function tends to be smooth because the speckle pattern from which it is calculated is bandlimited, i.e., varies smoothly. Relatively large errors in the estimate of the autocorrelation, however, occur at large spatial offsets. By the Fourier-transform relation, these errors correspond to rapid variations, or high-frequency noise, in the spectral-density curves. As a general rule, the magnitude of the fluctuations in the estimate of the spectral density is inversely proportional to the square root of the number of averages. Therefore, many realizations of the speckle pattern are needed to obtain a smooth spectral density. This need for many measurements of a two-dimensional speckle pattern can pose a problem in implementing imaging correlography.

The box entitled "Autocorrelation Functions" presents a graphical interpretation of the autocorrelation

function. Figure B in this box is a plot of the theoretical autocorrelation function for the brightness distribution function of a ring. This result agrees in general shape with the measurement presented in Figure 6(c). Figure C is a plot of the theoretical outline of the autocorrelation function of a triconic. It agrees in shape with the measured result given in Figure 6(d).

As a consequence of the autocorrelation theorem,

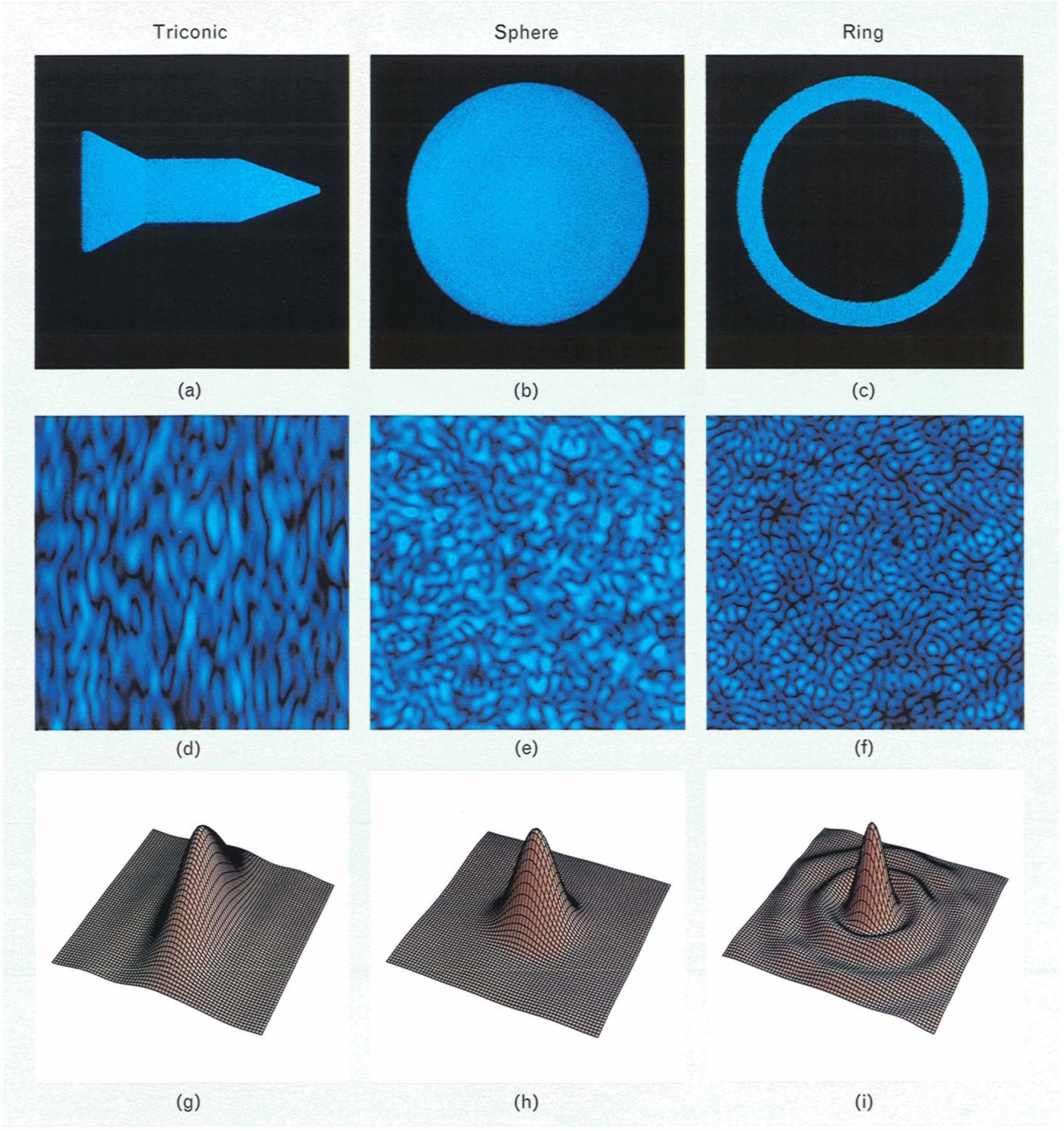

FIGURE 5. Effect of object shape on speckle patterns: brightness distribution functions for (a) a 2.5-cm-long triconic, (b) a 2.5-cm-diameter sphere, and (c) a ring with an outer diameter of 2.5 cm and an inner diameter of 2.0 cm; their corresponding speckle patterns are shown in (d), (e), and (f); the ensemble-averaged autocorrelation functions (forty averages) of the speckle patterns are shown in (g), (h), and (i), respectively.

the autocorrelation function of the brightness distribution function $B(x, y)$ contains the same information as the magnitude-squared of the Fourier transform of $B(x, y)$. In imaging correlography, the phase is recovered through two-dimensional phase retrieval, allowing $B(x, y)$ to be reconstructed in theory.

Thus far we have presented an overview of the transverse structure of speckle and described the basic principle for imaging correlography. In doing so we have demonstrated the important role that Fourier transforms play in the theory of speckle. The results for imaging correlography closely parallel the results

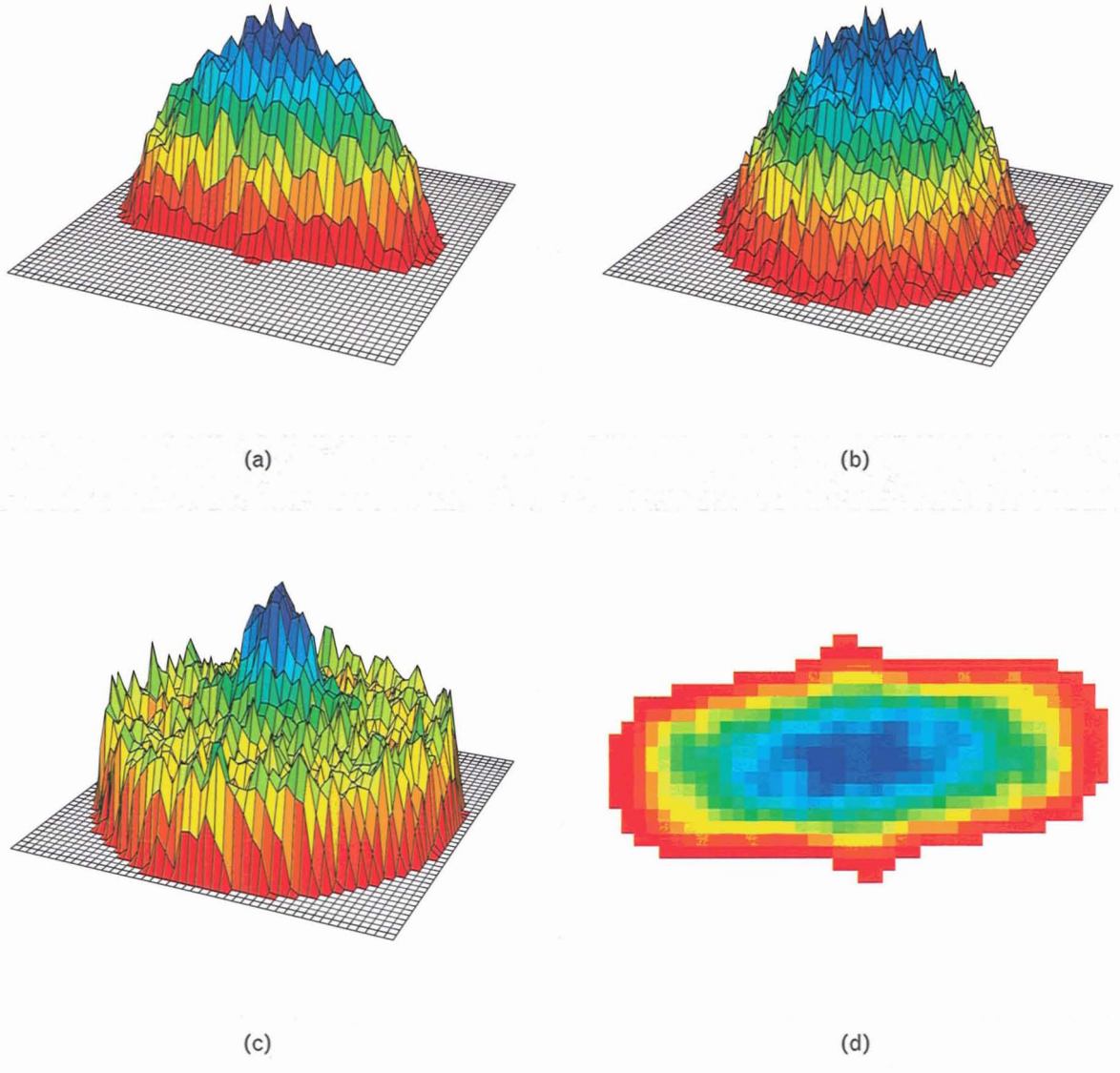

FIGURE 6. Estimated spectral density (forty averages) of the speckle patterns associated with the three objects shown in Figure 5: (a) triconic, (b) sphere, and (c) ring. A top view of part *a* is given in (d). Theoretically, these spectral-density plots correspond to the autocorrelation function of the brightness distribution functions shown in Figures 5(a) through 5(c), respectively.

for wavelength decorrelation. We present a careful theoretical analysis of wavelength decorrelation in the section entitled "Theory for Wavelength Decorrelation."

Longitudinal Structure

A speckle pattern also has longitudinal structure. From the above discussion, once the observation point is in the far field, the intensity of the speckle pattern does not change in the radial direction, except for falling off as $1/R^2$. In this section we investigate how the longitudinal structure of a speckle pattern varies with distance from the scattering object, without assuming that the field point is in the far field.

We illustrate the variation in longitudinal structure through the computer-simulated speckle pattern displayed in Figure 7(a). The data are generated by adding the field contributions from a linear array of point-scatterers. The array is 20λ in length and the spacing between points is $\lambda/4$. The scatterers are randomly phased by using a uniform distribution over 2π radians. The intensity is calculated on a square grid by summing the field contributions from the individual point-scatterers and squaring the magnitude. The grid lies in the plane defined by the linear scattering array and the longitudinal direction. The size of the sampled area is 40λ in the transverse direction and 50λ in the longitudinal direction. For the purpose of visualization, the speckle intensity is normalized by dividing by the ensemble-averaged intensity value at each grid point. This normalization compensates for the decrease in intensity with distance.

Near the scatterer the speckles are small in both directions, but not smaller than the wavelength λ. Note that the rule of thumb for the average speckle size $d_\perp$ applies well into the near field, as the transverse speckle size appears to increase linearly with distance from the scattering object. The speckles also become elongated rapidly in the radial direction. A rule of thumb for estimating the longitudinal speckle size $d_{||}$ in the Fresnel zone is given in the literature [9, 28]; namely, $d_{||} = 4\lambda R^2/D^2$. Thus the longitudinal speckle size grows as the square of the distance R, rather than linearly with R, which accounts for the rapid elongation of the speckles with distance. The transition to the far field occurs at a range of approximately $R = D^2/\lambda$. For this example, $R = 400\lambda$. In Figure 7(b) we show a calculation of the normalized speckle intensity as a function of the logarithm of the distance along a horizontal line passing through the center of the linear scattering array. This curve illustrates the transition to the far field and confirms that

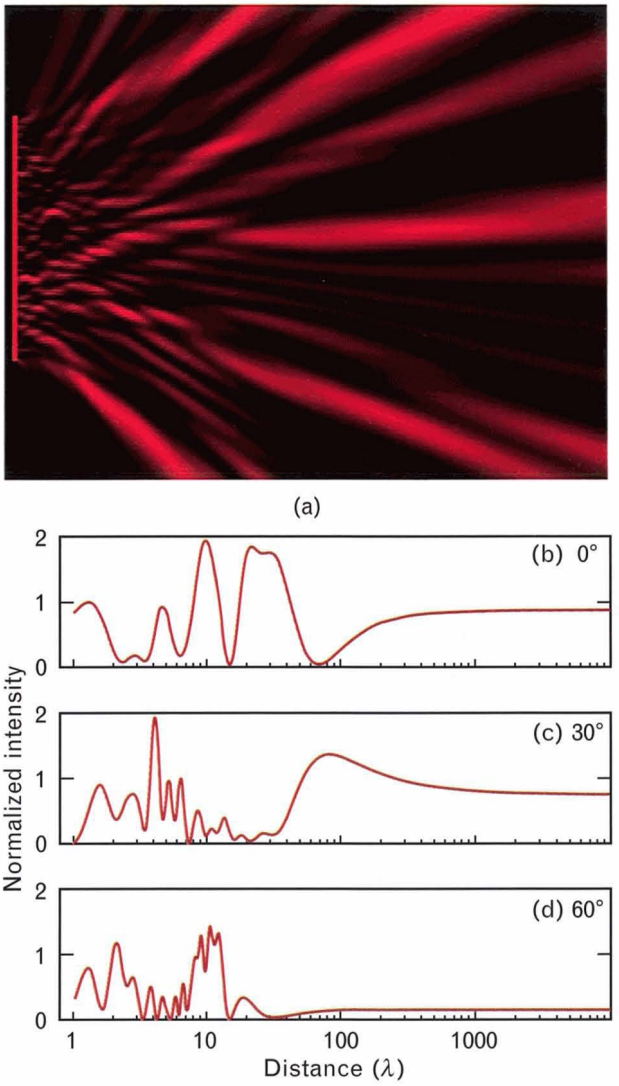

FIGURE 7. Computer-simulated normalized speckle intensity from a 20-wavelength-long linear array of randomly phased point-scatterers: (a) longitudinal slice of the speckle pattern cutting through the linear array; (b) speckle intensity versus logarithm of distance for a horizontal line lying in the longitudinal slice and beginning at the center of the linear array; (c) speckle intensity along a radial line 30° above the horizontal; (d) speckle intensity along a radial line 60° above the horizontal. The speckle intensity is normalized by dividing by the expected value of the intensity at each point.

AUTOCORRELATION FUNCTIONS

BECAUSE AUTOCORRELATION functions play an important role in the theory of speckle, we can often use them to explain target signatures. Let us first consider wavelength decorrelation. In this technique we obtain the autocorrelation function

$$R_U(z) = \int_{-\infty}^{\infty} U(z')\, U(z + z')\, dz'$$

of the target's range-resolved laser radar cross section $U(z)$ by calculating the spectral density of the fluctuations in speckle intensity induced by scanning the laser frequency. We do not need to take the complex conjugate of $U(z')$ in this equation (as we do in the general definition of the autocorrelation function) because the range-resolved laser radar cross section is a real quantity.

Figure A illustrates the calculation of the autocorrelation function pictorially for a triconic illuminated on axis. To calculate the value of the autocorrelation function at a particular range offset z, we multiply the original function $U(z')$ by the shifted function $U(z + z')$ and integrate to find the area under the product curve. This procedure is illustrated for two separate offset values z_a and z_b. The shaded areas represent the magnitude of the autocorrelation function for these two range offsets. Observe that the null in the autocorrelation function occurs because the middle section of the triconic is longer than either of the outer two sections.

In imaging correlography we obtain the autocorrelation function of the target's brightness distribution function $B(x, y)$ by calculating the two-dimensional spectral density of the speckle-intensity pattern. The autocorrelation function of $B(x, y)$ is defined as

$$R_B(x, y) = \int_{-\infty}^{\infty}\int_{-\infty}^{\infty} B(x', y') \times B(x + x', y + y')\, dx'\, dy'. \quad \text{(A)}$$

We plot the autocorrelation function of a ring in Figure B.

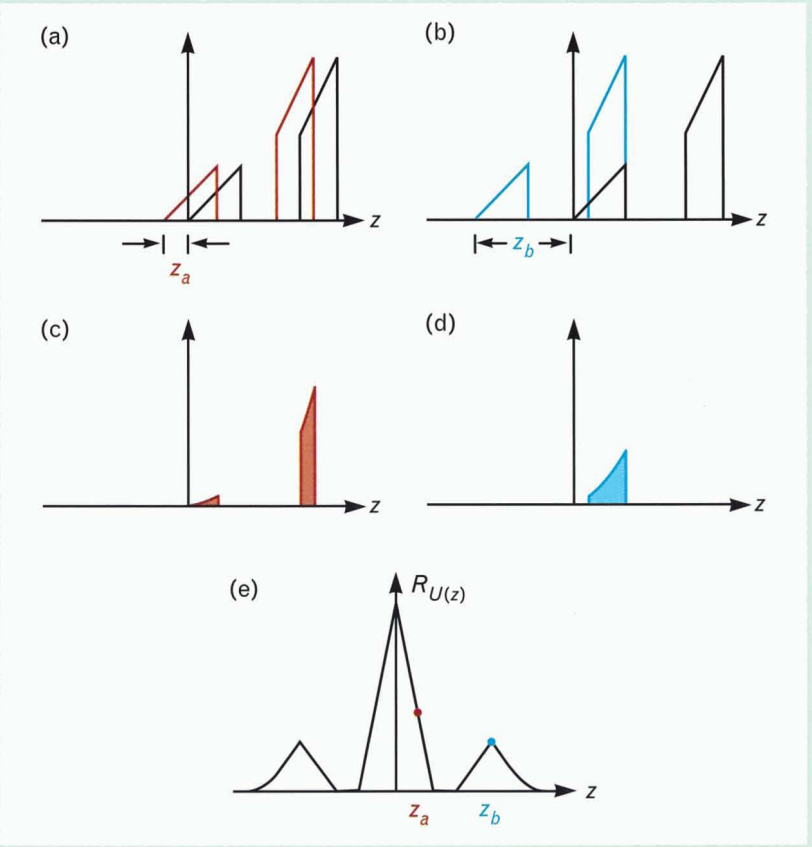

FIGURE A. Pictorial calculation of the autocorrelation function of the range-resolved laser radar cross section of a triconic. The function being autocorrelated is duplicated with the specified value of the range offset and then multiplied by the original function. The area under the resulting product curve corresponds to the value of the autocorrelation function for the given offset value.

The inner diameter of the ring is 80% of its outer diameter, as is the case for the target used in Figure 5. This autocorrelation function agrees in general shape with the experimentally measured autocorrelation function displayed in Figure 6(c).

In Figure C we demonstrate a simple method for determining the outline of the two-dimensional autocorrelation function defined in Equation A. The object in this demonstration is a triconic illuminated from the side. We can determine the outline of the autocorrelation function by sliding the outline of the blue brightness distribution function around the red point and plotting the extreme point, or set of points, of the moving object. The outline shown in Figure C agrees with the outline of the experimentally obtained autocorrelation function for the triconic given in Figure 6(d). In general, a two-dimensional autocorrelation function of a real function is point-symmetric around the origin. The reason for the stronger fourfold symmetry in Figure C is that $B(x, y)$ for the triconic is symmetric around one of the axes.

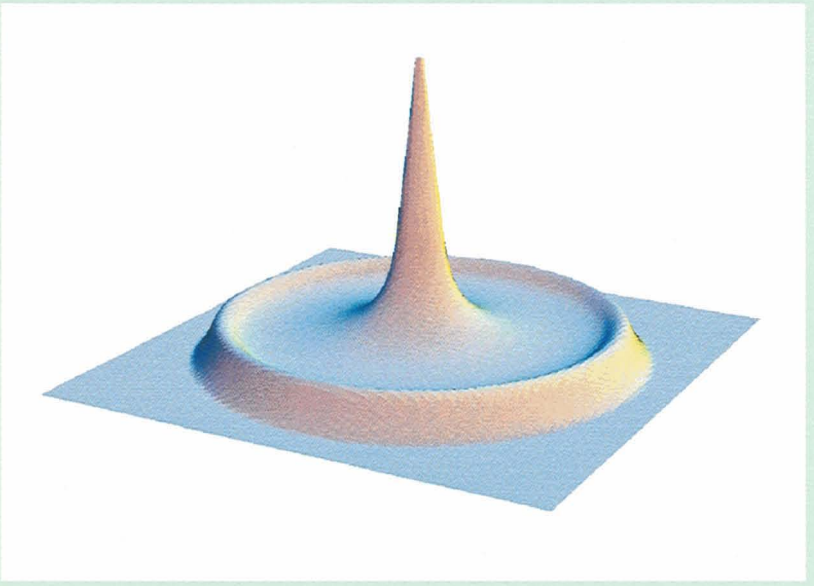

FIGURE B. Autocorrelation function of a ring function having an inner diameter that is 80% of the outer diameter.

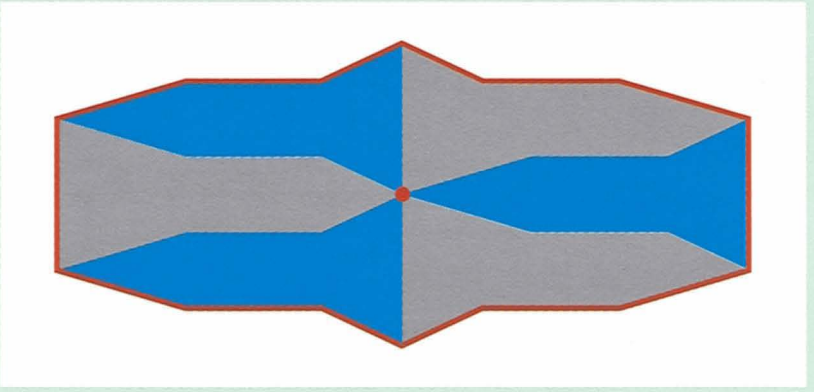

FIGURE C. Outline of the autocorrelation function for the brightness distribution function of a triconic. The outline, shown in red, can be determined by sliding the perimeter of the blue triconic around the red point and plotting the extreme point or points.

the normalized speckle intensity does not fluctuate past this point. In Figures 7(c) and 7(d) we plot similar curves for radial lines making angles of 30° and 60° with respect to the horizontal axis. The transition to the far field occurs more rapidly at these larger angles because the projected length of the scattering array decreases.

To illustrate further the spatial properties of speckle, we show a three-dimensional measured speckle pattern in Figure 8. We obtained this speckle pattern by back-illuminating a ground-glass diffuser with a focused laser beam from a HeNe laser and sampling the resulting speckle pattern with a CCD array. We translated the CCD array in the longitudinal direction between frames and combined the frames into a three-dimensional array representing the speckle intensity as a function of position. The conical region containing the speckle pattern is 300 μm in length and its

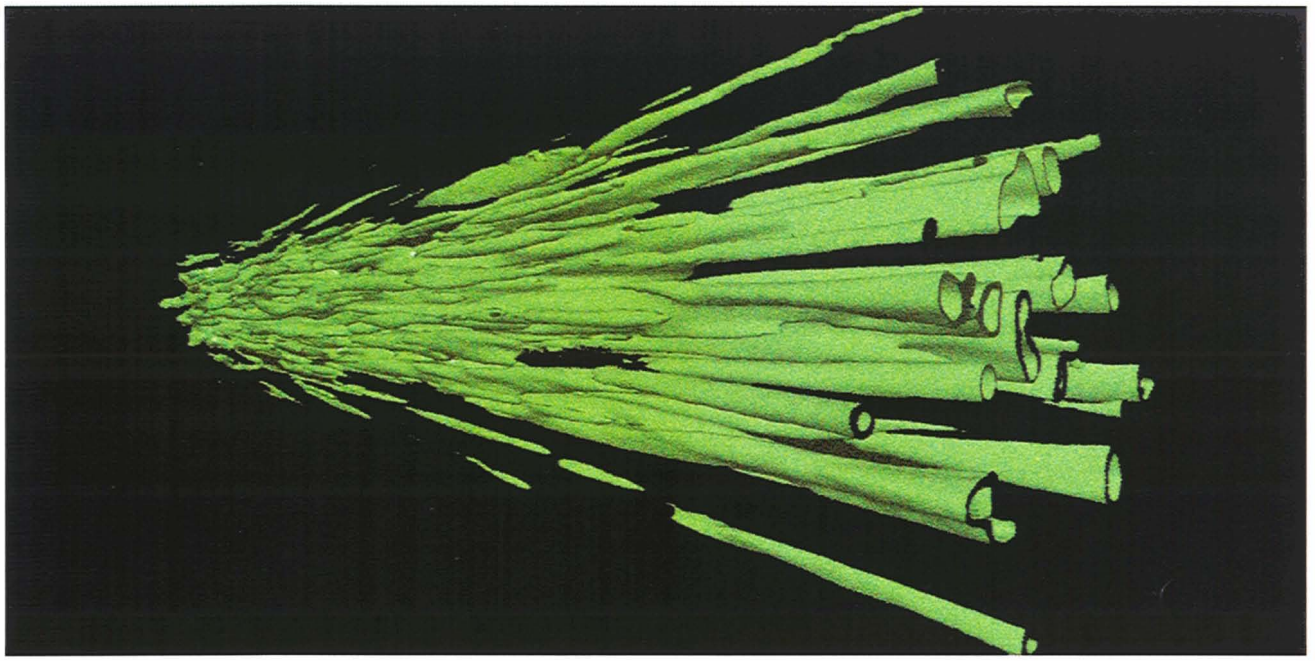

FIGURE 8. Measured three-dimensional speckle pattern from a ground-glass diffuser that is back illuminated by a 25-μm-diameter 0.633-μm-wavelength HeNe laser spot. This image was formed by stacking a series of 150 CCD images of the speckle pattern, with a longitudinal displacement of 2 μm between frames.

diameter increases from 25 μm to 100 μm. We used a microscope objective to magnify the speckle and to image the plane of interest onto the CCD array. To visualize the speckle pattern in three dimensions more easily, we also normalized the intensity (as in Figure 7) and applied a threshold function to convert the speckles to solid objects. As expected, the transverse speckle size increases linearly with radial distance, and the speckle rapidly becomes elongated.

In the above two examples, the transverse size D of the scatterer was chosen to be small so that a small number of speckles would be present for visualization purposes. (Observe that approximately $D/\lambda = 20$ speckles are at a given value of range in Figure 7[a]. Thus $(D/\lambda)^2$ is the approximate number of speckles associated with a scatterer.) Let us estimate the speckle size for other situations. In a typical laboratory setup with $D = 5$ cm, $R = 2$ m, and $\lambda = 0.75$ μm, the average transverse speckle size at the receiver plane is $d_\perp = 30$ μm. At this range we are still not in the far field, which occurs at $R = 3300$ m. Therefore, the speckle is still fluctuating in the radial direction; and the longitudinal speckle size is $d_{||} = 4.8$ mm. This relatively slow variation of the speckle pattern with R allows the methods described in the following sections to be applied to targets with longitudinal motion components. In a space-based application, typical parameters might be $D = 1$ m, $R = 100$ km, and $\lambda = 1$ μm, which yields a transverse speckle size of $d_\perp = 10$ cm. The far-zone transition for this set of parameters occurs at approximately $R = 1000$ km, and the longitudinal speckle size at $R = 100$ km is $d_{||} = 40$ km.

Laser Radar Cross Section and Range-Resolved Laser Radar Cross Section

In this section we describe the fundamental relations involved in the calculation of an object's laser radar cross section σ and its range-resolved laser radar cross section $U(z)$ [14]. These quantities are fundamentally important in understanding and interpreting radar signatures. The laser radar cross section σ determines the strength of the return signal, while the range-resolved laser radar cross section $U(z)$ determines how much of the return signal comes from each value of range z. Therefore, $U(z)$ contains information about the size, shape, and surface-scattering properties of the object. Because $U(z)$ can be measured by the wavelength-decorrelation method, we

are interested in relating it to the physical properties of a target. In what follows, we build a theoretical framework and point out similarities in the methodology for calculating $U(z)$ and σ. We then apply this methodology to the calculation of $U(z)$ and σ for basic geometrical shapes.

Definitions

Because of speckle, there is a basic distinction between microwave cross sections and laser radar cross sections. To smooth out the large fluctuations in intensity caused by the speckle, we define the laser radar cross section as an ensemble-averaged quantity. Hence the usual microwave-radar expression relating the cross section to the irradiance E (power per unit area) at the receiver is modified by placing ensemble-average brackets around the received irradiance

$$\sigma = 4\pi R^2 \frac{\langle E \rangle}{E_0}. \tag{5}$$

The quantity E_0 in Equation 5 is the irradiance of the illuminating beam and R is the distance to the target, as shown in Figure 9. We interpret the laser radar cross section σ as the cross-sectional area of a hypothetical isotropic scatterer that would produce the same averaged irradiance at the receiver as the actual scatterer. An isotropic scatterer is one that scatters the incident light uniformly into 4π steradians.

Because the laser wavelength is small compared to the object size and to any feature of interest on the object, the scattering can be treated as a localized phenomenon. This fact simplifies the calculation of σ. In addition, because σ is defined as an ensemble-averaged quantity and because the surface is rough on a wavelength scale, the interference between the contributions arising from different regions of the surface averages out. Therefore, σ is obtainable by incoherently summing the contributions arising from individual surface patches.

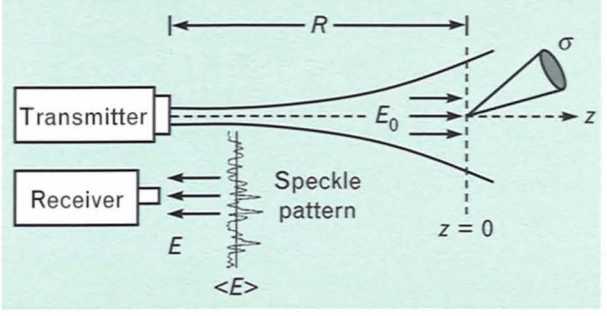

FIGURE 9. The coordinate system used to define laser radar cross section and range-resolved laser radar cross section.

The range-resolved laser radar cross section $U(z)$ is also an ensemble-averaged quantity. Because σ is the incoherent sum of individual localized contributions we can define $U(z)$ as the derivative of the laser radar cross section σ with respect to range:

$$U(z) = \frac{d\sigma}{dz}. \tag{6}$$

Thus $U(z)$ is a density function that quantifies the contributions to the cross section as a function of range. Integrating $U(z)$ over the entire range extent of the object yields σ. Both σ and $U(z)$ are nonnegative functions; $U(z)$ can be infinite at isolated points, as long as the integrated area under the curve is finite. Because σ has dimensions of area, $U(z)$ has dimensions of length. Both quantities depend on the viewing angle.

Method of Calculation

There are two physical properties of the object that affect σ and $U(z)$: the shape of the object and the angular-scattering distribution of its surface materials. We characterize the shape of the object by the function $h_{||}(x, y)$, which represents the height of the object boundaries above the $z = 0$ plane as a function of the Cartesian coordinates x and y lying in this plane. Hence this height function is measured along the direction of illumination and increases with distance from the source. If the function is multivalued, then we use the smallest value because it corresponds to the point closest to the source; the other values are associated with points that are shadowed by the closest point.

The standard radiometric quantity for specifying the angular-scattering distribution is the bidirectional reflectance distribution function (BRDF) [29, 30]. The BRDF describes the scattering of light from a flat surface element as a function of both the illumination direction and the observation direction. Knowledge

of the full BRDF is not necessary in our situation, however, because we have assumed a monostatic radar configuration. Instead, we can use the monostatic reflectance distribution function (MRDF), which is a subset of the BRDF obtained by setting illumination and observation angles equal. By assuming that the surface material has no preferred azimuthal axis, we can write the MRDF as a function of one variable only, the angle of incidence θ. We denote the MRDF by the symbol $f(\theta)$. The local angle of incidence θ varies with position on the surface. It is related to the height function $h_{||}(x, y)$ through

$$\cos\theta = \pm \frac{1}{\sqrt{h_{||_x}^2 + h_{||_y}^2 + 1}}, \tag{7}$$

where the subscripts x and y denote partial derivatives of the height function with respect to these variables. The plus sign is chosen if the surface element points toward the source, and the minus sign is chosen if the surface element points away from the source.

To evaluate the cross section σ, we incoherently sum the contributions arising from individual surface elements. If dA is the area of a given surface element, then the associated contribution to the cross section is

$$d\sigma = 4\pi f(\theta) \cos^2\theta \, dA. \tag{8}$$

This result follows from the definition of cross section and the definition of the BRDF. One of the cosine factors arises from the illumination obliquity factor; the other is associated with the decreased projected area of the element as seen by the detector. The total cross section is obtained by integrating over the entire illuminated surface area. There are two conditions under which a surface patch will not be illuminated: (1) if its surface normal points away from the source, which occurs when $\cos\theta < 0$, or (2) if it is shadowed by some other region of the object. The second condition occurs when $h_{||}$ is multivalued and the given surface patch does not correspond to the lowest value of $h_{||}$. If the object is convex, then all shadowing can be accounted for by applying the $\cos\theta < 0$ rule.

In our situation, we find it more convenient to perform the integration over the projected area $A_\perp$ along the line of sight. If we write the surface-area differential dA in terms of $dA_\perp = dx\, dy = dA \cos\theta$, then one of the cosine factors is eliminated. By summing over the projected area $A_\perp$ of the object, we obtain

$$\sigma = 4\pi \iint_{A_\perp} f(\theta) \cos\theta \, dx \, dy \tag{9}$$

as the cross section for the particular viewing angle.

The assumptions that go into the derivation of Equation 9 limit its use to the calculation of σ for diffusely scattering objects that are large in size compared to the optical wavelength. Contributions to the cross section arising from specular scattering points can be accounted for separately. Also, interactions between different surface elements, such as multiple scattering, are not accounted for. Polarization effects are also ignored in Equation 9, but they could be included by defining a polarization-dependent MRDF and σ.

The basic formula for calculating $U(z)$ is similar in appearance to Equation 9. The only difference is the inclusion of a δ-function within the integral to limit the region of integration to the specified value of range z:

$$U(z) = 4\pi \iint_{A_\perp} f(\theta) \cos\theta \, \delta\left[z - h_{||}(x, y)\right] dx \, dy. \tag{10}$$

Figure 10 illustrates how the δ-function reduces the region of integration to the contour formed by the intersection of the range plane with the boundary of the object. We can check that Equation 10 is valid by substituting it into Equation 6, which yields Equation 9 for σ.

We further illustrate the meaning of Equation 10 by considering two special cases. In the first case, we suppose that the scattering object is a flat plate of area A that is illuminated at normal incidence. Then the height function is constant (say z_0) on this plate, and the object's total cross section is confined to one value of range; i.e., $z = z_0$. Equation 10 is easily evaluated in this case; the δ-function does not depend on the variables of integration and can be removed from the integral, which leaves

$$U(z) = \sigma \, \delta(z - z_0), \tag{11}$$

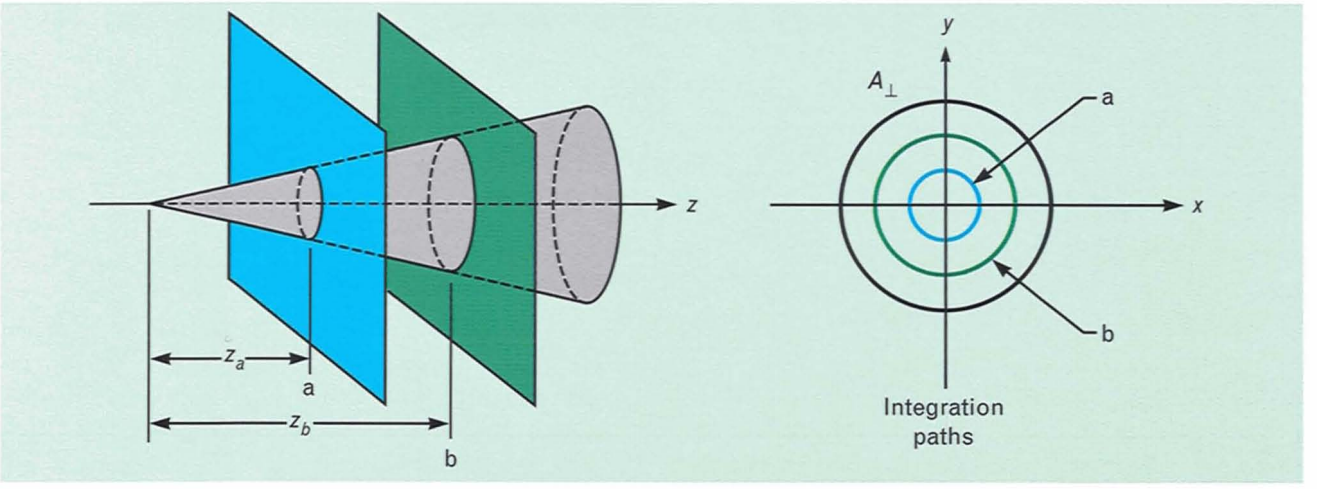

FIGURE 10. The circularly shaped integration paths for calculating the range-resolved laser radar cross section $U(z)$ for a cone illuminated on axis.

where $\sigma = 4\pi f(0)A$ is the cross section of the plate.

In the second case, we exclude any situations covered by Equation 11. Then Equation 10 reduces to a line integral around the contour associated with the given height value of z. We obtain this line integral by changing variables from x and y to z and l, where l is the distance along the integration path. Then $dx\,dy = \cot\theta\; dl\,dz$, and the range integration can be performed by applying the δ-function, which leaves

$$U(z) = 4\pi \int_{\text{contour}} f(\theta) \cos\theta \cot\theta \, dl \,. \qquad (12)$$

Because the height function may have multiple peaks and valleys, more than one contour line may exist for a given value of z.

On-Axis Illumination

We now illustrate the calculation of σ and $U(z)$ for on-axis illumination of axially symmetric objects. Although these calculations are among the simplest to carry out, the results are still important because they apply to a number of common situations and because they illustrate the general behavior of σ and $U(z)$. We consider the laser radar cross section first. In radar measurements the radar is calibrated by using a standard target with a known cross section. The calibration standard for laser radars is typically either a diffuse disk illuminated at normal incidence or a diffuse sphere. Ideally, the surface of the calibration target is Lambertian, which corresponds to an angle-independent MRDF value of $f = 1/\pi$.

As calibration standards, the numerical values of σ for Lambertian spheres and Lambertian disks have special significance. The laser radar cross section of a Lambertian sphere is 8/3 times its projected geometrical cross section. Compare this value to that of the conventional radar cross section of a smooth, perfectly conducting sphere as calculated in the short-wavelength, physical-optics limit [31]; in this situation the cross section is equal to the geometrical cross section of the sphere. The conventional radar cross section of a smooth sphere can be attributed to the neighborhood of the specular point, whereas the laser radar cross section of a diffuse sphere is composed of contributions from the entire illuminated hemisphere. We have distinguished between laser radar cross section and conventional radar cross section to stress that it is not necessary to take the ensemble average when the surface of the object is smooth. The laser radar cross section and the conventional radar cross section, however, are equal in this situation, and we shall not distinguish between the two in the remainder of this discussion.

A Lambertian disk viewed at normal incidence has a laser radar cross section equal to four times its area A. But the laser radar cross section of a smooth, perfectly conducting disk at normal incidence depends on the wavelength λ through the relation $\sigma = 4\pi A^2/\lambda^2$. This strong wavelength dependence is

caused by coherent addition of the specular reflections from the entire surface area of the disk.

The surfaces of a sphere and a disk are examples of two different classes of surfaces, namely, those having curvature in two dimensions and those having no curvature in either dimension. The surface of a cylinder is an example of an intermediate category; its surface has curvature in a single dimension. If we view a smooth, perfectly conducting cylinder normal to its axis, then there is a straight line on the surface where specular reflections occur. The coherent addition of these specular contributions produces a laser radar cross section that is inversely proportional to wavelength; i.e., $\sigma = 2\pi a L^2/\lambda$, where a is the radius of the cylinder and L is its length. Contrast this relation with the wavelength-independent result that $\sigma = 2\pi a L$ for a Lambertian cylinder viewed normal to its axis. In summary of these three situations, except for possible variations of $f(\theta)$ with wavelength, the laser radar cross section of a diffuse object is independent of the wavelength, but the laser radar cross section of a smooth-surfaced object can exhibit a strong wavelength dependence for those viewing angles where there is coherent addition of specular components.

Next we illustrate some elementary calculations of the range-resolved laser radar cross section for axially symmetric objects that are viewed along the axis of symmetry. In these calculations Equation 12 reduces to a simple form. We derive this form by representing the object by a radius function $r(z)$. If $r(z)$ increases monotonically, then each value of z maps into a single value of the angle of incidence θ. Therefore, the quantities that depend on θ can be removed from the integral, and the integration in Equation 12 simply results in the circumference $2\pi r(z)$ of the object for the given range value. Consequently, for axially symmetric objects illuminated along the axis of symmetry, Equation 12 takes the form

$$U(z) = 8\pi^2 r(z)\, f(\theta) \cos\theta \cot\theta . \qquad (13)$$

The angle of incidence θ is related to the radius function $r(z)$ by $\cot\theta = dr/dz$. If $r(z)$ is not a monotonic function, then for certain ranges z there will be more than one value of r corresponding to z. If this is the case then we sum the contributions from the different solutions.

Let us apply Equation 13 to the case of a cone viewed on axis. For a cone half-angle α_c and a cone length equal to L, and with the tip of the cone located at $z = 0$, we obtain

$$U(z) = 8\pi^2 \sin\alpha_c \tan^2\alpha_c\, f(\pi/2 - \alpha_c)\, z \quad \text{for } 0 \le z \le L . \qquad (14)$$

Note that the range-resolved laser radar cross section of the cone increases linearly with range, regardless of the functional form of the MRDF. This result is intuitive because the angle of incidence is constant and the circumference of the cone is proportional to z.

We now calculate the range-resolved laser radar cross section of a sphere. Let the sphere have radius a and be located with its center at $z = 0$. Then Equation 13 reduces to

$$U(z) = \frac{8\pi^2}{a} f\left[\cos^{-1}(-z/a)\right] z^2 \quad \text{for } -a \le z \le 0 . \qquad (15)$$

Observe that $U(z)$ is a segment of a parabola when the surface of the sphere is Lambertian. The parabola has a maximum value of $8\pi a$ at the pole where $z = -a$, and falls to zero at the equator where $z = 0$. Interestingly, the on-axis cone and the Lambertian sphere have range-resolved laser radar cross sections that are linear and quadratic in range, respectively. Figure 11 contains plots of $U(z)$ for a top hat and a cone, each viewed on axis, and a Lambertian sphere. These plots illustrate Equations 11, 14, and 15, respectively.

Off-Axis Illumination

The cross section σ and range-resolved laser radar cross section $U(z)$ vary markedly with viewing angle. This angular dependence can produce distinctive signatures that are useful for identifying and characterizing targets; the capability to predict these signatures can aid in their interpretation. In this section we introduce methods for calculating the angular dependence of σ and $U(z)$.

Although Equation 9 for calculating σ and Equation 10 for calculating $U(z)$ are general results, they are difficult to apply to angle-dependent problems

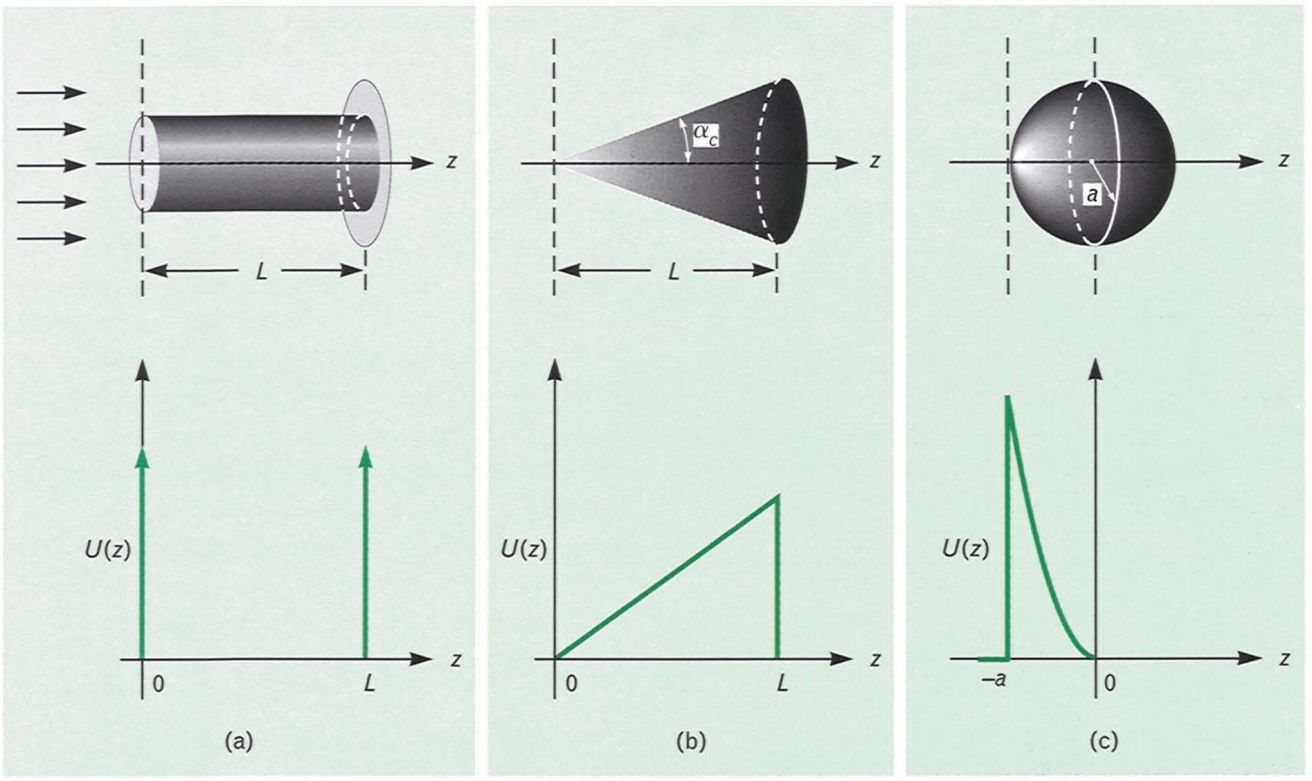

FIGURE 11. Range-resolved laser radar cross sections for on-axis viewing: (a) top hat; (b) cone; (c) Lambertian sphere.

because the functional form of $h_{||}$ also depends on the aspect angle. Therefore, to apply these results we would have to provide the appropriate height function of an object for each aspect angle. We avoid this problem by performing the integration in a rotated coordinate system (ξ, η, ζ) that is natural (or preferred) for defining the object shape. We denote the height function in this new coordinate system by $h(\xi, \eta)$. If there is an axis of symmetry, it is usually aligned with the ζ axis.

In the rotated coordinate system the height function remains constant and the illumination direction varies. Let α and β be the polar and azimuthal angles representing the direction of illumination, as illustrated in Figure 12. Then the expression analogous to Equation 7 for calculating the angle of incidence θ in terms of the new height function is

$$\cos\theta = \frac{\cos\alpha - \sin\alpha\,(h_\xi \cos\beta + h_\eta \sin\beta)}{\sqrt{h_\xi^2 + h_\eta^2 + 1}}. \qquad (16)$$

Note that Equation 16 reduces to Equation 7 when $\alpha = 0$.

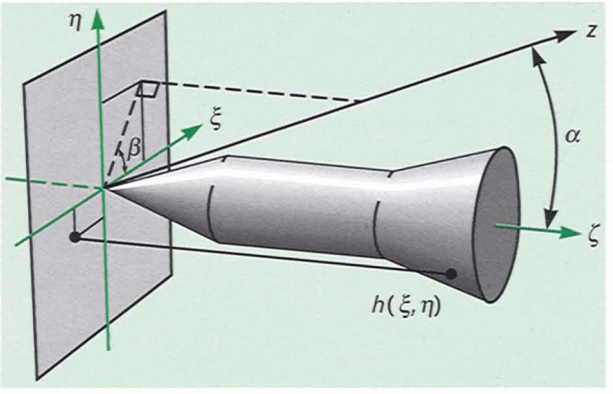

FIGURE 12. Coordinate system for describing the object height function $h(\xi, \eta)$ and the direction of illumination (α, β).

We evaluate σ in the rotated coordinate system by changing the variables of integration from x and y to ξ and η. Equation 9 then becomes

$$\sigma = 4\pi \iint_{A_h} f(\theta)\cos^2\theta \sqrt{h_\xi^2 + h_\eta^2 + 1}\; d\xi\, d\eta. \qquad (17)$$

The region of integration A_h corresponds to the pro-

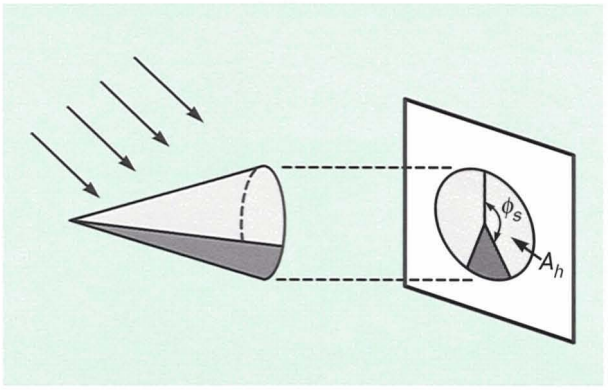

FIGURE 13. Region of integration for calculating the laser radar cross section for off-axis illumination of a cone. As the aspect angle increases, the angular range of integration $\pm\phi_s$ in the projection plane decreases. This range of integration corresponds to the illuminated surface area of the cone.

jection of the illuminated surface area onto the ξ-η plane, as illustrated in Figure 13. Observe that Equation 17 simplifies to Equation 9 when $\alpha = 0$. There is one complication in using Equation 17 that does not arise in Equation 9. In Equation 9 we account for shadowing by retaining only the lowest value of $h_{||}$ if it is multivalued. In Equation 17 we must separately determine when the old height function $h_{||}$ for the given aspect angle is multivalued.

A similar integral exists for the range-resolved laser radar cross section. In the rotated coordinate system, Equation 10 takes the form

$$U(z) = 4\pi \iint_{A_h} f(\theta)\cos^2\theta \sqrt{h_\xi^2 + h_\eta^2 + 1} \times \delta\left[z - h(\xi,\eta)\cos\alpha - \sin\alpha(\xi\cos\beta + \eta\sin\beta)\right] d\xi\, d\eta. \quad (18)$$

Again, the advantage of this form is that the height function h is independent of aspect angle. As expected, Equation 18 reduces to Equation 10 when $\alpha = 0$. Note that Equation 18 is identical to Equation 17, except for the inclusion of the δ-function, which limits the integration to the contour formed by the intersection of the object boundary with the range plane. Note also that we can obtain the formula that describes the integration path by setting the argument of the δ-function to zero.

Equations 17 and 18 can be difficult to evaluate analytically. Closed-form solutions can be found for many simple shapes, however, and these solutions aid in the prediction and interpretation of target signatures. Because complex objects can usually be described as a combination of simple component shapes, we should carry the analysis of simple components as far as possible. As long as we account for cross shadowing of one component by another, the results we determine for individual components can be used in modeling more complex object shapes.

Many component shapes have some form of symmetry. In the remainder of this section we consider off-axis illumination of the class of objects that are symmetric around an axis of rotation. We can characterize these objects by a height function $h(r)$ that depends only on the radius r. Some important members of this class, including spheres, disks, cylinders, and cones, are treated below.

Let us first consider the laser radar cross section σ. Because the sphere is radially symmetric, σ is independent of aspect angle as long as the material covering the sphere is applied uniformly. Most other objects, however, exhibit a strong angular dependence in their cross section. For example, by Equation 17, the cross section of a disk or any other flat object falls off as $\cos^2\theta$, not including any variations caused by $f(\theta)$. The Lambertian cylinder also has a simple dependence on aspect angle. Let the radius of the cylinder be denoted by a and the length by L. If the aspect angle α is measured relative to the cylinder axis, then the cross section σ is given by $2\pi aL\sin^2\alpha$, not including contributions from end caps. The aspect-angle dependence of σ for a Lambertian cone is not so simple, but a closed-form solution does exist [14, 32]. Figure 14 illustrates this angle dependence for a Lambertian cone with a Lambertian disk base.

Next, we consider the range-resolved laser radar cross section $U(z)$. In general, $U(z)$ is more difficult to calculate than σ, but the solutions for $U(z)$ tend to be more interesting because of the dependence on range. A specialized form of Equation 18 results when the object is axially symmetric. The steps involved in determining this form are (1) transforming the integral to polar coordinates r and ϕ, (2) converting the δ-function to an explicit function of r, and (3) performing the radial integration via the δ-function. The

result does not depend on β. We set $\beta = 180°$ to center the range of integration around $\phi = 0$, which yields

$$U(z) = 8\pi \int_{\phi} \sum_{i} f(\theta) \cos^2\theta \, \frac{r_i \sqrt{1 + h_r^2}}{\left| h_r \cos\alpha - \sin\alpha \cos\phi \right|} \, d\phi . \tag{19}$$

Equation 19 requires some clarification. First we explain the meaning of the summation. For given values of azimuth angle ϕ, range z, and aspect angle α, more than one value of the radius r can lie on the integration path. These values of r correspond to the discrete solutions r_i of the integration-path equation

$$z = -r_i \sin\alpha \cos\phi + \cos\alpha \; h(r_i) . \tag{20}$$

Each solution contributes to $U(z)$; hence the summation in Equation 19. The symbol h_r in Equation 19 denotes the derivative of $h(r)$ with respect to r, evaluated at the point $r = r_i$.

The integration in Equation 19 extends over values of the azimuth angle ϕ ranging between 0 to π such that all of the following conditions are satisfied: (1) a solution to Equation 20 exists, which implies that the range plane intersects the object; (2) $\cos\theta > 0$, which implies that the surface element faces the source; and (3) only the lowest-valued branch of the corresponding function $h_{||}$ is taken when it is multivalued, which implies that the point is not shadowed by a point closer to the source. Integration over azimuth angles between $-\pi$ and 0 has been accounted for in Equation 19 by using symmetry and doubling the result.

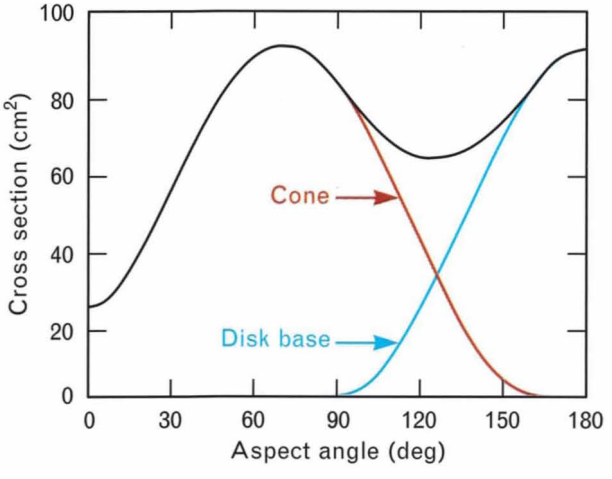

FIGURE 14. Aspect-angle dependence of the laser radar cross section of a Lambertian cone 10 cm in length with a cone half-angle of 15°. The colored lines indicate the separate contributions from the cone and the disk base.

The formula for the angle of incidence θ given in Equation 16 reduces to

$$\cos\theta = \frac{h_r \sin\alpha \cos\phi + \cos\alpha}{\sqrt{1 + h_r^2}} \tag{21}$$

for axial symmetry. Equations 19 through 21 provide the basic framework for calculating the angular dependence of the range-resolved laser radar cross section for axially symmetric objects. In the following sections we use these results to write solutions for the aspect-angle dependence of $U(z)$ for disks, cones, cylinders, and truncated spheres.

Disk. Let a disk of radius a be positioned with its center at the origin. It is relatively simple to apply Equation 19 to this situation because the height function has a constant value; namely, $h(r) = 0$. Consequently, there are no shadow boundaries to contend with, and the integration path is a straight line. The azimuthal range of integration is determined by setting $r_i = a$ in Equation 20 and solving for ϕ. The resulting form for $U(z)$ is elliptical in shape:

$$U(z) = 8\pi f(\alpha) \cot^2\alpha \sqrt{a^2 \sin^2\alpha - z^2} \quad \text{for} \quad |z| \le |a \sin\alpha| . \tag{22}$$

This result is intuitive because the range-resolved laser radar cross section of a disk is proportional to the length of the straight-line integration path, which varies elliptically. Equation 22 is illustrated in Figure 15. As the aspect angle α approaches normal incidence, the peak value of $U(z)$ increases without bound, and the width of the ellipse approaches zero. In this limit $U(z)$ reduces to a δ-function, as in Equation 11.

Cone. For generality, we allow the cone to be truncated and we denote the radii at the two ends by a_1 and a_2. If we assume the tip of the corresponding non-truncated cone is at the origin, then the cone is represented by the height function $h(r) = r \cot\alpha_c$ for $a_1 < r < a_2$. With these definitions, Equation 19 for the range-resolved laser radar cross section becomes

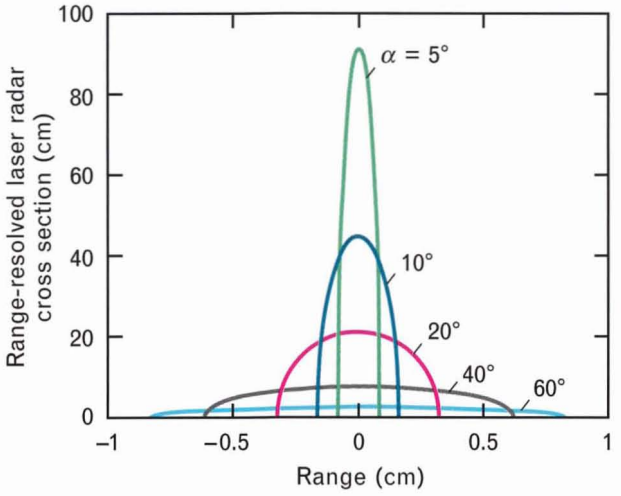

FIGURE 15. Range-resolved laser radar cross section of a 1-cm-radius Lambertian disk at various illumination angles.

$$U(z) = 8\pi \sin \alpha_c \times |z| \int_{\phi_1}^{\phi_2} \left(\frac{\tan \alpha_c + \tan \alpha \cos \phi}{1 - \tan \alpha_c \tan \alpha \cos \phi} \right)^2 f(\theta)\, d\phi\,, \quad (23)$$

and the local angle of incidence in Equation 21 reduces to

$$\cos \theta = \cos \alpha_c \sin \alpha \cos \phi + \sin \alpha_c \cos \alpha\,. \quad (24)$$

Although Equation 23 can be integrated analytically for certain choices of $f(\theta)$, we leave it in its integral form because it is compact, well suited to numerical integration, and valid for arbitrary choices of $f(\theta)$.

Before Equation 23 can be applied, we must determine the limits of integration. This determination is often the most difficult part of the calculation of a range-resolved laser radar cross section. It is complicated because these limits generally vary with both the aspect angle α and the range value z. But once these limits are determined, they can be applied to arbitrary choices of $f(\theta)$. As illustrated in Figure 16, two boundary types are associated with the azimuthal limits of integration for a cone. They are *shadow boundaries* and *truncation boundaries*. Shadow boundaries cause the region of integration A_p in Equation 18 to be pie shaped, as illustrated in Figure 16(b). We denote the half-angle of the illuminated segment of the pie by ϕ_s. Truncation boundaries occur when the range plane cuts through the circle of radius a_1, which is associated with the truncation plane, or through the circle of radius a_2, which defines the cone base. The corresponding azimuthal limits of integration are denoted as ϕ_{b_1} and ϕ_{b_2}, respectively. Note that ϕ_s is independent of range but that ϕ_{b_1} and ϕ_{b_2} depend on range.

Before evaluating the shadow and truncation boundaries, we point out an important feature of Equation 23—the explicit dependence on z occurs only in the linear factor in front of the integral.

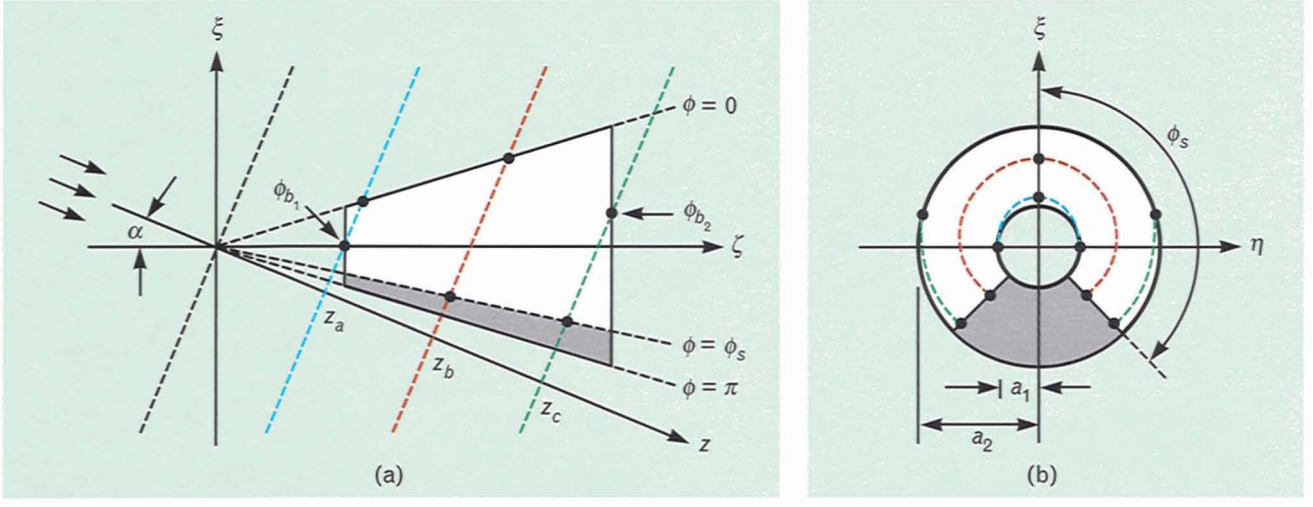

FIGURE 16. Limits of integration for calculating the range-resolved laser radar cross section for off-axis illumination of a truncated cone: (a) shadow boundaries and truncation boundaries for three separate range planes cutting through the cone; (b) the corresponding integration paths in ξ-η space.

Therefore, as long as the limits of integration do not depend on z, the $U(z)$ curve will increase linearly with range, just as it does for the on-axis cone described by Equation 14. As already noted, the limits of integration can exhibit range dependence only for those values of range and for those aspect angles where the range plane intersects one of the truncation planes. For every truncated cone there is a range of aspect angles, beginning with $\alpha = 0$, such that there are no truncation boundaries. Thus every truncated cone exhibits a linear dependence on z over some region of α-z space, and the longer the cone, the larger the angular region where this dependence occurs. This linear dependence on z produces a distinctive signature that can be used for identifying and characterizing conical objects.

Now we describe how the two types of boundaries are determined. Shadow boundaries can be obtained by setting $\cos\theta$ equal to zero in Equation 24 and solving for ϕ:

$$\phi_s = \mathrm{Re}\left[\cos^{-1}(-\tan\alpha_c \cot\alpha)\right]. \qquad (25)$$

The reason for taking the real part is that the inverse cosine becomes complex when $\alpha < \alpha_c$ and when $\alpha > \pi - \alpha_c$. In the first case, the entire cone is illuminated so that no shadowing occurs, and Equation 25 reduces to $\phi_s = \pi$. In the second case, the cone is completely unilluminated (only the inside of the cone is visible to the laser), so that complete shadowing occurs and Equation 25 reduces to $\phi_s = 0$.

Truncation boundaries are determined by setting r_i equal to a_1 or a_2 in Equation 20 and solving for ϕ. This yields

$$\phi_{b_n} = \mathrm{Re}\left[\cos^{-1}\left(\cot\alpha_c \cot\alpha - \frac{z}{a_n \sin\alpha}\right)\right], \qquad (26)$$

where n assumes the value 1 or 2. Taking the real part in Equation 26 allows us to define ϕ_{b_n} for those cases in which no intersection occurs between the range plane and the truncation boundary of the cone. The value assigned is the last value, 0 or π, that ϕ_{b_n} had as the range plane moved away from the object.

Now that we have analyzed the different boundary types that can occur, the next step is to choose the limits of integration that are appropriate for the given situation. By referring to Figure 16, we can see that the algorithm defined by

$$\phi_1 = \min(\phi_s, \phi_{b_1}, \phi_{b_2}) \qquad (27)$$

and

$$\phi_2 = \min\left[\phi_s, \max(\phi_{b_1}, \phi_{b_2})\right] \qquad (28)$$

correctly handles all possible situations. In Figure 17 we plot Equation 23 for the range-resolved laser radar cross section of a truncated Lambertian cone illuminated at various angles. The cone has the same shape as the one in Figure 16. The cone half-angle is 15°, the distance between truncation planes is 10 cm, and the distance from the first truncation plane to the apex of the corresponding untruncated cone is 5 cm. Note that as pointed out above, the $U(z)$ curves have a large linear region if the aspect angle is small, but that this linear region eventually disappears as the aspect angle increases.

Cylinder. The cylinder does not lend itself to direct analysis by Equation 19 because $h(r)$ is ill defined in the associated coordinate system. We can apply Equa-

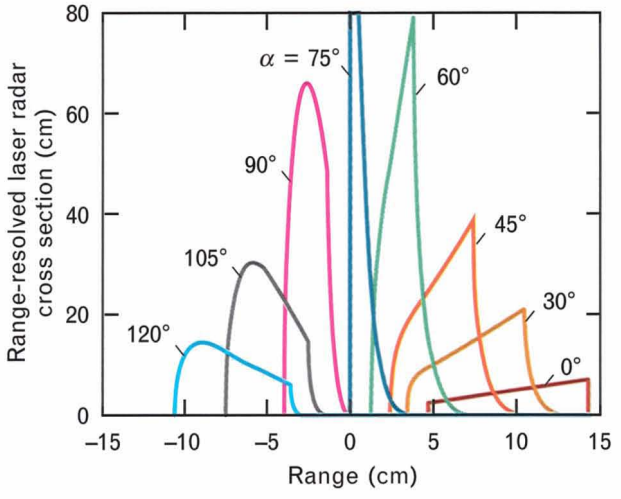

FIGURE 17. Range-resolved laser radar cross section for a truncated Lambertian cone viewed at various aspect angles. The cone half-angle is 15° and the distance between the truncation planes is 10 cm. The range-reference point is located at the apex of the corresponding untruncated cone, which is located 5 cm to the left of the first truncation plane. There are no contributions from the disk-shaped regions formed by the intersection of the truncation planes with the cone.

tion 23 to a cylinder, however, by taking the limit as α_c approaches zero. A slight complication occurs when we do this. Because the origin of the coordinate system is at the apex of the cone, the range values of interest shift to infinity. To adjust for this shift, we transform the equation to a coordinate system having its origin at the truncation point where $r = a_1$. When the aspect angle $\alpha = 0$, the range offset between the origins of the two coordinate systems is simply the axial distance from the apex of the cone to the truncation plane $\zeta_0 = a_1 \cot \alpha_c$. But as α increases, this offset is reduced by a factor of $\cos \alpha$. Thus we transform coordinates in Equation 23 by replacing z with $z + a_1 \cot \alpha_c \cos \alpha$. For a cylinder of length L and radius a, Equation 23 reduces to

$$U(z) = 8\pi a \frac{\sin^2 \alpha}{|\cos \alpha|} \times \int_{\phi_1}^{\phi_2} \cos^2 \phi \, f\left[\cos^{-1}(\sin \alpha \cos \phi)\right] d\phi , \quad (29)$$

where

$$\phi_{b_1} = \mathrm{Re}\left[\cos^{-1}\left(\frac{-z}{a \sin \alpha}\right)\right]$$

and

$$\phi_{b_2} = \mathrm{Re}\left[\cos^{-1}\left(\frac{L \cos \alpha - z}{a \sin \alpha}\right)\right].$$

The limits of integration are obtained by using Equations 27 and 28 with $\phi_s = \pi/2$. Note that $U(z)$ for a cylinder is independent of range, regardless of the functional form of $f(\theta)$, as long as the range plane does not cross a truncation boundary. Thus all cylinders have a region in z-α space where $U(z)$ is independent of range, and this region provides a distinctive range-resolved laser radar cross-section signature for cylindrical objects. In Figure 18 we plot Equation 29 for a 10-cm-long 4-cm-diameter Lambertian cylinder illuminated at various angles α. To separate the curves for the different values of α from one another in range, we have actually plotted $U(z - \zeta_0 \cos \alpha)$, where $\zeta_0 = 5$ cm. The range offset in the argument corresponds to measuring range with respect to a point on the cylinder axis that is 5 cm outside of the cylinder.

Truncated Sphere. Equation 15 gives the general solution of the range-resolved laser radar cross section for a complete sphere. Although this solution does not depend on aspect angle, the solution for a truncated sphere does. Because the truncated sphere is an important component for building up composite target models, we also describe its angle-dependent range-resolved laser radar cross section. We assume the center of the sphere is located at the origin and that the truncation plane is at a height h. Thus the value of h ranges between $-a$ and a, with $-a$, 0, and a corresponding respectively to a single point at the pole, a hemisphere, and a complete sphere. For some values of z the truncation boundary limits the range of the azimuthal integration so that it no longer covers a complete circle. Equation 15 is modified to account for the truncation boundary by replacing π with the actual angular half-range of integration, which varies between 0 and π. The new form is

$$U(z) = \frac{8\pi}{a} f\left[\cos^{-1}(-z/a)\right] \times \mathrm{Re}\left[\cos^{-1}\left(\frac{z \cos \alpha - h}{\sqrt{a^2 - z^2} \sin \alpha}\right)\right] z^2 \quad (30)$$
$$\text{for } -a \le z \le 0 .$$

Spherical objects also have a distinctive signature. For any values of the truncation height h, there is an angular region, beginning with $\alpha = 0$, such that $U(z)$ is independent of viewing angle over certain values of z. Equation 30 is illustrated in Figure 19.

Composite Objects. We combine the preceding results to obtain the aspect-angle-dependent range-resolved laser radar cross section for a Lambertian cylinder-disk combination and for a Lambertian sphere-cone-disk combination. The spherical and conical segments of the sphere-cone-disk are joined together such that the slope of the surface is continuous. Figure 20 shows three-dimensional plots of the logarithm of the range-resolved laser radar cross section as a function of range and aspect angle for these

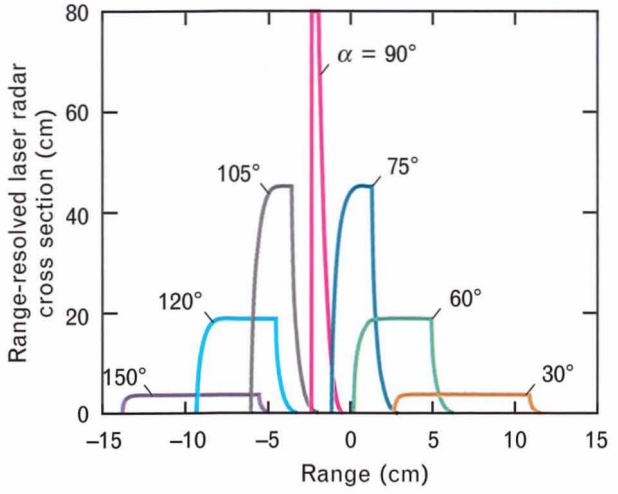

FIGURE 18. Range-resolved laser radar cross section for a Lambertian cylinder viewed at various aspect angles. The length of the cylinder is 10 cm and its diameter is 4 cm. The range-reference point is located 5 cm outside of the cylinder to separate the various plots in range. There are no contributions from the disk-shaped endcaps.

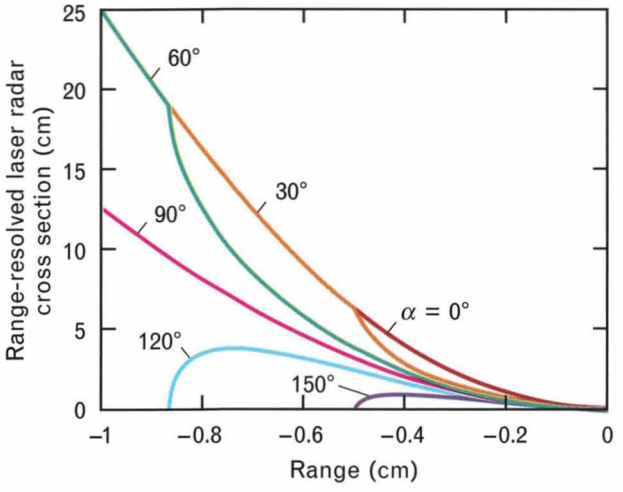

FIGURE 19. Range-resolved laser radar cross section for a 1-cm-radius Lambertian hemisphere viewed at various aspect angles.

two objects. The separate signatures for the disk, the cone, the cylinder, and the sphere are evident in these plots. We have already pointed out that it is easier to obtain the autocorrelation of $U(z)$ than $U(z)$ by the wavelength-decorrelation method. Figure 20 also shows the autocorrelation functions of $U(z)$ for comparison. We can clearly distinguish between the two shapes, given the aspect-angle dependence of the autocorrelation function.

Theory for Wavelength Decorrelation

We have shown how the range-resolved laser radar cross section $U(z)$ relates to an object's shape and angular surface-scattering properties. Our next step is to show theoretically how $U(z)$ is related to the fluctuating speckle intensity caused by scanning the laser frequency in the wavelength-decorrelation technique. In the box entitled "Wavelength Decorrelation of Speckle" we explain (1) why the speckle intensity fluctuates when the laser frequency is scanned, (2) how much of a frequency shift is necessary to decorrelate the speckle pattern, (3) the minimum required sampling rate, and (4) how the range resolution is affected by the scan length. We begin this section by calculating the spectral density of the speckle intensity and then progress toward bispectral analysis in an effort to maximize the information extracted from the signal.

Spectral Density

We have stated that a fundamental relation exists between the spectral density of the speckle signal and the autocorrelation function of the range-resolved laser radar cross section of the illuminated object. We now derive this relation from basic principles. As in the previous section, we quantify the speckle intensity by using the irradiance. The analysis is divided into two parts. First we establish a model for calculating the irradiance $E(t)$ at the receiver in terms of the physical properties of the object; then we use this model to perform the statistical calculation of the spectral density.

The spectral density of $E(t)$ is defined in terms of its Fourier transform $\tilde{E}(f)$ by

$$G_E(f) = \frac{\left\langle \left| \tilde{E}(f) \right|^2 \right\rangle}{T}, \tag{31}$$

where

$$T = \int_{-\infty}^{\infty} |w(t)|^2 \, dt \tag{32}$$

is the effective scan duration, and $w(t)$ is a dimen-

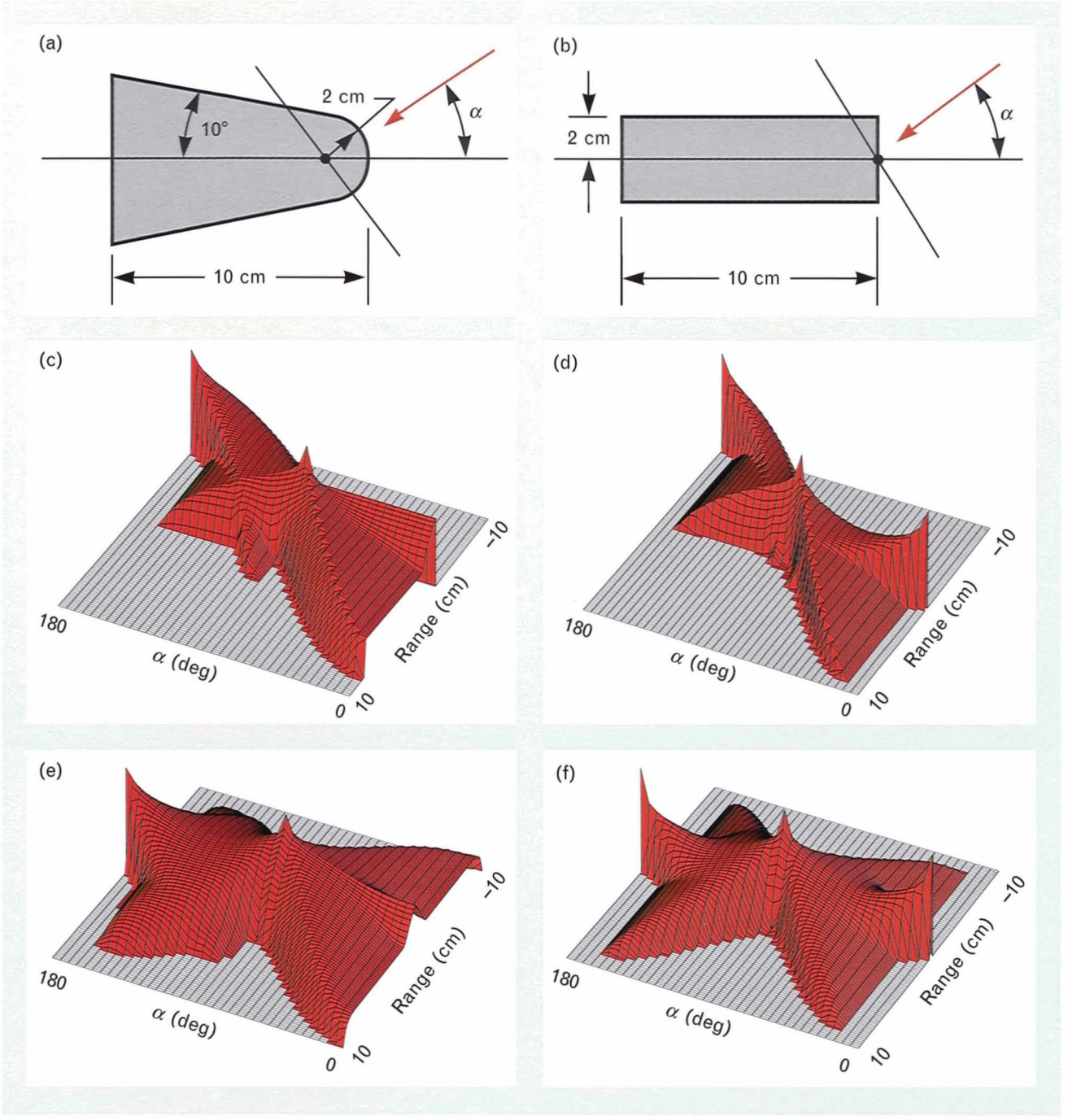

FIGURE 20. Wavelength-decorrelation signatures for composite objects: (a) Lambertian sphere-cone-disk combination; (b) Lambertian cylinder with disk endcaps; (c) and (d) aspect-angle dependence of the range-resolved laser radar cross section for parts *a* and *b*, respectively; (e) and (f) autocorrelation functions of the range-resolved laser radar cross section for parts *a* and *b*, respectively. The magnitude of these signatures is plotted on a logarithmic scale covering four decades for parts *c* and *d* and two decades for parts *e* and *f*.

sionless window function, ranging between zero and unity, that specifies the temporal shape and the duration of the transmitted signal irradiance. If $w(t)$ turns on and off abruptly, then T is simply the scan duration in the usual sense. Typically, $w(t)$ tapers to zero at the edges of the signal for the purpose of decreasing

the sidelobes. In this analysis, the scan duration is assumed to be long compared to the time it takes light to traverse the range extent of the object.

Our model for the irradiance at the receiver differs from previous models for analyzing the wavelength dependence of speckle in that we do not try to predict angular-scattering effects from assumed surface statistics. Instead, these surface-correlation effects are taken into account directly through the functional dependence of $f(\theta)$, which can be readily measured in practice. This approach greatly simplifies the calculations. The resulting analysis, which is a hybrid between radiometry and physical optics, proceeds as follows.

First we break the surface of the object into N small uncorrelated area elements A_j and use principles of radiometry to calculate the contribution to the speckle-averaged irradiance at the receiver from each individual element. The magnitude of the complex amplitude at the receiver arising from an individual surface element on the object is obtained by taking the square root of the irradiance from that element. The phase is introduced by considering path lengths and assigning each scattering cell a random phase offset ϕ_j that is uniformly distributed over 2π radians. The N contributions $V_j(t)$ to the total complex amplitude $V(t)$ at the receiver are then added coherently as in physical optics. Finally, the irradiance $E(t)$ is obtained by squaring the magnitude of the complex amplitude.

This model for $E(t)$ is based on the following reasoning. The area A_j of each surface element is large enough to determine the angular scattering (i.e., large compared to the wavelength and the surface correlation length), but small enough so that the resultant complex amplitude $V(t)$ at the receiver would not change significantly if the elements were further subdivided. For example, the range extent L_j of the individual surface elements must be small enough so that the corresponding decorrelation frequency $\Delta\nu_D = c/(2L_j)$ from Equation B in the box on the wavelength decorrelation of speckle is large compared with the total frequency scan of the laser. Because objects of interest are large on a wavelength scale, we can divide the surface area into many individual cells that each satisfy these requirements.

The first step in calculating $E(t)$ is to define the transmitted signal; its complex amplitude is expressed in the form

$$V_T(t) = \sqrt{E_0\, w(t)}\, \exp\left[i\phi_T(t)\right].$$

In this equation E_0 represents the final target irradiance after the transmitted beam has propagated over the distance R. As explained above, variations in the transmitted irradiance with time are accounted for through the window function $w(t)$. The phase $\phi_T(t)$ is obtained by assuming that the initial laser frequency is ν_0 and that ν increases linearly in time at the rate γ, such that $\nu = \nu_0 + \gamma t$. Through application of the relation $d\phi/dt = 2\pi\nu$ we obtain

$$\phi_T(t) = 2\pi\left(\nu_0 + \frac{\gamma t}{2}\right)t\,, \tag{33}$$

which completes the description of the transmitted signal.

Having defined the transmitted signal, we are now in a position to write the irradiance at the receiver. Because a monostatic and far-field configuration is assumed, we need only consider rays that propagate parallel to the z-axis. For the jth scattering cell, the round-trip propagation time from the transmitter and back to the receiver is $t_0 + t_j$, where $t_0 = 2R/c$ is the round-trip propagation time to the $z = 0$ plane (from which the object height function is defined) and $t_j = 2h_j/c$ is the round-trip propagation time between the $z = 0$ plane and the jth scattering cell. The time dependence associated with the contribution $V_j(t)$ is the same as the time dependence of the transmitted signal $V_T(t)$, but at the earlier time $t - t_0 - t_j$. By the procedure outlined above, the total complex amplitude at the receiver is

$$V(t) = \sqrt{w(t - t_0)} \times \sum_{j=1}^{N} \sqrt{\left\langle E_j \right\rangle}\, \exp\left\{i\left[\phi_T(t - t_0 - t_j) + \phi_j\right]\right\}. \tag{34}$$

In Equation 34 we assume that the pulse duration T is long compared to the largest value of t_j and that $w(t)$ is slowly varying, except possibly at the edges, to replace $w(t - t_0 - t_j)$ by $w(t - t_0)$ and move it outside of the summation. The expected irradiance $\left\langle E_j \right\rangle$ from

WAVELENGTH DECORRELATION OF SPECKLE

ONE OF THE BASIC characteristics that can be used to describe the wavelength dependence of speckle is the sensitivity of the speckle pattern to changes in laser frequency. If a large frequency shift is required for changing, or *decorrelating*, the speckle pattern, then we say that the speckle pattern has a large decorrelation frequency $\Delta\nu_D$.

We can show that $\Delta\nu_D$ is inversely proportional to the range extent L of the illuminated object. Let the cone in Figure A be illuminated on axis with a tunable laser. To calculate the resultant complex amplitude at a distant receiver located on axis, we sum the backscattered contributions corresponding to the different scattering cells located on the surface of the cone. A phase delay ϕ is associated with the propagation path, or optical path length, for each scattering cell. If we measure ϕ with respect to the $z = 0$ plane, then the phase delay for propagation from this plane to a scattering cell with range z is $\phi = -2\pi z/\lambda = -2\pi z\nu/c$, where λ is the wavelength, ν is the optical frequency, and c is the speed of light. The minus sign is consistent with a forward propagating wave and the positive harmonic time dependence $\exp(i2\pi\nu t)$. For the moment, let us consider only scattering contributions from the two extreme ends of the cone, i.e., from planes with range values of $z = 0$ and $z = L$. The phase delay associated with the round-trip propagation path $2L$ between these two planes is

$$\phi = -4\pi L\nu/c. \qquad \text{(A)}$$

Either constructive or destructive interference occurs between these two contributions, depending on the value of ϕ for the particular frequency ν. This variation between destructive and constructive interference from different range planes is what causes the intensity of the speckle pattern to fluctuate as we scan the laser frequency. The larger the range extent, the more rapid is the variation with laser frequency.

In Figure A we use the red and blue sinusoids to illustrate how the phase delay varies with laser frequency (we have exaggerated the wavelength scale for the purpose of visualization). For the red wave, there are 5 complete wavelength cycles within the range extent of the cone. As the laser frequency increases, the wavelength decreases, until eventually there are 5.5 wavelength cycles within the range extent, as illustrated by the blue curve. Thus the red and blue sinusoids are out of phase by 180° at the $z = L$ plane. An additional half-cycle of phase delay is introduced on the return trip so that the two waves are back in phase at the $z = 0$ plane. If no other scattering contributions existed, then the speckle intensity would have gone through a complete cycle for the frequency offset between the red and blue waves. Because there are scattering cells located at other range planes, the speckle intensity does not return to its original value. Even though the contributions from the end segments are back in phase, the contributions from the middle of the cone are now 180° out of phase. Thus the new speckle pattern for the cone (corresponding to the blue wave) is different in appearance from the initial pattern (corresponding to the red wave).

To find an expression for the decorrelation frequency $\Delta\nu_D$, we use Equation A to calculate the phase delay ϕ corresponding to the propagation distance $2L$ at two separate frequencies ν and $\nu + \Delta\nu$, and then we subtract to find the phase-delay difference $\Delta\phi$ resulting from the frequency offset $\Delta\nu$:

$$\Delta\phi = -2\pi\,\frac{2L}{c}\,\Delta\nu.$$

We then choose a value for the phase-delay difference $\Delta\phi$ that is sufficiently large to cause the two speckle patterns to differ appreciably. We have already shown that $\Delta\phi = 2\pi$ is sufficiently large. The resulting expression for the decorrelation frequency is

$$\Delta\nu_D = \frac{c}{2L}. \qquad \text{(B)}$$

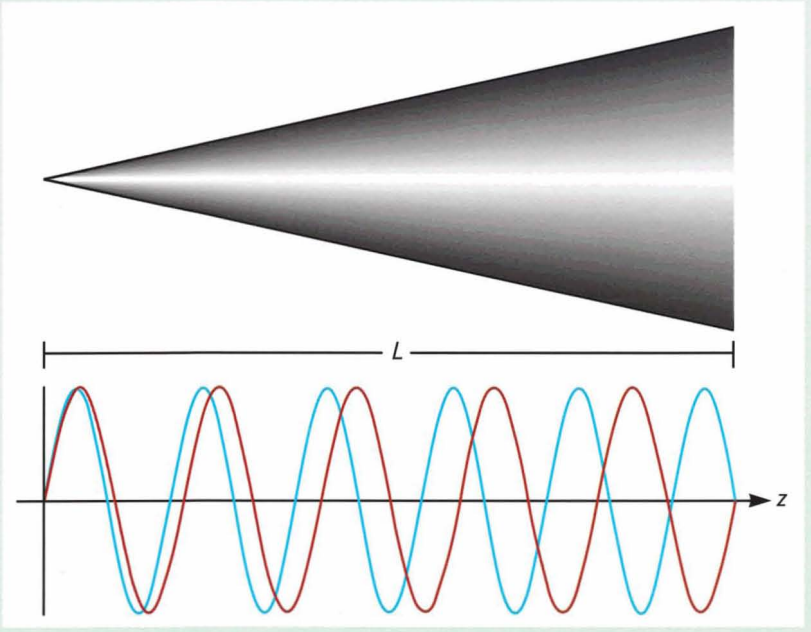

FIGURE A. Effect of changing the laser frequency on the phase delay.

As an illustration of Equation B, the decorrelation frequency for an object with a range extent of 10 cm is 1.5 GHz. This result agrees well with the speckle-intensity measurements in Figure 30 for a 10-cm-long cone and a 10-cm-long triconic.

The next observation that we make about the wavelength dependence of speckle is that the fluctuating speckle intensity is bandlimited. In other words, the Fourier transform of the intensity sequence has a cutoff frequency, above which it is zero-valued. Correspondingly, the intensity sequence produced by scanning the laser has a highest frequency of oscillation, and the speckle intensity cannot change any faster than this highest-frequency component. We know that large oscillation frequencies correspond to large range offsets between scattering cells. Therefore, the cutoff frequency (which bandlimits the speckle-intensity sequence) is determined by the range extent L of the object.

The decorrelation frequency $\Delta\nu_D$ in Equation B was defined to correspond to the period associated with the highest-frequency oscillation in the intensity-versus-laser-frequency curve. By the Nyquist sampling theorem, we must sample the speckle-intensity sequence at least twice during each of these highest-frequency oscillations. This fact leads us to the important conclusion that the laser-frequency step size between samples in the wavelength-decorrelation technique must obey the expression

$$\Delta\nu_{\text{step}} \leq \frac{c}{4L}. \qquad \text{(C)}$$

For example, an object with a range extent of 10 cm would require a laser-frequency step size of 750 MHz or less.

We next consider how the total scan bandwidth B affects the range resolution of the measurement. Recall that a scan length equal to the decorrelation frequency $\Delta\nu_D$ induces one complete cycle of phase delay between contributions from the two ends of the scattering object. Each time we increase the length of the frequency scan by one frequency-decorrelation unit $\Delta\nu_D$, we induce an additional cycle of phase delay within the range extent. Consequently, if we scan the laser frequency by N times the decorrelation frequency $\Delta\nu_D$, we divide the range extent into N segments. The length of these individual segments corresponds to the range resolution Δz of the measurement.

We can obtain an expression for Δz in terms of the scan bandwidth B by manipulating Equation B. If we multiply both sides of Equation B by N, then the left side is equal to the total scan bandwidth B. The right side contains the expression L/N, which is equal to the range resolution Δz. By solving for the range resolution, we obtain

$$\Delta z = \frac{c}{2B}, \qquad \text{(D)}$$

which is identical to the result given in Equation 45. As an example of Equation D, we must scan the laser over a bandwidth of 150 GHz to obtain a range resolution of 1 mm.

the jth scattering cell is found by substituting its cross section, obtained from Equation 8, into Equation 5 and rearranging terms to yield

$$\langle E_j \rangle = \frac{E_0}{R^2} f(\theta_j) \cos^2\theta_j A_j .$$

The irradiance $E(t)$ at the receiver is the magnitude-squared of $V(t)$ in Equation 34.

To perform the statistical analysis, we must expand the magnitude-squared in the computation of $E(t)$ into a double summation. This is done by using two different summation indices, say j for writing $V(t)$ and k for writing its complex conjugate, and then multiplying to yield

$$E(t) = w(t - t_0) \sum_{j=1}^{N} \sum_{k=1}^{N} \sqrt{\langle E_j \rangle \langle E_k \rangle} \times \exp\left\{ i \left[\phi_T(t - t_0 - t_j) - \phi_T(t - t_0 - t_k) + \phi_j - \phi_k \right] \right\}. \quad (35)$$

The significance of a linear scan becomes apparent when Equation 33 for $\phi_T(t)$ is substituted into Equation 35; the quadratic terms cancel, which leaves a linear dependence of phase on time t:

$$\phi_T(t - t_0 - t_j) - \phi_T(t - t_0 - t_k) = 2\pi(t_k - t_j)\left[\nu_0 + \gamma(t - t_0)\right] + \pi\gamma({t_j}^2 - {t_k}^2). \quad (36)$$

These linear phase factors correspond to frequency offsets in the Fourier-transform domain. The size of these offsets is proportional to the axial propagation time $t_k - t_j$, and hence also proportional to the range offset $h_k - h_j$ between scattering cells. Thus the intensity signal carries information about range. We shall see that the other phase terms in Equation 36, which do not depend on time, are unimportant and cancel out later in the analysis.

Applying Equation 31, we proceed with the evaluation of the spectral density by taking the Fourier transform of Equation 35, squaring its magnitude, applying the expected-value operator, and dividing by the effective scan duration. This yields

$$G_E(f) = \frac{1}{T} \sum_{j=1}^{N} \sum_{k=1}^{N} \sum_{l=1}^{N} \sum_{m=1}^{N} \sqrt{\langle E_j \rangle \langle E_k \rangle \langle E_l \rangle \langle E_m \rangle} \times \left\langle \exp\left[i(\phi_j - \phi_k - \phi_l + \phi_m) \right] \right\rangle \times \exp\left[-i2\pi\nu_0(t_j - t_k - t_l + t_m) \right] \times \exp\left[-i\pi\gamma({t_j}^2 - {t_k}^2 - {t_l}^2 + {t_m}^2) \right] \times \tilde{w}(f + f_j - f_k)\, \tilde{w}^*(f + f_l - f_m), \quad (37)$$

where the notation $f_j = \gamma t_j$ has been used for compactness. Note that frequency offsets are related to range offsets through $f_j = 2\gamma h_j / c$. Again, the magnitude-squared has been expanded in Equation 37 by doubling the number of summations, this time to four. The reason for expanding the summation is to write the spectral density as a linear combination of the function $\exp[i(\phi_j - \phi_k - \phi_l + \phi_m)]$ so that the expected-value brackets can be moved inside the summation to act on this function alone.

Next we apply known statistical properties of the random process ϕ_j to evaluate the new expected value, in the hope of simplifying Equation 37. We have made two assumptions about ϕ_j: (1) it is uncorrelated from cell to cell, and (2) it is uniformly distributed over 2π radians. These assumptions completely specify ϕ_j and make it possible to write the expected value in terms of Kronecker delta functions as

$$\left\langle \exp\left[i(\phi_j - \phi_k - \phi_l + \phi_m) \right] \right\rangle = \delta_{jk}\delta_{lm} + \delta_{jl}\delta_{km} - \delta_{jklm} . \quad (38)$$

By definition, a Kronecker delta function is unity when its subscripts are equal, and zero otherwise. We now show how Equation 38 can be derived by applying the two assumptions listed above. By the first assumption, the characteristic function can be expressed as the product of the expected values of the individual factors, as long as the indices are all unequal. But by the second assumption

$$\left\langle \exp(i\phi_j) \right\rangle = 0 , \quad (39)$$

and the product of the expected values is zero. The only way for the expected value in Equation 38 to be

nonzero is if the phases add to zero, in which case the expected value is unity. For the phases to add to zero for every realization of the random process, the indices for positive and negative phases must be equal in pairs. Equation 38 covers all the possibilities.

Applying Equation 38 to Equation 37 allows the quadruple summation to be reduced to

$$G_E(f) = \frac{|\tilde{w}(f)|^2}{T}\left[\left(\sum_{j=1}^{N}\langle E_j\rangle\right)^2 - \sum_{j=1}^{N}\langle E_j\rangle^2\right] + \sum_{j=1}^{N}\sum_{k=1}^{N}\langle E_j\rangle\langle E_k\rangle\frac{|\tilde{w}(f+f_j-f_k)|^2}{T}. \tag{40}$$

The double integral can be further reduced by observing that

$$|\tilde{w}(f+f_j-f_k)|^2 = |\tilde{w}(f)|^2 * \delta(f+f_j-f_k) = |\tilde{w}(f)|^2 * \left[\delta(f-f_j)\bigstar\delta(f-f_k)\right], \tag{41}$$

where the asterisk denotes convolution and the five-pointed star denotes cross correlation. (The cross correlation is defined by using two different variables in Equation 4, instead of the one variable *V*.) Equation 41 allows the double summation to be written as an autocorrelation of two single summations, convolved with the Fourier-transform magnitude-squared of the window function.

The next step is to interpret the meaning of the resulting three types of single summations. The first summation in Equation 40 is the easiest to interpret. The sum of the ensemble-averaged contributions to the irradiance is simply the total irradiance, which can be expressed in terms of the object's cross section σ through Equation 5, yielding

$$\sum_{j=1}^{N}\langle E_j\rangle = \frac{E_0}{4\pi R^2}\sigma.$$

The magnitude of the second summation depends on the number of surface cells N used in modeling the object. Note that, because the strength of the individual components $\langle E_j\rangle$ falls off as $1/N$ as the object is divided into smaller surface patches, the magnitude of the individual terms in the series goes as $1/N^2$. Because the series contains N terms, the magnitude of the summation is inversely proportional to N. Thus

$$\lim_{N\to\infty}\sum_{j=1}^{N}\langle E_j\rangle^2 = 0,$$

and we can drop this term because we are considering objects that have many uncorrelated scattering cells. The third summation can be made to resemble Equation 10 for the range-resolved laser radar cross section if it is converted to an integral by taking the limit of large N. The result is

$$\lim_{N\to\infty}\sum_{j=1}^{N}\langle E_j\rangle\,\delta(f-f_j) = \frac{E_0}{4\pi R^2}\frac{c}{2\gamma}U(z)\Big|_{z=\frac{c}{2\gamma}f}. \tag{42}$$

The factor involving the speed of light c and the scan rate γ arises from converting the δ-function from a function of frequency f to a function of range z.

The remaining quantity to be interpreted in Equation 40 is the Fourier-transform magnitude-squared of the window function, divided by the effective scan duration T. In the limit of large T, this function becomes a δ-function of frequency, and the convolution does not blur the signature. We define a related quantity that is a function of range z; namely,

$$W_z(z) = \frac{2\gamma}{c}\frac{|\tilde{w}(f)|^2}{T}\Big|_{f=\frac{2\gamma}{c}z}. \tag{43}$$

This quantity can be interpreted as the range-resolution impulse response of the system. In the limit as the scan bandwidth $B = \gamma T$ approaches infinity, this impulse response also reduces to a δ-function; i.e., $W_z(z) = \delta(z)$. Again, the factor of $2\gamma/c$ in Equation 43 accounts for converting the δ-function from a function of frequency to a function of range.

With the above observations, Equation 40 can be rewritten in the form

$$G_E(f)\Big|_{f=\frac{2\gamma}{c}z} = \left(\frac{E_0}{4\pi R^2}\right)^2 \times \frac{c}{2\gamma}\left[W_z(z)\,\sigma^2 + W_z(z) * R_U(z)\right], \tag{44}$$

where the autocorrelation function is given by

$$R_U(z) = \int_{-\infty}^{\infty} U(z')\,U(z+z')\,dz'.$$

We do not need to take the complex conjugate of the first $U(z)$ in the definition of $R_U(z)$, as in the general definition of an autocorrelation function given in Equation 4, because $U(z)$ is always real. In Equation 44, the spectral density of the fluctuating speckle irradiance consists of two terms: (1) a dc-like component that is proportional to the square of the object's total cross section σ, and (2) a term that is proportional to the convolution of the system impulse function $W_z(z)$ with the autocorrelation function $R_U(z)$ of the object's range-resolved laser radar cross section $U(z)$. Both components are multiplied by a factor that accounts for the received signal strength.

As the length of the scan increases, the system impulse function becomes more localized. This localization causes the dc component in Equation 44 to be more localized and improves the resolution to which the autocorrelation function $R_U(z)$ can be determined. Because the system impulse response reduces to a δ-function in the large-bandwidth limit, the convolution can be dropped in this limit. In general, however, the width of the impulse response determines the range resolution. As an illustration of Equation 43, we assume that the window function turns on and off abruptly. Then T is simply the time that it takes to complete the scan, and B is simply the total frequency scanned by the laser. The range-resolution impulse response evaluates to

$$W_z(z) = \frac{2B}{c}\,\mathrm{sinc}^2\left(\frac{2B}{c}\,z\right),$$

where $\mathrm{sinc}(x) = \sin(\pi x)/(\pi x)$. If we define the resolution Δz to be the value of z where the sinc function has its first null, i.e., $x = 1$, then

$$\Delta z = \frac{c}{2B}. \tag{45}$$

As expected, the range resolution improves as the scan bandwidth increases. (See the box entitled "Wavelength Decorrelation of Speckle" for a heuristic derivation of Equation 45.)

What makes the wavelength-decorrelation technique so powerful is that the high effective bandwidth of a tunable laser can be utilized to obtain range resolutions that far surpass conventional methods. For example, a range resolution of 1 mm can be achieved by scanning the laser over a bandwidth of 150 GHz. This bandwidth is a small frequency excursion for a tunable laser, and submillimeter range resolutions can readily be obtained. We use Equation 45 to define range resolution for arbitrary window shapes. In doing so we use the effective bandwidth B corresponding to the effective scan duration T defined in Equation 32.

The dc component in Equation 44 is associated with the fact that an intensity can never be negative. If the signal were ac coupled, or if the data were preprocessed by subtracting the mean, then this component would be eliminated. Let us denote the zero-mean signal by a prime; i.e.,

$$E'(t) = E(t) - \langle E(t)\rangle. \tag{46}$$

The Fourier transform of this signal also has zero mean and can be written in an analogous manner as

$$\tilde{E}'(f) = \tilde{E}(f) - \langle \tilde{E}(f)\rangle.$$

We can show that the spectral density of the zero-mean signal takes the form

$$G_{E'}(f)\Big|_{f=\frac{2\gamma}{c}z} = \left(\frac{E_0}{4\pi R^2}\right)^2 \frac{c}{2\gamma}\,W_z(z) * R_U(z). \tag{47}$$

As we can see from either Equation 44 or Equation 47, the spectral density of the speckle irradiance provides a way to measure the autocorrelation function $R_U(z)$ of an object's range-resolved laser radar cross

section to a resolution determined by the scan bandwidth. Note the strong similarity with imaging correlography, in which the two-dimensional spectral density of the speckle intensity pattern provides a measurement of the two-dimensional autocorrelation function of the object's brightness distribution function, and the resolution is determined by the total size of the detector array.

Random-Process Representation

In the above calculation of the spectral density of the fluctuating speckle signal, the complex amplitude $V(t)$ is represented by Equation 34, which is derived by using a discrete scattering-cell model. In the associated analysis we converted from summations to integrals by allowing the number of cells N to approach infinity. An alternative approach is introduced here that streamlines further analysis of statistical properties associated with the wavelength dependence of speckle. In this approach we construct a representation of the random process $V(t)$ in which the limiting operation has already been performed. Thus the new representation of $V(t)$ is based on an underlying random process that is continuous, not discrete, as is ϕ_j.

In constructing this new representation, we first define an auxiliary complex amplitude $V_s(t)$ that is similar to $V(t)$ but stationary. Stationarity means that statistical moments, such as the average and the autocorrelation function, are independent of offsets in time. Because the nonstationarity in $V(t)$ arises from the time dependence of the transmitted signal, it can be removed by dividing Equation 34 by the time variation associated with $V_T(t - t_0)$. Thus

$$V_s(t) = \lim_{N\to\infty} \sum_{j=1}^{N} \sqrt{\langle E_j \rangle} \times \exp\left\{ i\left[\phi_T(t - t_0 - t_j) - \phi_T(t - t_0) + \phi_j \right] \right\}$$

and

$$V(t) = \sqrt{w(t - t_0)}\, \exp\left\{ i\left[\phi_T(t - t_0) \right] \right\} V_s(t). \quad (48)$$

Our objective is to construct a new representation for $V_s(t)$ that does not require the limiting procedure. To construct this representation, we must first know the statistical properties of $V_s(t)$ that are to be duplicated. Because the complex amplitude is a superposition of many independent contributions, and because none of these contributions dominates, the central limit theorem applies, and the real and imaginary parts of $V_s(t)$ are normally distributed. A unique property of a normal, or Gaussian, random process is that it is completely determined by its first-order and second-order moments. The first-order moment is simply the mean, which by Equation 39 is

$$\langle V_s(t) \rangle = 0. \quad (49)$$

Two types of second-order moments must be considered. One is the usual statistical autocorrelation function, defined as

$$R_{V_s}(t) = \left\langle V_s^*(t')\, V_s(t + t') \right\rangle,$$

and the other does not include the complex conjugation. These two second-order moments behave quite differently. In particular, the second type vanishes, regardless of the arguments; i.e.,

$$\langle V_s(t')\, V_s(t + t') \rangle = 0. \quad (50)$$

Equation 50 indicates that $V_s(t)$ is circular. Circularity means that the real and imaginary parts of the random process are uncorrelated and have equal variance [33–36]. Consequently, contours of constant probability are concentric circles centered on the origin of the complex plane. (A nonzero-mean random process can also be circular, but the contours of equal probability are centered around its mean.) In the theory of speckle, the assumptions we have made about ϕ_j lead to what is known as *Gaussian speckle* [33, 34], or more precisely, to a complex amplitude of the optical field that is represented by a zero-mean, complex circular Gaussian random process.

Equation 50 follows directly from a similar property for the random process ϕ_j; namely,

$$\left\langle \exp\left[i(\phi_j + \phi_k) \right] \right\rangle = 0. \quad (51)$$

As in Equation 38, the expected value in Equation 51 vanishes when the indices are unequal, but here it also vanishes when the indices are equal because the two phases are not subtracted and do not cancel. If the

phases were subtracted, then the expected value would be unity when the indices were equal. Therefore, this expected value can be expressed as a Kronecker delta function; i.e.,

$$\left\langle \exp\left[i(\phi_j - \phi_k)\right]\right\rangle = \delta_{jk}\,. \tag{52}$$

We use Equation 52 to evaluate the autocorrelation function $R_{V_s}(t)$, yielding

$$R_{V_s}(t) = \lim_{N\to\infty} \sum_{j=1}^{N} \left\langle E_j \right\rangle \exp(-i2\pi f_j t)\,. \tag{53}$$

The next step is to express Equation 53 in terms of the range-resolved laser radar cross section $U(z)$. This can be accomplished by noticing that the left side of Equation 42 is the Fourier transform of the right side of Equation 53, to within a sign flip in the frequency argument. Thus the autocorrelation function $R_{V_s}(t)$ can be written as

$$R_{V_s}(t) = \frac{E_0}{4\pi R^2}\,\tilde{U}(f_z)\Big|_{f_z=\frac{2\gamma}{c}t}\,, \tag{54}$$

where the Fourier transform

$$\tilde{U}(f_z) = \int_{-\infty}^{\infty} U(z)\exp(-i2\pi f_z z)\,dz$$

is a function of spatial frequency. Because time and spatial frequency are related by a proportionality constant through

$$f_z = \frac{2\gamma}{c}\,t\,,$$

the fluctuating speckle intensity can be represented either as a function of spatial frequency or as a function of time.

The random process $V_s(t)$ has now been completely characterized. In summary, it is a stationary complex Gaussian random process that is zero mean (Equation 49) and circular (Equation 50), and whose autocorrelation function is proportional to $\tilde{U}(f_z)$ (Equation 54). Our new representation of $V_s(t)$ is obtained by requiring that all of these specifications hold. This representation is

$$V_s(t) = \sqrt{\frac{E_0}{4\pi R^2}} \times \int_{-\infty}^{\infty} \sqrt{U(z)}\,g(z)\exp\left(-i2\pi f_z z\right)dz\Big|_{f_z=\frac{2\gamma}{c}t}\,, \tag{55}$$

where $g(z)$ is a stationary complex Gaussian random process that is zero mean,

$$\left\langle g(z)\right\rangle = 0\,, \tag{56}$$

circular,

$$\left\langle g(z')\,g(z+z')\right\rangle = 0\,, \tag{57}$$

and δ-correlated,

$$\left\langle g^*(z')\,g(z+z')\right\rangle = \delta(z)\,. \tag{58}$$

By using Equations 56, 57, and 58, we can verify that Equation 55 satisfies Equations 49, 50, and 54, respectively. We also know that the new representation is Gaussian because a linear combination of Gaussian random processes remains Gaussian.

We now provide an interpretation of the various components in Equation 55. The integration represents a summation over the contributions to $V_s(t)$ from different range planes. The strength of the contribution to the complex amplitude $V_s(t)$ from a given plane is proportional to the square root of the laser radar cross section associated with that plane. Hence, there is a square root of $U(z)$ in Equation 55. The factor $g(z)$ converts the contribution from the plane located at range z into a complex Gaussian random process to account for the fact that the speckle from the individual range planes is Gaussian. The complex exponential introduces time-varying fluctuations in the relative phase delay between range planes. These fluctuations are induced by changing the laser frequency, as explained in the box entitled "Wavelength Decorrelation of Speckle." In effect, scanning the laser frequency linearly in time results in a Fourier transformation of the quantity $\sqrt{U(z)}\,g(z)$. We see that Fourier transforms play a fundamental role in the wavelength dependence of speckle, as well as in its spatial depencence.

Equation 55 is convenient for statistical calculations. It can be manipulated, either analytically or by

computer simulation, to study input-output relations associated with a given signal processing algorithm or to study higher-order statistics such as the bispectrum, without first going through the discrete scattering-cell argument. To carry out this type of analysis, we must know the corresponding moments of the random process $g(z)$. These moments can be evaluated by applying the complex Gaussian moment theorem [37] to a δ-correlated, zero-mean random process. All odd-order moments of $g(z)$ vanish, as do all even-order moments that do not have an equal number of conjugated and nonconjugated variables. The remaining moments obey the general rule

$$\left\langle g^*(z_1)\, g^*(z_2) \cdots g^*(z_M)\, g(z_{M+1}) \cdots g(z_{2M}) \right\rangle = \sum_{\pi} \delta(z_1 - z_{M+p})\, \delta(z_2 - z_{M+q}) \cdots \delta(z_M - z_{M+r}), \tag{59}$$

where π denotes a summation over the $M!$ possible permutations $(p, q, \ldots, r)$ of $(1, 2, \ldots, M)$. Equation 59 reduces to Equation 58 for $M = 1$ and to

$$\left\langle g^*(z_1)\, g^*(z_2)\, g(z_3)\, g(z_4) \right\rangle = \delta(z_1 - z_3)\, \delta(z_2 - z_4) + \delta(z_1 - z_4)\, \delta(z_2 - z_3) \tag{60}$$

for $M = 2$. Equation 60 is analogous to Equation 38 and is used in deriving Equation 44 when using the continuous random process $g(z)$ instead of the discrete random process ϕ_j.

Coherent Detection

By Equation 44, spectral analysis of the fluctuating speckle irradiance $E(t) = |V(t)|^2$ provides the autocorrelation function $R_U(z)$ of the object's range-resolved laser radar cross section $U(z)$. But Equation 55 for the random-process representation of $V_s(t)$ is written in terms of $U(z)$. This leads us to the hypothesis that $U(z)$ is recoverable through appropriate analysis of the complex-valued return signal $V(t)$. However, optical frequencies are so high (300 THz for a wavelength of 1 μm) that the rapid phase fluctuations associated with $V(t)$ cannot be measured directly. Optical detectors generally measure the magnitude-squared of $V(t)$; to obtain the phase of $V(t)$ we must use coherent detection.

Heterodyne detection is the most common form of coherent detection. In heterodyne detection the return signal is mixed with a monochromatic reference beam that is shifted in frequency. The resulting irradiance has four terms: (1) the irradiance of the return signal, (2) the irradiance of the reference beam, (3) a cross term produced by multiplying the complex amplitude of the return signal with the complex conjugate of the complex amplitude of the reference beam, and (4) a cross term that is the complex conjugate of the third term. The Fourier components of the first two terms are centered around the dc and have a small spread in frequency. Because the reference beam is shifted in frequency, the Fourier transforms associated with the two cross terms are also shifted in frequency. This frequency shift is in opposite directions for the two terms. If the frequency shift is large enough, the two cross terms are separated from each other and from the first two terms. Then a high-pass filter can be used to select one of these two cross terms. The cross terms carry the desired information, because they are equivalent to the return signal, except for having a much lower carrier frequency that can be handled electronically.

The first inclination might be to implement wavelength decorrelation by using heterodyne detection because it would eliminate the high-frequency phase fluctuations that occur at the carrier frequency. Heterodyne detection, however, is actually a poor choice. We explain this by referring to Equation 47 for direct detection. In that equation the desired quantity $R_U(z)$ is convolved with an impulse response function that is essentially a spectral density of the window function. As we show below, a similar convolution arises in the analysis of coherent detection. In either case, to obtain a high range resolution, the impulse response should be as narrow as possible, and hence the spectral density of the corresponding window function should contain only low-frequency components.

In direct detection, the phase fluctuations $\phi_T(t)$ associated with the transmitted signal are not measured. Hence the window function is smooth, with little high-frequency content. In heterodyne detection, however, the phase fluctuations introduce high-

frequency oscillations, with the maximum frequency equal to the chirp rate γ multiplied by the scan duration T. To see what this frequency γT corresponds to in range, we multiply it by the scaling factor $c/(2\gamma)$, which yields an impulse response with a total width of approximately $Tc/2$. Except for extremely short scan durations, the range resolution is large compared to the object's total range extent! Thus a monochromatic reference beam is useless for measuring the range-resolved laser radar cross section.

From the above discussion, we see that the rapid phase variations must be eliminated to obtain the optimal range resolution. The way to eliminate these variations is to multiply the complex phase exponential in Equation 48 by its complex conjugate $\exp[-i\phi_T(t - t_0)]$. This multiplication corresponds to mixing the return signal $V(t)$ with a reference beam that is a copy of the transmitted signal delayed by the round-trip transit time t_0. (We set the window function $w(t)$ for the reference signal to unity.) Actually, we still need a constant frequency shift in the reference beam to separate the desired cross-correlation term from the other three terms in the expression for the resulting irradiance. This frequency shift can be incorporated mathematically by assuming that the range plane from which t_0 is measured lies outside the object by a certain minimum distance. As illustrated in the box entitled "Range-Reference Planes," this minimum distance is equal to the range extent of the illuminated portion of the object. The coherent-detection approach just described also corresponds to matched filtering and stretched processing [38].

We are now in a position to write the random-process representation for the coherently detected signal. Because we are dealing with complex amplitudes rather than intensities, we change the notation for the window function to the quantity $a(t) = \sqrt{w(t)}$. Then the coherently detected signal can be written as

$$\begin{aligned} V_c(t) &= V(t)\exp[i\phi_T(t - t_0)] \\ &= \sqrt{\frac{E_0}{4\pi R^2}}\, a(t - t_0) \\ &\quad \times \int_{-\infty}^{\infty} \sqrt{U(z)}\, g(z)\exp(-i2\pi f_z z)\, dz\Big|_{f_z = \frac{2\gamma}{c}t}. \end{aligned} \tag{61}$$

The spectral density for the coherently detected signal is

$$G_{V_c}(f) = \frac{\left\langle \left|\tilde{V}_c(f)\right|^2 \right\rangle}{T_a},$$

where the effective scan duration is

$$T_a = \int_{-\infty}^{\infty} |a(t)|^2\, dt.$$

By using the random-process representation given in Equation 61 and by applying the fact that the underlying random process $g(z)$ is δ-correlated (Equation 58), we can write the spectral density in the form

$$G_{V_c}(f)\Big|_{f=-\frac{2\gamma}{c}z} = \frac{E_0}{4\pi R^2}\frac{c}{2\gamma}\, A_z(z) * U(z), \tag{62}$$

where

$$A_z(z) = \frac{2\gamma}{c}\frac{\left|\tilde{a}(f)\right|^2}{T_a}\Bigg|_{f=-\frac{2\gamma}{c}z}$$

is the range-resolution impulse response of the system. As before, the impulse response reduces to a δ-function in the large scan bandwidth limit, and the convolution with the impulse response can be dropped in Equation 62 in this limit. Thus the spectral density of the coherently detected signal provides a measurement of the object's range-resolved laser radar cross section $U(z)$, not just the autocorrelation function $R_U(z)$. We can also arrive at this conclusion for coherent detection by beginning with the result given in Equation 44 for direct detection and incorporating the reference signal by including a δ-function to represent the range-resolved laser radar cross section of the reference signal. We describe how this is done in the box entitled "Range-Reference Planes."

Note that Equation 62 contains a sign flip between the frequency f and the range z for coherent detection, but there is no sign flip in Equation 47 for direct detection. Actually, Equation 47 could have been written with the sign flip, because the spectral density is an even function for direct detection. Thus the rela-

tion between frequency and range

$$f = -\frac{2\gamma}{c} z \tag{63}$$

actually covers both situations. The sign flip in Equation 63 is associated with the fact that Equation 55 occurs with a negative sign in the complex exponential, but we need a positive sign to make the integral look like an inverse Fourier transform of a function of frequency.

We have shown that the range resolution is poor if the phase of the reference beam is inaccurate. The longer the frequency scan, the harder it is to maintain the required accuracy, and long scans are necessary for high range resolutions. If the distance to the object is relatively short, then we can produce the reference beam by using a beam splitter and sending this beam through an appropriate delay line before recombining it with the return signal. (A variation of this technique that uses a range-reference plane located near the object is explained in the box on range-reference planes and demonstrated in the section describing wavelength-decorrelation measurements.) The coherent-detection approach may not be feasible, however, for the large propagation distances associated with a remote-sensing application. An additional complication is that the time delay varies if a target is moving radially. Because of these difficulties, we have chosen to investigate direct-detection-based methods for recovering $U(z)$.

Bispectral Analysis

In considering how the direct-detection wavelength-decorrelation technique could be extended to the measurement of $U(z)$, we note by the autocorrelation theorem that $R_U(z)$ contains the same information as the magnitude of the Fourier transform of $U(z)$. If we also knew the phase $\phi(f_z)$, which is defined such that

$$\tilde{U}(f_z) = \left|\tilde{U}(f_z)\right| \exp\left[i\phi(f_z)\right], \tag{64}$$

then $\tilde{U}(f_z)$ would be completely determined, and $U(z)$ could be found through inverse Fourier transformation. Therefore, methods that yield $U(z)$ must provide the Fourier phase information. We would be particularly interested if $\phi(f_z)$ could be found by processing the speckle intensity data. Then the hardware complexities and other difficulties associated with coherent detection could be traded off for more sophisticated signal processing.

There are two general approaches for obtaining phase information from the intensity signal. The first approach is to take the autocorrelation function $R_U(z)$, obtained from calculating the spectral density, and attempt to recover the phase by applying well-known iterative phase-retrieval algorithms [39, 40]. In these algorithms, known constraints are applied iteratively in the spatial and Fourier-transform domains. The constraints in the spatial domain are that $U(z)$ is a non-negative function with finite support, i.e., zero-valued outside of its range extent. In the Fourier-transform domain, the constraint is that the Fourier magnitude is known. Iterative phase retrieval has been applied to wavelength-decorrelation data in Reference 19 with good success, but in general the method is not guaranteed to converge to the correct solution, and it does not utilize all of the available information. Because of these reasons we began to investigate other methods for recovering $\phi(f_z)$.

The second general approach is to analyze the original data by using more sophisticated signal processing techniques, in the hope that additional information about the phase can be extracted from the intensity signal. The basis for this optimism is that $U(z)$ appears explicitly in Equation 55, and that information about the Fourier phase $\phi(f_z)$ may have been lost in taking the magnitude-squared when we calculated the spectral density defined by Equation 31. Now that we have a statistical representation of the signal, we can test any potential signal processing algorithm to see if it yields more information about the Fourier phase. The first inclination might be to modify Equation 31 by not taking the magnitude when squaring, or to use different frequency arguments for the two factors. But we can show that the spectral density is the only second-order moment of $\tilde{E}(f)$ that is non-zero. The next logical choice is to calculate a third-order moment.

The bispectral density is a third-order moment, and it is the natural extension of the spectral density to two dimensions [41–43]. (The application of

RANGE-REFERENCE PLANES

IN THE TECHNIQUE of wavelength decorrelation, the spectral density of the fluctuating speckle-intensity signal provides the autocorrelation function $R_U(z)$ of the target's range-resolved laser radar cross section $U(z)$. By making a simple alteration to the laboratory apparatus, we can obtain $U(z)$ directly. This alteration involves placing a range-reference plane either in front of or behind the target. We can explain the basis for the range-reference-plane technique from the point of view of either direct detection or coherent detection.

Let us first consider direct detection. Assume that a range-reference ring is located behind the target at position z_0, as illustrated at the top of Figure A. This reference ring produces a sharp spike, or a δ-function, in the black $U(z)$ curve shown in the center of Figure A. As usual, the spectral density of the directly detected signal produces the autocorrelation function of $U(z)$, but $U(z)$ now contains the additional δ-function component. In calculating the autocorrelation function for this combination, we (1) choose a range-offset value, say z_a, (2) replicate the original $U(z)$ function with a range offset equal to z_a, as shown by the red curve, (3) multiply the original curve and the shifted curve point by point to obtain a product curve, and (4) integrate to obtain the area under this product curve. This procedure yields the value of the autocorrelation function of the target reference-plane combination for the particular range offset z_a, as illustrated by the red point at the bottom of Figure A. We repeat this procedure for different values of range offset to fill out the autocorrelation-function curve.

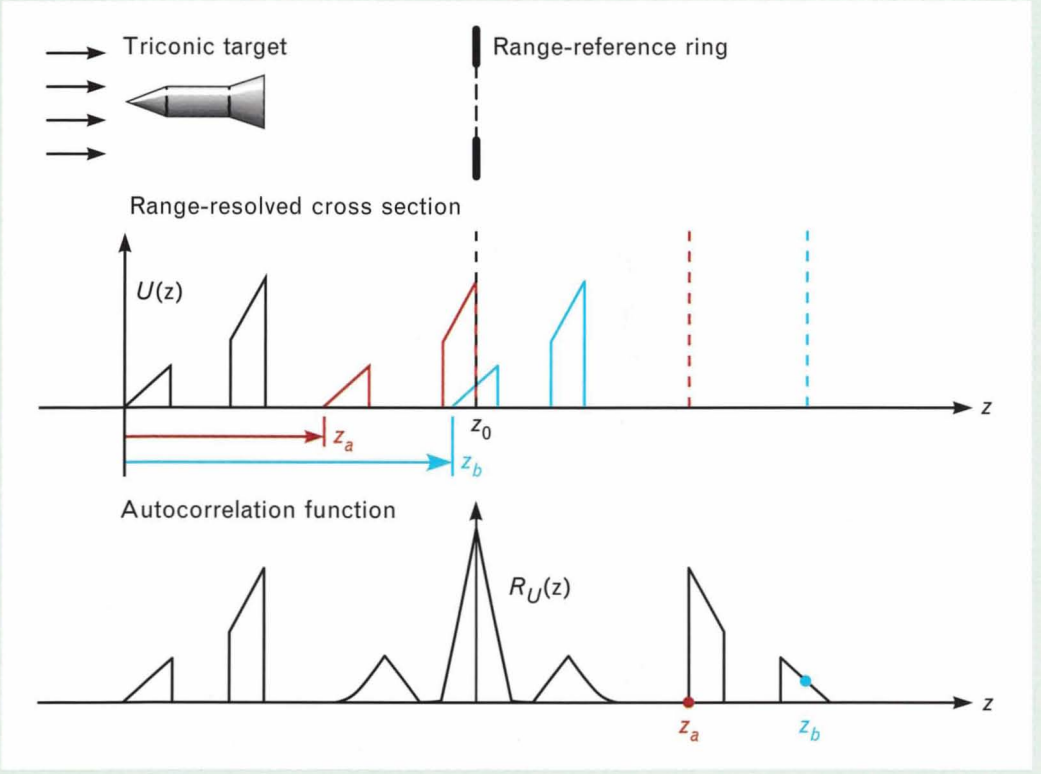

FIGURE A. Pictorial illustration of how a range-reference plane produces the range-resolved laser radar cross section.

For range offsets lying between z_a and z_0, the δ-function traces through the $U(z)$ curve for the triconic and replicates its functional form. Observe that the range-reference plane must be separated from the target by a distance greater than the target's range extent L, or the desired $U(z)$ curve will overlap with the central autocorrelation curve $R_U(z)$. Because autocorrelation functions of real quantities are even functions, the replicated $U(z)$ curves on either side of the origin are mirror images of each other. If the reference plane is located behind the target, as depicted in Figure A, then the $U(z)$ curve on the left side has the correct orientation; if the reference plane is located in front of the target, then we must choose the curve on the right side.

From the coherent-detection point of view, the range-reference ring produces a delayed copy of the transmitted signal, which follows the same path through the optical system as the signal from the target. Because these two signals mix coherently at the receiver, we can apply the coherent-detection result given in Equation 62. In summary of this result, coherent detection yields the range-resolved laser radar cross section $U(z)$ of the target, provided that the reference beam is sufficiently offset in frequency so that the desired spectral components can be separated from the undesired spectral components by high-pass filtering.

Let us examine further the meaning of having a sufficient offset in frequency. Let t_0 be the time delay between contributions coming from the origin of the coordinate system (which is located at the tip of the triconic) and the reference plane (which is located at z_0). Because these points are separated in range by a distance z_0, the time delay is $t_0 = 2z_0/c$. A frequency shift of $\Delta\nu_0 = \gamma t_0$ is induced between the two contributions because the laser frequency scans at the rate γ during this time delay. This frequency shift corresponds to the frequency shift normally associated with heterodyne detection. (Our situation differs from what is normally considered to be heterodyne detection because the frequency of the laser, and hence of the reference beam, changes with time. The frequency shift remains constant, however.) As with heterodyne detection, the frequency shift must be large enough to separate the desired Fourier components (produced by mixing the reference signal with the target signal) from the undesired Fourier components associated with the return signal from the target alone. The desired Fourier components correspond to $U(z)$ and its mirror image at the bottom of Figure A, and the undesired Fourier components correspond to the central autocorrelation region. The minimum frequency offset corresponds to a range-reference-plane offset z_0 that is separated from the target by a distance at least as large as the target's range extent L.

bispectral signal processing to wavelength-decorrelation data is described in detail in Reference 19. The results from this work are summarized here.) As with the spectral density, the final results are simpler if central moments are calculated. Consequently, we deal with the zero-mean speckle irradiance $E'(t)$ defined in Equation 46. The bispectral density of $E'(t)$ is defined as

$$G^{(3)}_{E'}(f_1, f_2) = \frac{\left\langle \tilde{E}'(f_1)\tilde{E}'(f_1)\tilde{E}'^{*}(f_1 + f_2)\right\rangle}{T^{(3)}}, \quad (65)$$

where the effective scan duration is

$$T^{(3)} = \int_{-\infty}^{\infty} |w(t)|^2 w(t)\, dt\,.$$

If the window function turns on and off abruptly, then $T^{(3)} = T$. But in general, $T^{(3)} \leq T$, because the window function is everywhere less than or equal to unity in our interpretation.

Before evaluating Equation 65 by using the random-process representation, we give some background and some additional information that might provide the motivation to consider bispectral analysis when trying to recover the phase information. For a deter-

ministic function, we define the bispectrum without dividing by a normalization factor. Additionally, the ensemble-average brackets are unnecessary. Thus the bispectrum of the window function $w(t)$ is

$$G_w^{(3)}(f_1, f_2) = \tilde{w}(f_1)\,\tilde{w}(f_2)\,\tilde{w}^*(f_1 + f_2). \quad (66)$$

Equation 66 is a general definition that also applies to complex-valued functions. Note that evaluation of the bispectrum along either the f_1 axis or the f_2 axis yields a result proportional to the spectrum $|\tilde{w}(f)|^2$. We can show that Equation 66 forms a two-dimensional Fourier-transform pair with the triple-correlation function of $w(t)$, which is defined as

$$R_w^{(3)}(t_1, t_2) = \int_{-\infty}^{\infty} w^*(t')\,w(t_1 + t')\,w(t_2 + t')\,dt'. \quad (67)$$

We see that the effective scan duration $T^{(3)}$ equals the value that the triple correlation of the window function takes at its origin. There is a natural extension of Equations 66 and 67 to higher dimensions. In extending Equation 66, the Fourier transform is repeated for each new argument, the last component is complex conjugated, and its argument is the sum of the frequency arguments of the other components. Equation 67 is extended to higher dimensions by repeating the window function, with corresponding time offsets in the argument.

The triple correlation and the bispectrum are plotted in Figure 21 for the range-resolved laser radar cross section of a triconic. Note that the major axis of the triple correlation points in a direction 45° above the horizontal axis, but that the major axis of the bispectrum is rotated by 90°. This result is expected for a two-dimensional Fourier-transform pair. Also note that if a function has finite support, then its triple correlation also has finite support, being confined to a hexagonal region as illustrated in Figure 21(a). Additionally, if the function is non-negative, then its triple correlation function is also non-negative. Some other properties, which are related to the real-valuedness of $U(z)$, are evident in Figure 21; namely, the triple-correlation function is real-valued, and the real and imaginary parts of the bispectrum are point-symmetric and anti-point-symmetric around the origin, respectively.

A motivating factor for considering bispectral analysis is that the Fourier phase of a function can be reconstructed, to within a linear phase factor, from knowledge of the phase of its bispectrum. Consequently, if there were some way of processing the speckle-intensity data that provided the bispectrum of $U(z)$, then we could recover the phase $\phi(f_z)$ to within a linear phase factor and reconstruct $U(z)$ to within an arbitrary range offset.

Let us take a closer look at the relation between $U(z)$ and its bispectrum. If the bispectrum is written in the form

$$G_U^{(3)}(f_{z_1}, f_{z_2}) = \left|G_U^{(3)}(f_{z_1}, f_{z_2})\right| \exp\left[i\psi(f_{z_1}, f_{z_2})\right],$$

then Equation 64 can be substituted into the definition of the bispectrum to relate its magnitude to the Fourier magnitude of $U(z)$ through

$$\left|G_U^{(3)}(f_{z_1}, f_{z_2})\right| = \left|\tilde{U}(f_{z_1})\right|\left|\tilde{U}(f_{z_2})\right|\left|\tilde{U}(f_{z_1} + f_{z_2})\right| \quad (68)$$

and its phase to the Fourier phase of $U(z)$ through

$$\psi(f_{z_1}, f_{z_2}) = \phi(f_{z_1}) + \phi(f_{z_2}) - \phi(f_{z_1} + f_{z_2}). \quad (69)$$

Equation 69 is a key result because it provides the basis for recovering the Fourier phase (which will be described below). We note that because $U(z)$ is a real function, the magnitude is symmetric around the origin and the phase is antisymmetric around the origin.

Let us now investigate the possibility of obtaining the bispectrum of $U(z)$ from the intensity data. First, recall that the spectral density of the zero-mean speckle intensity $E'(t)$ provided the autocorrelation function of $U(z)$. Because the bispectral density is an extension of the spectral density to two dimensions, we expect that the bispectral density of $E'(t)$ will provide us

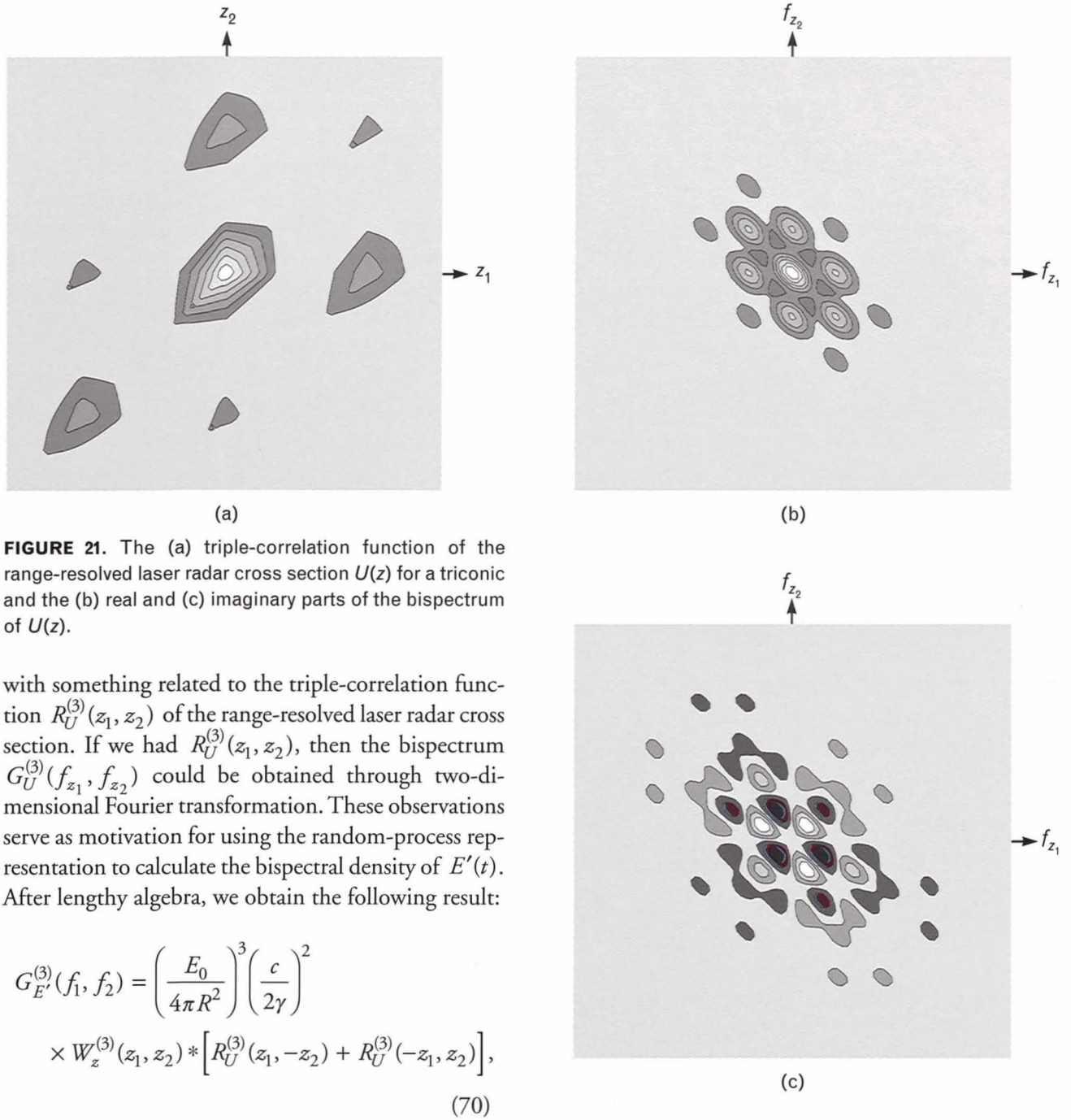

FIGURE 21. The (a) triple-correlation function of the range-resolved laser radar cross section $U(z)$ for a triconic and the (b) real and (c) imaginary parts of the bispectrum of $U(z)$.

with something related to the triple-correlation function $R_U^{(3)}(z_1, z_2)$ of the range-resolved laser radar cross section. If we had $R_U^{(3)}(z_1, z_2)$, then the bispectrum $G_U^{(3)}(f_{z_1}, f_{z_2})$ could be obtained through two-dimensional Fourier transformation. These observations serve as motivation for using the random-process representation to calculate the bispectral density of $E'(t)$. After lengthy algebra, we obtain the following result:

$$G_{E'}^{(3)}(f_1, f_2) = \left(\frac{E_0}{4\pi R^2}\right)^3 \left(\frac{c}{2\gamma}\right)^2 \times W_z^{(3)}(z_1, z_2) * \left[R_U^{(3)}(z_1, -z_2) + R_U^{(3)}(-z_1, z_2)\right], \tag{70}$$

where

$$W_z^{(3)}(z_1, z_2) = \left(\frac{2\gamma}{c}\right)^2 \frac{G_w^{(3)}(f_1, f_2)}{T^{(3)}} \tag{71}$$

is the bispectral range-resolution impulse-response function. Again, frequency and range are related by Equation 63. The normalization factor in Equation 71 has been chosen such that the integrated area under the $W_z^{(3)}(z_1, z_2)$ curve is unity, independent of the choice of the window function. As the effective scan length $T^{(3)}$ increases, the impulse-response function becomes more and more localized and reduces to $\delta(z_1)\,\delta(z_2)$ in the large-bandwidth limit. Thus the convolution with $W_z^{(3)}(z_1, z_2)$ can be dropped from Equation 70 in this limit.

Equation 70 is an interesting result that requires

further explanation. As expected, it does involve the triple-correlation function $R_U^{(3)}(z_1, z_2)$, but in an unusual form. First, note that there is a sign flip on one of the two arguments in each of the two triple-correlation functions. This sign flip might have been expected because the major axes of a bispectrum and a triple-correlation point in perpendicular directions (as illustrated in Figure 21) and the two types of functions are being equated. Also, note that the argument list for the second triple correlation is the negative of the argument list for the first triple correlation. Thus these two functions are rotated by 180° around the origin with respect to each other. Consequently, their sum is point-symmetric around the origin. This result might also have been expected because the real part of the bispectrum of a real function is point-symmetric around the origin.

The next step is to take the two-dimensional Fourier transform of the right-hand side of Equation 70 to see what information can be obtained about the bispectrum of $U(z)$. The Fourier transform of the point-symmetric triple-correlation function is equal to twice the real part of the bispectrum. By applying the convolution theorem we obtain

$$\int_{-\infty}^{\infty}\int_{-\infty}^{\infty}\left\{W_z^{(3)}(z_1, z_2) * \left[R_U^{(3)}(z_1, -z_2) + R_U^{(3)}(-z_1, z_2)\right]\right\} \times \exp\left[-i2\pi(f_{z_1} z_1 + f_{z_2} z_2)\right] dz_1\, dz_2 = \tilde{W}_z^{(3)}(f_{z_1}, f_{z_2})\; 2\,\mathrm{Re}\left[G_U^{(3)}(f_{z_1}, -f_{z_2})\right]. \tag{72}$$

In the large-bandwidth limit, $\tilde{W}_z^{(3)}(f_{z_1}, f_{z_2})$ tends to unity and can be dropped from Equation 72. In summary, to this point we have shown that by calculating the bispectral density of the zero-mean intensity signal $E'(t)$ and then Fourier transforming, we can measure the real part of the bispectrum of $U(z)$.

To deduce information about the Fourier phase $\phi(f_z)$ from Equation 69 we must know the phase $\psi(f_{z_1}, f_{z_2})$ of the bispectrum of $U(z)$, but Equation 72 provides only the real part of the bispectrum. Fortunately, we have more information at our disposal. Because the Fourier magnitude of $U(z)$ can be determined by the original spectral-density method, it can be substituted into Equation 68 to determine the magnitude of the bispectum of $U(z)$. Once both the magnitude and the real part of the bispectrum are known, the imaginary part can be determined to within a plus or minus sign ambiguity. Figure 22 illustrates the situation graphically in the complex plane. In this figure, the circle represents the magnitude of the bispectrum for a given value of its arguments and the vertical line represents its real part. The two intersection points represent the two possible solutions for the imaginary part. We see that the imaginary part has been determined within a sign ambiguity or, equivalently, that the absolute value of the phase $\psi(f_{z_1}, f_{z_2})$ has been determined. The corresponding mathematical relation is

$$\left|\psi(f_{z_1}, f_{z_2})\right| = \cos^{-1}\left\{\frac{\mathrm{Re}\left[G_U^{(3)}(f_{z_1}, f_{z_2})\right]}{\left|G_U^{(3)}(f_{z_1}, f_{z_2})\right|}\right\}.$$

In general, the sign of the phase $\psi(f_{z_1}, f_{z_2})$ changes as a function of the spatial-frequency coordinates.

Next, we investigate potential algorithms, based on Equation 69, for recovering Fourier phase information. In conventional applications of the bispectrum, both the absolute value and the sign of the phase are known. As background for our method, we consider two algorithms developed for conventional applica-

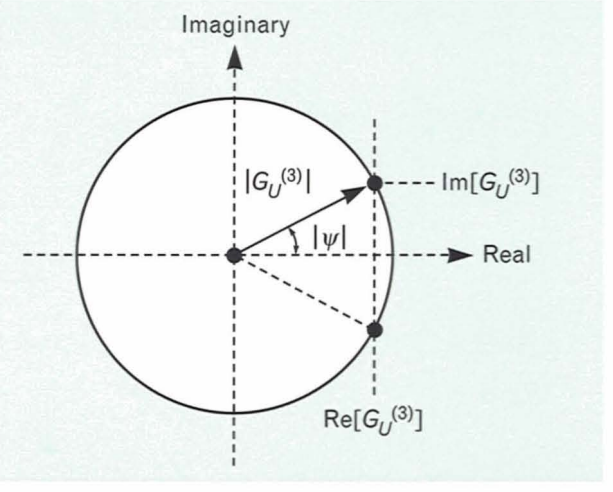

FIGURE 22. Representation of the real and the imaginary parts of the bispectrum in the complex plane. Knowledge of both the magnitude and the real part of the bispectrum determines the imaginary part to within a sign ambiguity.

tions. In practice, the phase of the bispectrum is sampled at discrete points (m, n) on a grid in spatial-frequency space so that Equation 69 can be written in the form

$$\psi_{m,n} = \phi_m + \phi_n - \phi_{m+n} . \tag{83}$$

The first algorithm is recursive [44]. It uses Equation 83 to build up the values of ϕ_{m+n} for larger indices $m+n$ from knowledge of $\psi_{m,n}$. It is based on the fact that ϕ_{m+n} can be expressed in terms of ϕ_0, ϕ_1, and $\psi_{m,n}$. By symmetry, $\phi_0 = 0$ but ϕ_1 cannot be determined. This lack of knowledge about ϕ_1 introduces an unknown linear phase factor in the reconstructed phase, which corresponds to an arbitrary offset in the function being reconstructed. (This offset is inherent in all bispectrum-based methods.) Besides being sensitive to noise and to missing elements in the $\psi_{m,n}$ array, the recursive algorithm cannot be implemented in our situation because the sign of $\psi_{m,n}$ is unknown.

The second algorithm was proposed more recently [45]. It performs least-squares minimization of the difference, modulo 2π, between the right and left sides of Equation 83. The function to be minimized is

$$F_1(\psi, \hat{\phi}, b) = \sum_{m,n} \left\{ \text{mod } 2\pi \left[\psi_{m,n} - (\hat{\phi}_m + \hat{\phi}_n - \hat{\phi}_{m+n}) \right] b_{m,n} \right\}^2 , \tag{84}$$

where $b_{m,n}$ is a weighting function, and the circumflexes denote quantities that are to be varied to minimize F_1. To apply Equation 84 to our situation, we would need to recover the sign of the bispectrum phase. One approach for doing so might be to use two-dimensional iterative phase retrieval. The constraints in the spatial domain are that the triple-correlation function is non-negative and has finite support; in the Fourier domain the bispectrum is known to within a sign ambiguity. There are two solutions to the sign-retrieval problem that differ by a global sign change. This ambiguity in the overall sign is a result of not being able to determine the sign of the imaginary part of the bispectrum. Thus this ambiguity is inherent in our phase-retrieval problem. It corresponds to an uncertainty as to whether the object is pointing toward or away from the observer. The ambiguity might be resolved by inspection of the functional form of $U(z)$ or by use of a low-resolution radar.

Recovering the sign of $\psi_{m,n}$ by using two-dimensional phase retrieval is a computationally intensive process. Consequently, we investigated the possibility of recovering the Fourier phase directly from the absolute value of the bispectrum phase. We found that this phase determination can be accomplished by making a slight modification to Equation 84. This modification is based on the following reasoning. If we take the absolute value of each side of Equation 83, then the resulting equation is still true. Thus we write

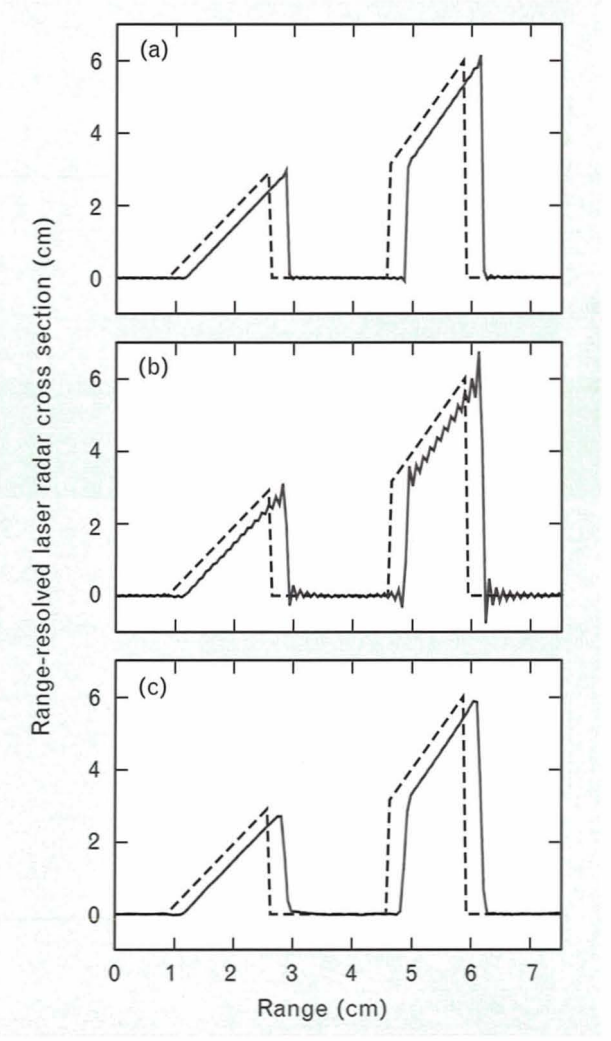

FIGURE 23. Reconstruction of the range-resolved laser radar cross section of a 5-cm-long triconic after recovery of the Fourier phase through minimization of (a) F_1 and (b) F_2. A low-pass filtered version of part *b* is shown in (c). The theoretical curves, represented by dashed lines, are shifted for the sake of comparison.

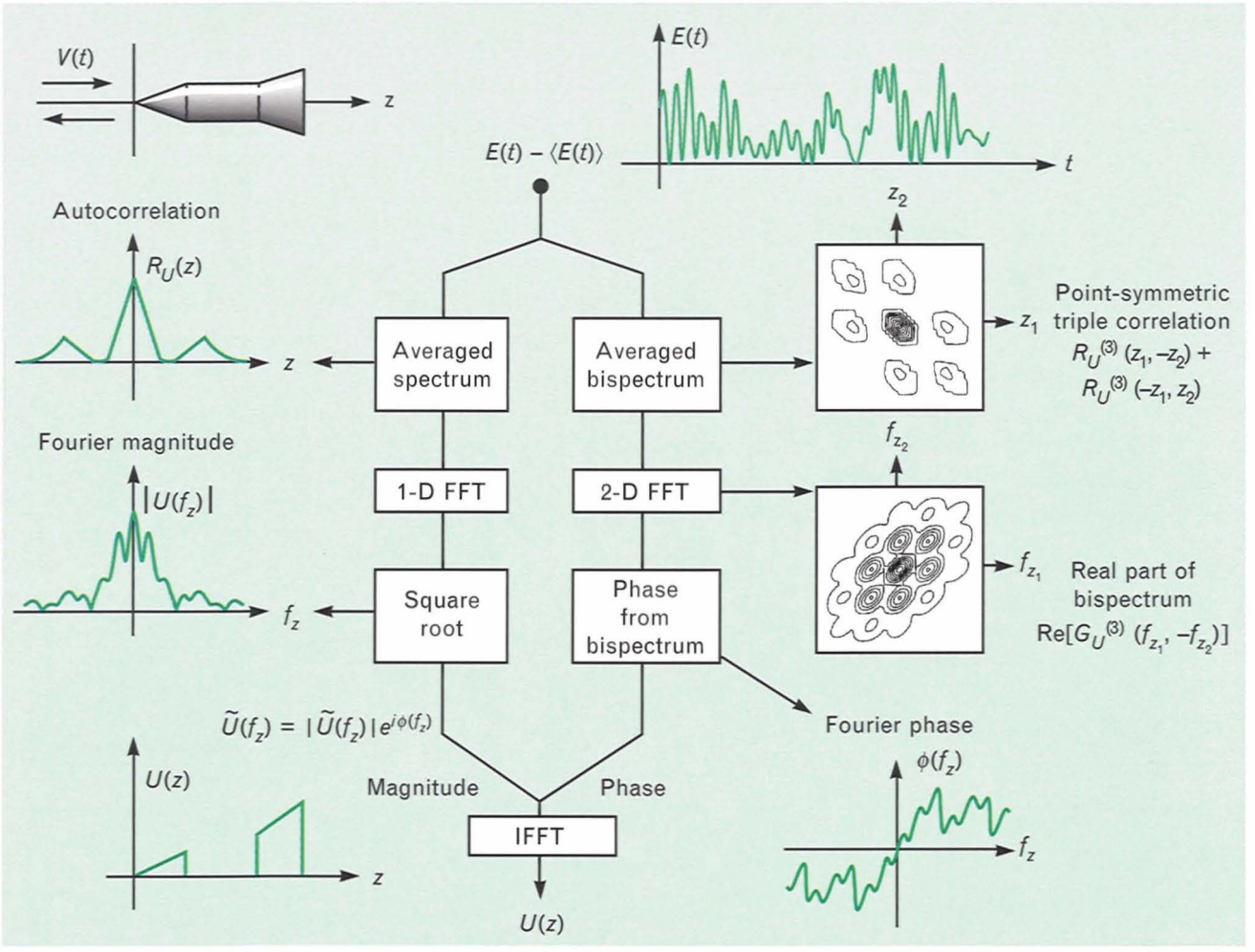

FIGURE 24. Block diagram for recovering the range-resolved laser radar cross section from bispectral signal processing of the fluctuating speckle intensity. The Fourier magnitude is recovered in the left branch and the Fourier phase is recovered in the right branch.

a new minimization function:

$$F_2(\psi, \hat{\phi}, b) = \sum_{m,n} \left\{ \mathrm{mod}\, 2\pi \left[|\psi_{m,n}| - |\hat{\phi}_m + \hat{\phi}_n - \hat{\phi}_{m+n}| \right] b_{m,n} \right\}^2 .$$

In Figure 23, we compare reconstructions of $U(z)$ for a triconic based on minimizing F_1 and F_2 to determine $\phi(f_z)$. Although both functions produce good reconstructions, minimizing F_2 tends to introduce high-frequency oscillations at sharp discontinuities in $U(z)$. As illustrated in the figure, these oscillations can be smoothed by filtering (with a slight loss in resolution). Minimization of F_2 greatly reduces the computation time because it allows the sign-retrieval step to be bypassed. Therefore, in our algorithm we have decided to minimize F_2 instead of attempting to recover the sign of the bispectrum phase by using two-dimensional phase retrieval.

The algorithm used for reconstructing $U(z)$ from the intensity data is summarized by the block diagram illustrated in Figure 24. This algorithm is demonstrated on wavelength-decorrelation data in the next section.

Wavelength-Decorrelation Measurements

Up to this point we have concentrated on the theoretical aspects of wavelength decorrelation. We now investigate wavelength decorrelation from an experimental point of view. We begin by describing the

laboratory setup and then we reintroduce the fundamental concepts of wavelength decorrelation through a series of laboratory measurements. At the end of this section, we point out some of the potential applications of the wavelength-decorrelation technique in target discrimination.

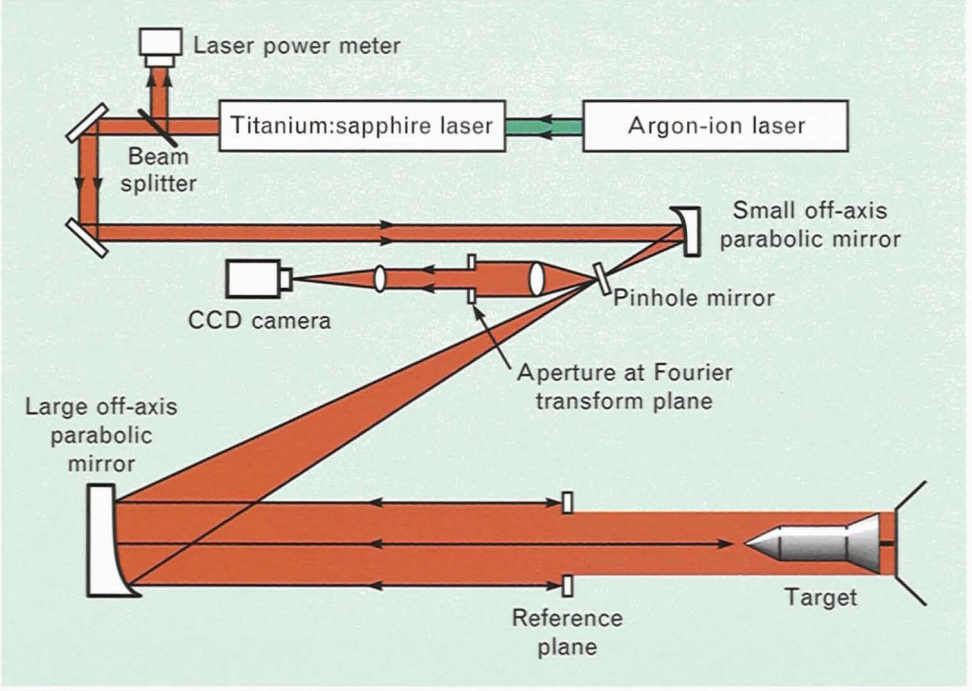

(a)

(b)

FIGURE 25. Laser Speckle Laboratory: (a) schematic of optical system; (b) photograph of laboratory apparatus.

Laboratory Layout

Figure 25 shows a schematic diagram and a photograph of the optical setup. Because our objective was to prove the wavelength-scanning concept, we used off-the-shelf equipment whenever possible. The commercially available tunable laser that best fit our needs was a Coherent, Inc., 899-29 Ti:sapphire ring laser (shown in Figure 26). It is pumped by a Coherent, Inc., Innova 200 argon-ion laser. The Ti:sapphire is an actively stabilized single-frequency ring laser that can produce a coherence length greater than 100 m. This coherence length is more than adequate for this type of measurement because it is large compared to the range extent of targets of interest. Because the wavelength-decorrelation technique can be implemented by using direct detection of the speckle intensity, the total propagation distance to and from the target can be much greater than the coherence length of the laser, which makes this technique attractive for remote-sensing applications.

The Ti:sapphire laser can scan continuously in frequency over a range of approximately 30 GHz, which implies a range resolution of 5 mm. It also operates in a computer-controlled frequency-stepping mode that uses an internal wavemeter for feedback. In this mode, it can be stepped over a much larger range of 10 THz, to yield an extremely high range resolution of 15 μm. But the stepping mode is slow compared to the scanning mode. We chose the stepping mode, however, because we felt that demonstrating submillimeter range resolutions in the initial measurements was more important than having high data-acquisition rates. In the future the optical system will be customized to combine high resolution with high speed.

After the beam exits the Ti:sapphire laser, it is directed into the beam-expanding telescope. A small fraction of the power is diverted into a power meter before entering the telescope to account for any fluctuations in the laser power during a scan. The telescope simulates far-field illumination by flood-illuminating the target with an expanded and collimated laser beam. It consists of a pair of off-axis parabolic mirrors that provide a beam-expansion ratio of 25× and a maximum beam diameter of 22.5 cm.

Once the beam has been expanded and collimated, it strikes a target assembly, such as the one pictured in Figure 27. A Newport Corp. PM500 computer-controlled rotation stage is incorporated into the assembly shown here for precise angular positioning of the target. In the case shown, the target is a 2.5-cm-long triconic coated with retroreflective paint, which is used primarily to provide a strong return signal relative to the scatter from the supporting structure. A vertical shaft attached to the base of the triconic

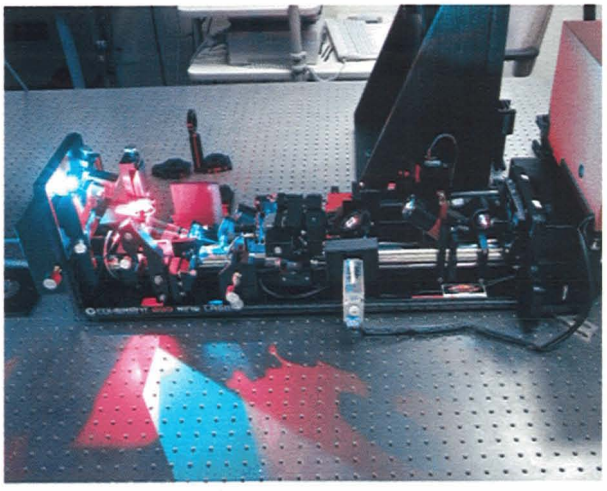

FIGURE 26. Coherent, Inc., Model 899 tunable Ti:sapphire ring laser. This laser is a continuously tunable, solid state source operating at wavelengths between 0.69 μm and 1.1 μm. Its maximum output power is 2.5 W cw, and its actively stabilized single-frequency operation provides for a coherence length greater than 100 m.

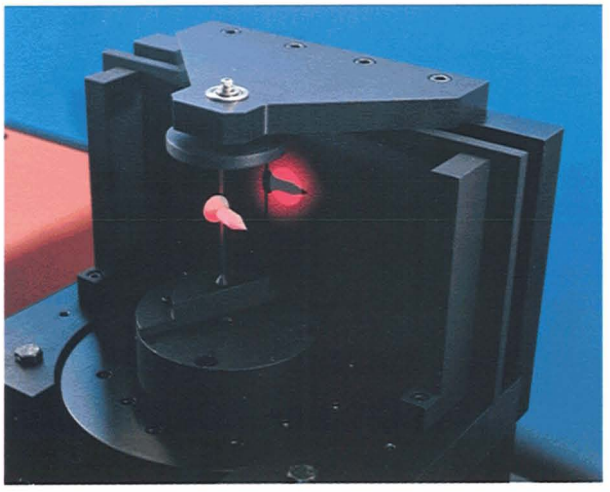

FIGURE 27. Target angular-positioning assembly utilizing a Newport Corp. PM500 Motion Controller for precise angular positioning.

allows it to accommodate a large range of aspect angles. Figure 28 shows several other bare target models. Except for the flat plate, these models are approximately 10 cm in length.

The telescope also serves as the collector for the receiver. Backscattered light from the target is collected by the large off-axis parabolic mirror (as shown in Figure 25[a]) and is reflected toward the pinhole mirror located at the focal point of the telescope. The purpose of the pinhole mirror is to direct the backscattered light into the detector leg of the telescope, while at the same time passing the strong outgoing beam through the pinhole without scattering stray light into the detector. Thus the pinhole mirror serves as a low-scatter, high-efficiency beam splitter for observing the speckle pattern in the neighborhood of the monostatic observation direction. Although the pinhole resembles an optical spatial filter, which is typically used for improving the spatial quality of a laser beam, spatial filtering is not intended here.

Because we are simulating a far-field configuration, the speckle pattern must be observed at the corresponding plane in the optical system. By Equation 1, the complex amplitude of the optical field in the far field is essentially the two-dimensional Fourier transform of the complex amplitude of the optical field at a representative plane near the target, so the appropriate place for observing the speckle intensity is the focal plane, or *Fourier plane*, of the large parabolic mirror. Here parallel incoming rays converge to localized points of light, each having a position corresponding to the direction of propagation of the rays. Only rays that propagate parallel to the telescope axis (which include the outgoing beam and exactly retroreflected light) pass through the pinhole. Only backscattered light traveling in directions near the monostatic observation direction reaches the pinhole mirror.

The detector cannot be placed at the focal point because it would block the outgoing beam. Therefore, the pinhole mirror reflects the light away from the telescope axis so that the speckle pattern can be imaged onto the detector array with lenses, as depicted in Figure 25(a). Besides relaying the speckle pattern at the focal plane to the detector plane, the lenses provide two other benefits. First, they provide for a magnification or demagnification M of the speckle pattern for optimal utilization of the detector array. Second, they make it possible to block out much of the scattered light associated with overfilling the target with the laser beam. This blocking of the scattered light is possible because the two lenses are in a Fourier-transform configuration. Consequently, an image of the target is formed at the Fourier-transform plane located between the two lenses, and light not associated with the target can be masked at this plane.

Figure 29 is a photograph of the CCD camera assembly. A Photometrics Ltd. scientific-grade CCD camera was selected because of its low noise, high

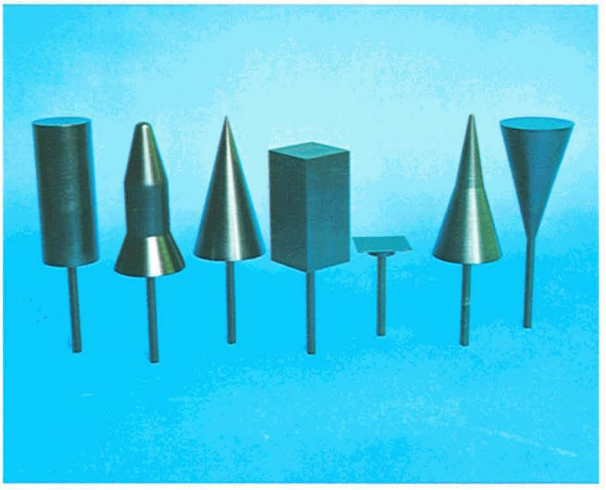

FIGURE 28. A sample of uncoated target models used for investigating speckle discrimination.

FIGURE 29. Photometrics Ltd. 512 × 512 pixel CCD camera Peltier-cooled to –40° C.

linearity, and high dynamic range. The CCD contains 512×512 pixels that are $27\ \mu m \times 27\ \mu m$ in size. The speckle size $d_\perp$ on the CCD array is an important consideration. It must be large compared to the pixel size so that speckle-intensity variations can be resolved. By replacing the distance R in the formula for the speckle size $d_\perp$ with the focal length f of the lens or mirror, we can apply this formula to the situation when the far field is simulated with a lens or a mirror. We must also include an additional factor of M to account for the magnification of the speckle pattern in the relay optics of the detector leg. Therefore, the appropriate expression for the speckle size at the detector plane is $d_\perp = \lambda Mf/D$. In our optical system, the focal length f of the primary mirror is 2 m, and the operating wavelength λ of the laser is approximately 0.75 μm. For a transverse target size of $D = 5$ cm and a magnification of $M = 8$, the average speckle size $d_\perp$ at the detector plane is approximately 240 μm. Thus the speckle lobes are well resolved, and the total number of speckles on the CCD array is greater than 1000 in this situation. Having a large number of speckles to sample from is useful because the wavelength signatures can be smoothed by averaging over many pixels.

The disadvantage of the Photometrics CCD camera is that it requires over one second to read out the entire array. This slow framing rate, along with the slow frequency-stepping rate of the laser, causes a typical 1024-point scan to take approximately one

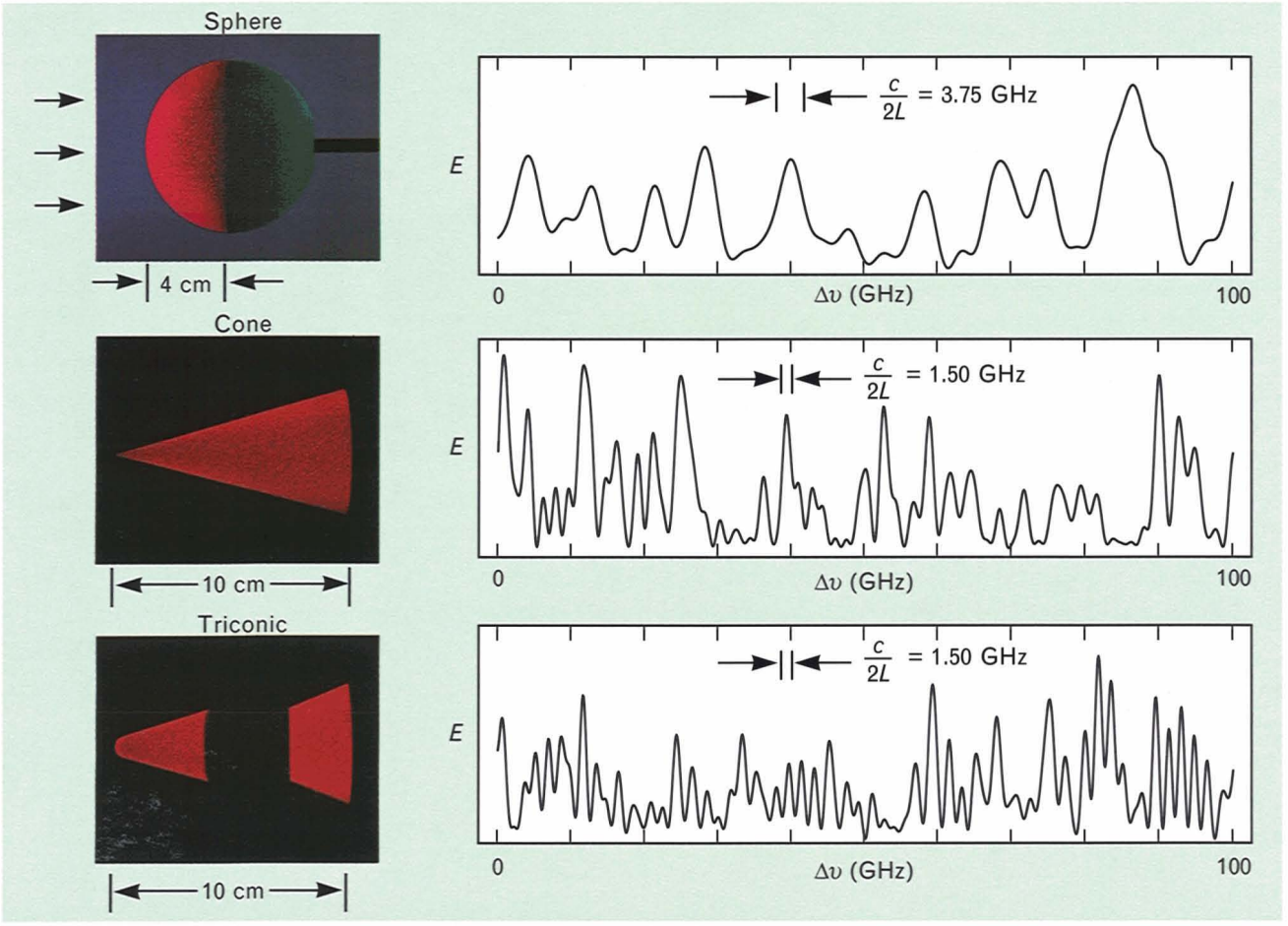

FIGURE 30. Speckle intensity versus laser frequency. These plots illustrate that the statistical properties of the fluctuating speckle intensity are related to the size and the shape of the illuminated object. As the illuminated range extent L increases, the decorrelation frequency $c/(2L)$ decreases. The spectral makeup of the curves depends on the shape of the object.

hour to complete. Any motion of the speckle pattern, arising from mechanical vibrations or air turbulence, during this period will degrade the measurements. For this reason, the entire optical assembly is mounted on a vibration-isolated optical table, and the optical assembly is enclosed within a turbulence shroud. Work is under way to increase the data-acquisition rate, which will greatly reduce the effects of turbulence and vibrations. Currently, data acquisition is inefficient because the 512×512 array is decimated to a 32×32 array to sample each speckle approximately once on average. Little advantage is gained by processing the information from every pixel (as long as the light level is high) because uncorrelated estimates are necessary for averaging.

Demonstration of Fundamental Concepts

The optical setup will now be used to demonstrate the basic relations between the wavelength dependence of speckle and the physical properties of the object being illuminated. In presenting these relations, we take the point of view of a scientist who is given access to the equipment described in the previous section, and who is investigating wavelength decorrelation for the first time.

The natural procedure for investigating wavelength decorrelation experimentally is to illuminate various objects with the tunable laser, observe the effect of varying the laser frequency on the speckle intensity, and look for any differences in behavior that might be linked to physical differences between the objects. We assume that the magnification of the lens in the detector leg is sufficient for producing a spatially well-resolved speckle pattern on the CCD array. Figure 30 illustrates the frequency dependence of the speckle intensity (at a single pixel in the CCD array) for three different objects: a 4-cm-radius sphere, a 10-cm-long cone, and a 10-cm-long triconic. The cone and the triconic are illuminated nose-on. The frequency scan length is 100 GHz, which corresponds to a very small frequency modulation of approximately 0.025% of the carrier frequency.

Observe that the speckle intensity in Figure 30 fluctuates wildly as the laser frequency varies; these scans have high contrast, with nearly complete destructive interference occurring at certain frequencies, and peaks of varying amplitude occurring at others. This type of behavior has already been observed in the spatial structure of the speckle patterns shown in Figure 5, and it is representative of speckle phenomena in general. The term *wavelength decorrelation* originates because the speckle intensity decorrelates as the frequency or wavelength of the laser is changed. The correlation length $\Delta\nu_D$, which is introduced in the box entitled "Wavelength Decorrelation of Speckle," is a measure of the frequency offset at which we can no longer make a reasonable estimate of the new speckle intensity, given the value of the original speckle intensity.

Let us investigate the differences between the three frequency scans. The most obvious distinction is the longer correlation length $\Delta\nu_D$ for the sphere, which has an illuminated range extent L equal to 4 cm, compared with the cone and triconic, which both have an illuminated range extent L equal to 10 cm. These plots indicate an inverse proportionality between range extent and correlation length and experimentally confirm the relation $\Delta\nu_D = c/(2L)$; i.e., the calculated correlation lengths of $\Delta\nu_D = 3.75$ GHz for the sphere and $\Delta\nu_D = 1.5$ GHz for the cone and triconic agree well with the measured intensity scans.

Next we compare the details of the curves for the cone and the triconic. Although both objects have the same correlation length, a higher proportion of the high-frequency component is found in the curve associated with the triconic. This fact suggests using Fourier analysis of the fluctuating intensity sequence to search for a relation between spectral content and object shape.

To illustrate the information obtained through spectral analysis, we used the sharp-tipped triconic shown in Figure 31. The triconic was chosen because it produces an interesting nose-on illumination signature that is also relatively easy to interpret. The lengths L_1, L_2, and L_3 of the three segments, beginning with the nose, are 3.5 cm, 4.0 cm, and 2.5 cm, and the cone half-angles α_{c_1} and α_{c_3} are 20° and 25°, respectively. For this series of measurements, the laser-frequency step size $\Delta\nu_{\text{step}}$ is 500 MHz to satisfy the Nyquist condition for sampling, as described in Equation C in the box on the wavelength decorrelation of speckle. The total scan length B is 500 GHz, which

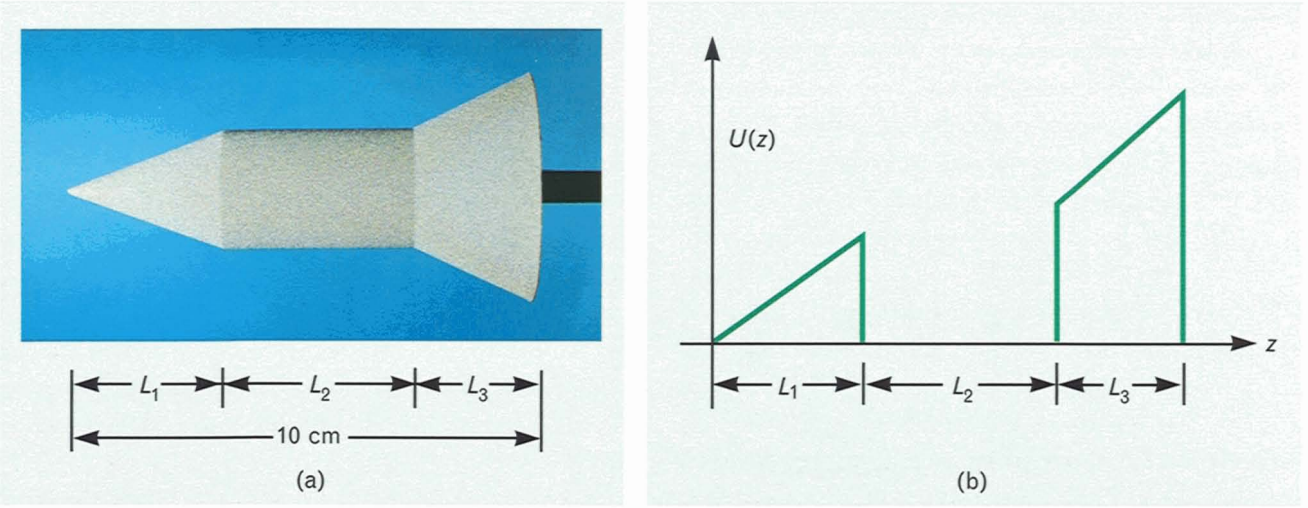

FIGURE 31. Triconic target model and corresponding theoretical range-resolved laser radar cross section for nose-on illumination.

yields a theoretical range resolution of approximately 0.3 mm.

Figure 32(a) is a plot of the estimated spectral density of the fluctuating speckle intensity obtained at a single pixel in the CCD array. Although the curve is highly speckled, several spectral features can be extracted. For example, the spectrum appears to have finite support, or appears to be zero valued outside a certain range of frequencies, indicating that the fluctuating speckle signal is bandlimited. There is also a region, and its mirror image, containing a null in the data. As illustrated in the box on autocorrelation functions, this null is associated with the fact that the lengths L_1 and L_3 of the two conical components of the triconic are both smaller than the length L_2 of the cylindrical component. We can obtain a better estimate of the spectral density by averaging the results from additional pixels. Figures 32(b), (c), and (d) contain plots for averages of 10, 100, and 1024 pixels, respectively. These plots demonstrate that the estimate of the spectral density smoothes out substantially as more averages are performed but that the smoothing effect is nonlinear; i.e., the degree of smoothing is proportional to the square root of the number of speckles sampled. As previously mentioned, calculating the spectral density for every pixel would not improve the estimate of the spectral density significantly because the intensity at neighboring pixels is correlated.

The final estimate of the spectral density shown in Figure 32(d) has an interesting shape that is related to the shape of the object. In investigating the interpretation of this spectral density, we first consider the meaning of the abscissa. Normally, a spectral density is a function of frequency because we take a Fourier transform of a function of time in calculating it. Although the fluctuating speckle signal can be treated as a function of time, the more basic parameter is the laser-frequency offset $\Delta\nu$. If the scan is smooth and continuous, then these two quantities are related through the scan rate γ by $\Delta\nu = \gamma t$. But in our measurements the frequency is stepped, and the time between steps varies from step to step. We therefore treat the signal as a function of laser-frequency offset. Consequently, our spectral density is a function of time because we are now taking a Fourier transform of a function of frequency. Note that the time of 0.67 nsec from the origin to the end of the curve corresponds to the propagation time for light to travel the 20-cm distance from the tip of the cone to the base and back again. This fact indicates that the spectral-density curve contains range information. The range is obtained by multiplying half of the time offset by the speed of light; the factor of one-half accounts for the round-trip path length.

Now that the abscissa has been related to the range z, we next investigate the information content carried by the shape of the curve. Because the strength of the

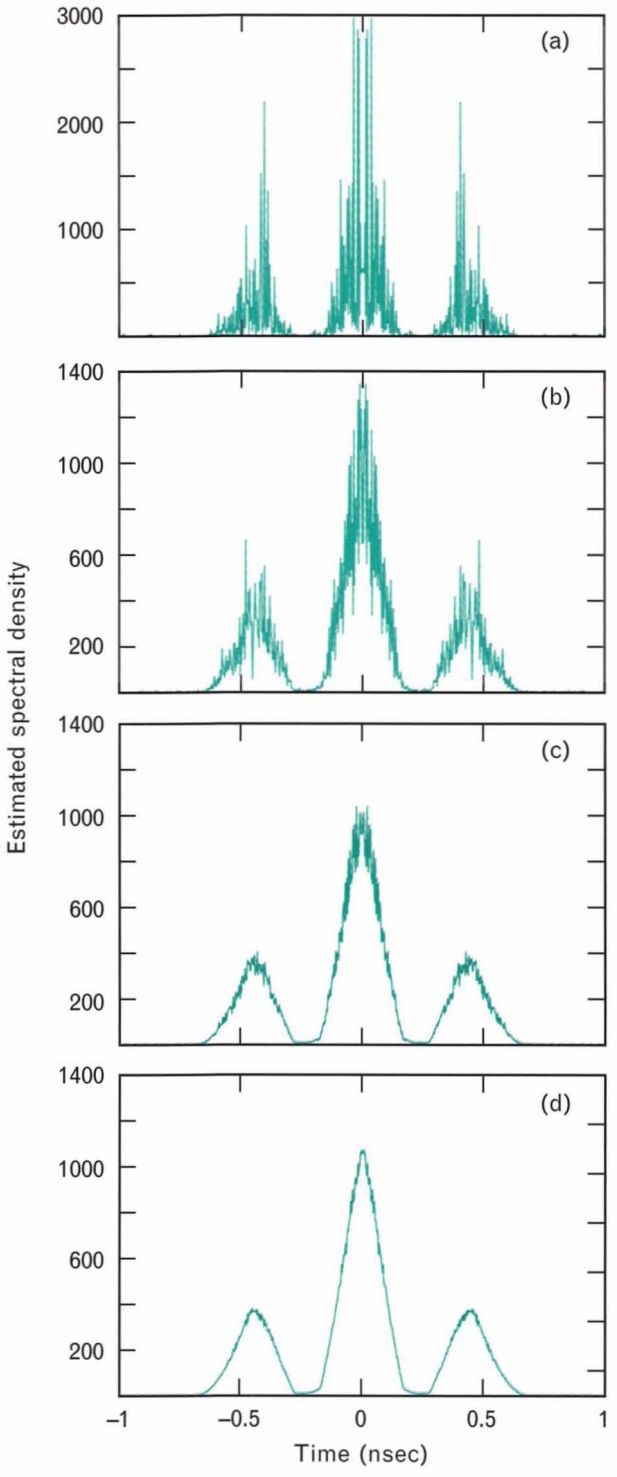

FIGURE 32. Estimated spectral density of the fluctuating speckle intensity produced by illuminating a 10-cm-long triconic target nose-on with a frequency-scanning laser: (a) 1 average; (b) 10 averages; (c) 100 averages; (d) 1024 averages. These curves illustrate the smoothing effect of averaging the individual spectral-density estimates obtained from multiple pixels in the CCD array.

intensity return from a radar is proportional to the target's cross section, and because the spectral-density signature is a function of range z, we expect that this signature contains information about the range-resolved laser radar cross section $U(z)$ of the target. The spectral-density signature is clearly not a direct measurement of $U(z)$, however. We note some properties of the spectral-density curve that help us relate it to the range-resolved laser radar cross section: (1) it has a width equal to twice the range extent of the target, (2) it is an even function, and (3) its highest value occurs at the origin. All of these properties are associated with autocorrelation functions. These observations, in addition to the previous result for the transverse properties of speckle, which involved the autocorrelation function of the brightness distribution function, lead us experimentally to the hypothesis that the ensemble-averaged spectral density is proportional to the autocorrelation function $R_U(z)$ of the range-resolved laser radar cross section $U(z)$.

To test this hypothesis, we need to determine $U(z)$ separately. Figure 31(b) contains a theoretical plot of $U(z)$ for on-axis viewing of a Lambertian triconic with the appropriate dimensions. The null in the middle region occurs because the surface of the cylindrical segment is not illuminated for nose-on viewing. The autocorrelation function of this particular range-resolved laser radar cross section is plotted in Figure A in the box entitled "Autocorrelation Functions." We observe a close similarity between Figure A and the averaged spectral density of Figure 32(d).

To compare these functions more closely, we must know $f(\theta)$ for the triconic at the angles of incidence for the two conical components; i.e., $\theta_1 = 70°$ and $\theta_3 = 65°$. A technique for measuring $f(\theta)$ is illustrated in the box entitled "Angular-Scattering Measurements." Figure A in this box shows the monostatic properties for a retroreflective paint that is similar in behavior to the 3M 7210 retroreflective paint used to coat the triconic. Note that the $f(\theta)$ function curves upward at the edges, and that $f(70°)$ is larger than $f(65°)$ by approximately 50%. Another consideration in comparing experiment with theory is beam uniformity. In this measurement, the illuminating beam was nearly Gaussian, with an intensity drop of approximately 25% at the perimeter of the target. After

ANGULAR-SCATTERING MEASUREMENTS

TO UNDERSTAND and predict laser radar target signatures, we must be able to measure the angular-scattering properties of surface materials. For the monostatic radar configuration considered in this article, we can characterize the surface-scattering properties by the monostatic reflectance distribution function (MRDF) $f(\theta)$. Basically, $f(\theta)$ describes the variation with angle of incidence θ of the strength of the backscattered radiation from a flat-shaped material sample. If the return signal is measured in units of laser radar cross section σ, and if the surface area of the sample is A, then we can write $f(\theta)$ as

$$f(\theta) = \frac{\sigma}{4\pi \cos^2\theta\, A}. \quad \text{(A)}$$

Equation A is obtained by applying Equation 8 to the calculation of σ for a flat plate and solving for $f(\theta)$. The division by $\cos^2\theta$ in Equation A accounts for two separate $\cos\theta$ obliquity factors. One obliquity factor arises from the decrease in target irradiance $E_0\cos\theta$ (measured normal to the surface element) as θ increases. The other obliquity factor accounts for the smaller projected area $A\cos\theta$ of the surface with respect to the receiver at larger values of θ. Equations 9 and 10 show how $f(\theta)$ enters into the calculation of the laser radar cross section σ and the range-resolved laser radar cross section $U(z)$. Equation 7 gives the local angle of incidence θ in terms of the height function $h_{||}(x, y)$ that specifies the target shape.

We describe two methods for measuring $f(\theta)$. In the first method we measure the laser radar cross section σ of a flat-shaped sample of the surface material as a function of the angle of incidence θ and substitute this result into Equation A. In the definition of laser radar cross section, we assume the target is flood illuminated with a uniform beam. Although the optical system shown in Figure 25 was designed to measure a target's monostatic speckle pattern, it is also useful for measuring σ because it provides for flood illumination of the target and detection of the return signal in the monostatic direction. When using this system to measure σ, we fix the laser frequency and measure the integrated intensity at the detector plane, rather than tuning the laser and resolving the individual speckles. We determine σ by comparing the resulting reading with the reading for a calibrated target with known σ.

The first method has two problems that limit its accuracy. First, because the surface sample is flood illuminated, the incident beam also strikes the background and the supporting structure. The resulting unwanted contributions to the return signal affect the accuracy of the measurement. Second, a uniform illumination beam is difficult to produce. This fact results in an uncertainty in the total power incident on the surface sample, which causes inaccuracies in the measurement of σ.

We can overcome both of these difficulties by spot-illuminating the sample material so that the entire beam strikes the target. Let P_i be the total incident power on the surface sample. For spot illumination we need an expression for $f(\theta)$ that is based on knowledge of P_i, rather than on the assumption that the surface is uniformly illuminated with irradiance E_0.

If we specify the strength of the return signal in terms of the radiometric intensity $I = dP/d\Omega$, where dP represents the power collected by a receiver subtending a solid angle of $d\Omega$ with respect to the scatterer, then we can write an expression corresponding to Equation A, but for spot illumination, as

$$f(\theta) = \frac{I}{P_i \cos\theta}. \quad \text{(B)}$$

The $\cos\theta$ obliquity factor in Equation B accounts for the decrease in surface irradiance with increasing angle of incidence θ. Only one obliquity factor occurs in the spot-illumination mode (in con-

trast with the flood-illumination mode, in which there are two obliquity factors) because the projected area of the illumination spot remains constant. The actual illuminated area of the surface sample increases by a factor of $\cos^{-1}\theta$. Consequently, either a large sample or a small beam is required to make measurements at large aspect angles.

One approach to measuring $f(\theta)$ by using the spot-illumination mode is to measure the radiometric intensity I and the incident power P_i separately and substitute them into Equation B. A better approach is to use a surface-material standard. The standard should be diffuse and highly reflective so that it approximates a Lambertian surface. Then its MRDF at normal incidence will be close to the ideal value of $f(0) = 1/\pi$. The system calibration factor is determined by relating the instrument reading for normally incident illumination of the standard to the known MRDF value of the standard. Readings at angles other than normal incidence are divided by $\cos\theta$ in accordance with Equation B.

We illustrate measurements of $f(\theta)$ by using the spot-illumination mode and the optical system depicted in Figure 25. Flat samples of the surface material are placed in an angular positioner at the target location and illuminated by a HeNe laser with $\lambda = 0.633$ μm. Figure A presents the resulting measurements of $f(\theta)$ for Newport HC-560 retroreflective paint, Newport HC-563 white diffuse paint, alodined aluminum, and Krylon 1402 heat-resistant paint. The dashed line represents a theoretical Lambertian surface with $f(\theta) = 1/\pi$. All of the measurements of $f(\theta)$ curve upwards for large values of θ, even though the $\cos\theta$ obliquity factor has been properly accounted for. The white diffuse paint most closely resembles a Lambertian surface. For monostatic purposes the retroreflective paint can be modeled as a Lambertian surface with a gain of approximately 20 dB.

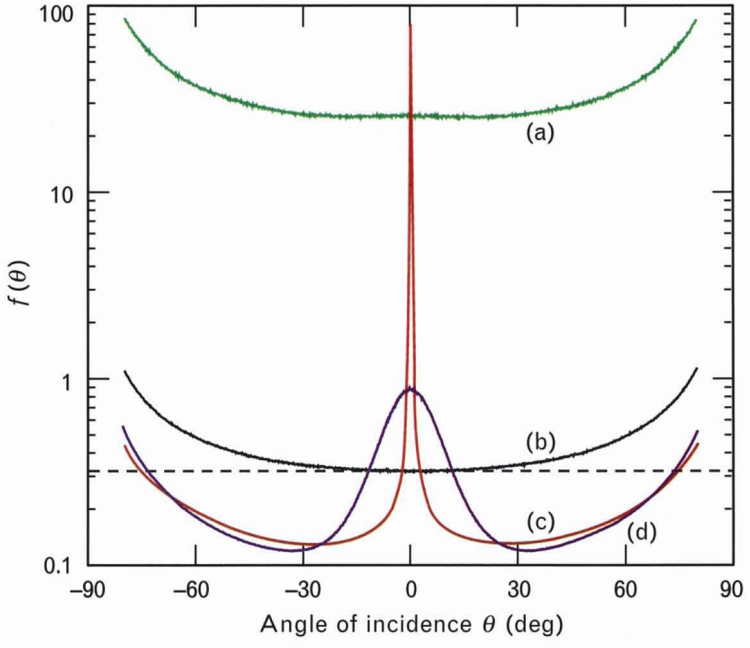

FIGURE A. Measured $f(\theta)$: (a) Newport HC-560 retroreflective paint; (b) Newport HC-563 white diffuse paint; (c) alodined aluminum; (d) Krylon 1402 heat-resistant paint.

accounting for the effect of a nonconstant $f(\theta)$ and the effect of beam nonuniformity on $U(z)$, we calculated the autocorrelation function of $U(z)$ by computer. In Figure 33 we compare this autocorrelation function with the averaged spectral density in Figure 32(d). The excellent agreement between experiment and theory indicates that the phenomenology for wavelength decorrelation is well understood.

Measurements of Range-Resolved Laser Radar Cross Section

We have shown both theoretically and experimentally that the wavelength-decorrelation technique allows us to measure the autocorrelation function $R_U(z)$ of the range-resolved laser radar cross section $U(z)$ of a target. As shown in the plots at the bottom of Figure

20, $R_U(z)$ may be useful by itself for discrimination purposes. We would also, however, like to have the capability of measuring $U(z)$ directly. This capability is desirable because we can more easily relate $U(z)$ to the physical properties of the target. As explained in the section on bispectral analysis, methods that yield measurements of $U(z)$ must provide the Fourier phase $\phi(f_z)$ in addition to the Fourier magnitude $\left|\tilde{U}(f_z)\right|$ of the range-resolved laser radar cross section. We now demonstrate two techniques that have been developed at the Laser Speckle Laboratory for measuring $U(z)$—a range-reference plane technique and bispectral signal processing.

In a laboratory setting, with a controlled target model, the coherent-detection approach can be implemented in a simple manner by using a range-reference plane. Figure 34 shows a typical laboratory setup with a range-reference ring located behind a spherical target. The basic principle underlying the range-reference technique is explained in terms of the autocorrelation-function result and coherent detection in the box entitled "Range-Reference Planes."

Figures 35 and 36 show experimental results obtained by using the range-reference-plane technique to measure $U(z)$ for off-axis illumination of a cone and a cylinder, respectively. The laser-frequency step size is 1 GHz, and the total scan length is approximately 1 THz. This scan length results in a theoretical range resolution of 0.15 mm. Theoretical predictions of $U(z)$ are shown for comparison; good agreement was achieved in the overall shape of these curves. The high-frequency oscillations in the data are the result of approximating an ensemble average with a finite number of averages, as well as with granularity in the retroreflective surface coating.

A disadvantage of the range-reference plane technique is that the number of effective averages is less than what one might initially expect. This reduced number occurs because the surface of the reference plane must be rough on a wavelength scale. If the surface of the reference plane were optically smooth, then it would produce a single bright spot at the detector plane (because of the Fourier-transform relation between the two planes), and the mixing between the reference signal and the target signal would be limited to a small region of the detector array. Although using a rough-surfaced reference plane does cause the reference signal to spread over the entire

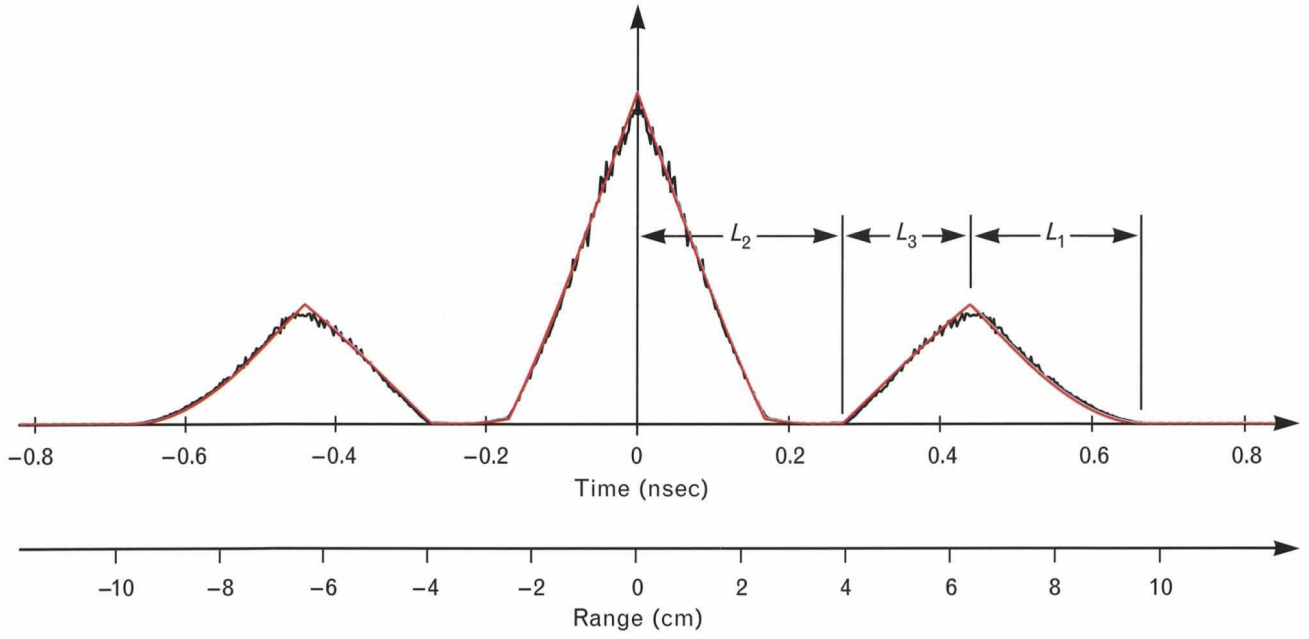

FIGURE 33. Comparison of the averaged spectral density displayed in Figure 32(d) with the autocorrelation function of the theoretical range-resolved laser radar cross section. Radial falloff in the intensity of the illuminating beam and non-Lambertian scattering from the surface of the triconic are accounted for in the theoretical curve.

FIGURE 34. A spherical target mounted in front of a range-reference ring. This type of setup provides a simple means for direct measurement of the range-resolved laser radar cross section.

detector array, it also results in a speckled reference signal. Furthermore, because the reference plane has a small range extent when illuminated at normal incidence, the speckle-intensity pattern from the reference plane remains fairly constant over the entire frequency scan. We know that the intensity distribution of a Gaussian speckle pattern obeys a decaying-exponential probability law [33]. Therefore, a large fraction of the area of the speckle pattern is dark, but there are also regions with intensity levels that are many times the mean. Consequently, the reference signal is weak over a large portion of the detector array. The strong reference signal from the bright regions will tend to dominate and reduce the effective number of speckle averages, resulting in higher fluctuations in the estimate of $U(z)$ than would be otherwise expected.

The reference-plane technique can be modified so that the number of effective averages is not reduced. Ideally, the range-reference plane would be replaced by a single range-reference point; then there would be

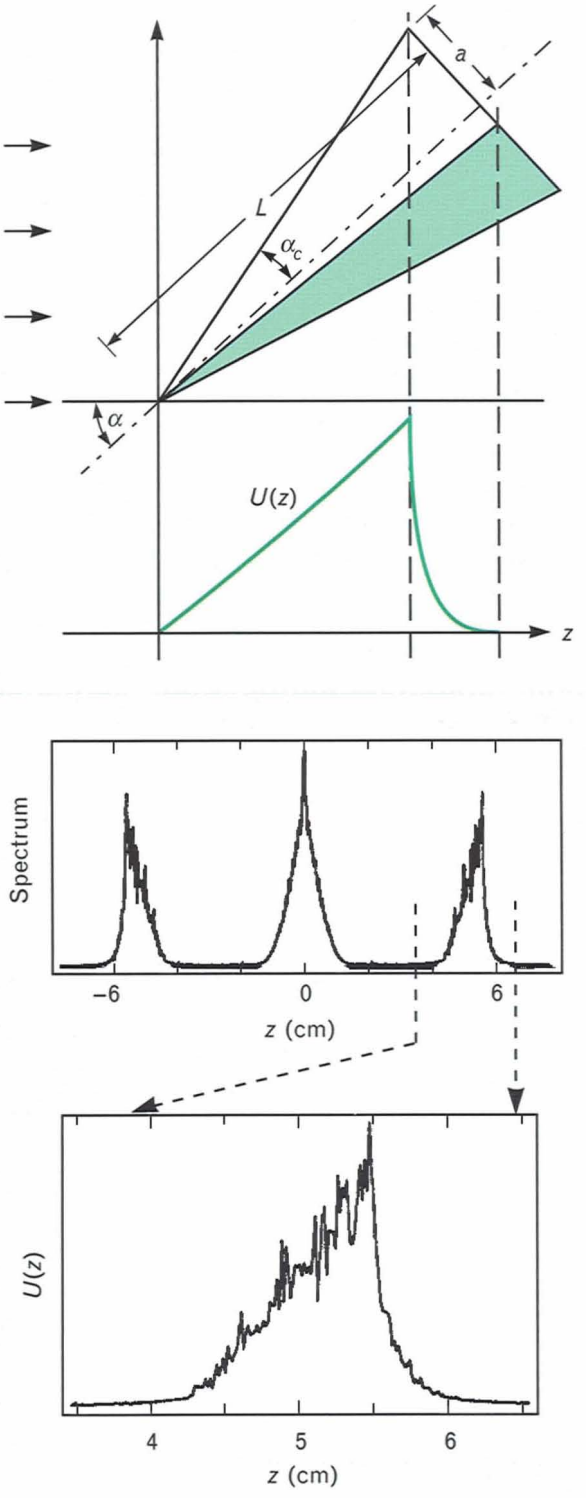

FIGURE 35. Experimental and theoretical range-resolved laser radar cross section for off-axis illumination of a cone at 45°. The cone has a length of 2.5 cm and a cone half-angle of 15°.

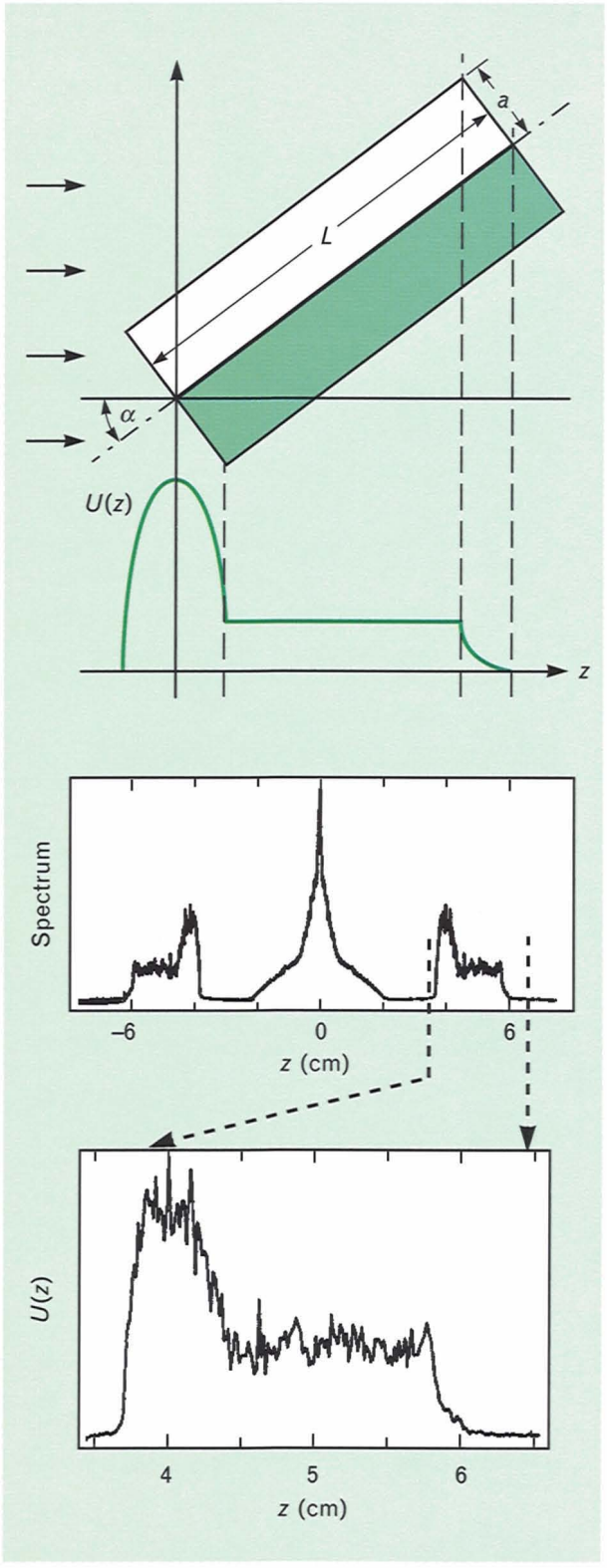

FIGURE 36. Experimental and theoretical range-resolved laser radar cross section for off-axis illumination of a cylinder at 35°. The cylinder has a length of 2.5 cm and a diameter of 1 cm.

no speckle and no degradation in the averaging. Of course, the problem with using a single range-reference point is that it has zero laser radar cross section. Specular points from curved polished surfaces do have large cross sections, however, and we have begun to implement the range-reference technique by using specular range-reference points.

As pointed out in the box entitled "Range-Reference Planes," the reference-plane technique is similar to the coherent-detection technique. The difference is that when using coherent detection we create a virtual range-reference point near the target by separating the paths of the reference beam and the signal beam. The reference beam is obtained by splitting the laser beam before it is expanded and then running the unexpanded beam through a delay path of the appropriate length. Near the detector array the reference beam is expanded and collimated for uniform illumination of the array. Because the reference beam is self-contained, this method could be used in a remote-sensing application, where we do not have physical access to the target. This method is only appropriate, however, when the distance to the target is relatively small; the method becomes increasingly difficult to implement as the propagation distance increases. Another complication is that for a target with a radial velocity component, we may have to adjust the delay length as a function of time to compensate for this motion.

If the frequency scan could be made to be highly repeatable, or coherent, from scan to scan, then a second laser-frequency scan could serve as the reference beam. This approach appears to be impractical, however, for the extremely long scan lengths required for high range-resolution measurements. Because of these difficulties associated with the coherent-detection implementation of wavelength decorrelation, we began to pursue and develop less restrictive direct-detection-based methods. Because direct-detection methods do not require that an accurate delayed copy of the transmitted signal be mixed with the return signal, the hardware requirements are greatly reduced and the resulting system is more robust.

Before illustrating the bispectral signal processing technique for measuring $U(z)$, we demonstrate the extremely high range resolution that we have achieved

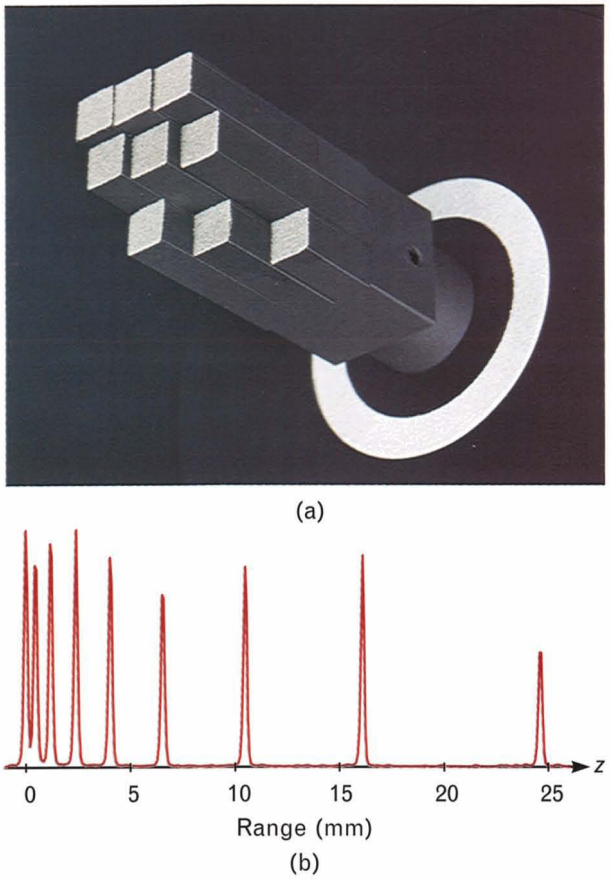

FIGURE 37. Demonstration of submillimeter range resolution: (a) nine-step range-resolution target mounted in front of a range-reference ring; (b) experimentally measured range-resolved laser radar cross section. The step size increases by a factor of 1.4 between steps, beginning with a smallest step size of 0.5 mm.

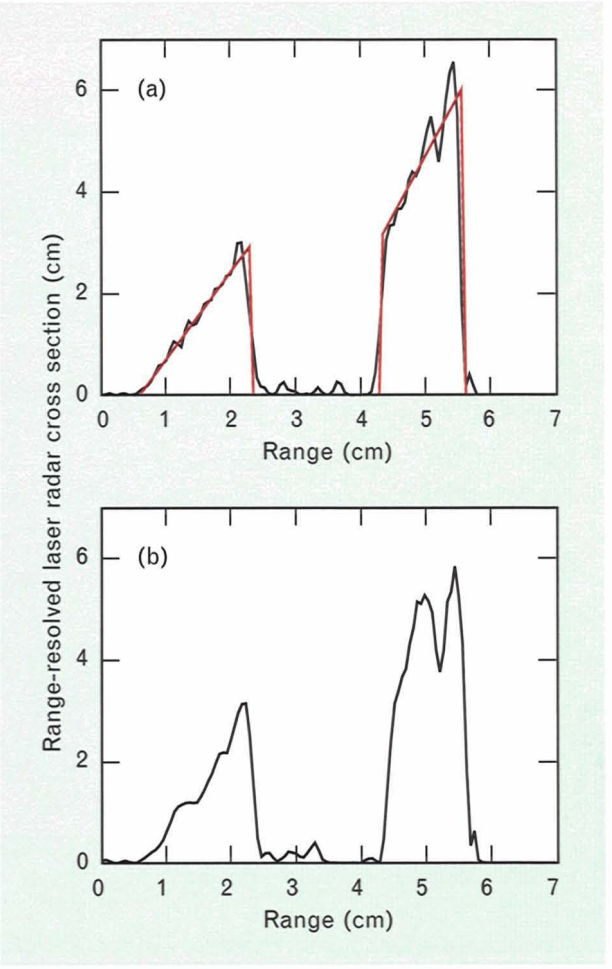

FIGURE 38. Reconstructions of the range-resolved laser radar cross section of a triconic target by using bispectral analysis of the speckle intensity: (a) simulated data; (b) measured data. The red line in part *a* represents the theoretical curve.

by using the range-reference-plane implementation of wavelength decorrelation. For testing range resolution, we constructed a step target with a number of flat surfaces separated by various distances, as shown in Figure 37(a). This target has nine levels, with a ratio of 1.4 between successive step heights. The individual steps range in value between 0.5 mm and 8.5 mm with a total range span of 24.6 mm. Figure 37(b) shows experimental results for a scan length of 2 THz. The associated theoretical range resolution is 0.075 mm. All nine levels in the target are accounted for in the $U(z)$ curve, and even the 0.5-mm step is well resolved, which clearly demonstrates submillimeter range resolution.

As described in the section on bispectral analysis, information about the Fourier phase $\phi(f_z)$ is actually carried by the fluctuating intensity signal, but this information is lost when the magnitude-squared of the Fourier transform is taken when calculating the spectral density. The bispectral signal processing method, however, retains this phase information. We present reconstruction results in Figure 38 for a 5-cm-long triconic target. The estimates of $U(z)$ (including postprocessing using one-dimensional phase retrieval) are indicated for both simulated and experimental data. These plots show good agreement with each other and with the theoretical plot of the range-resolved laser radar cross section for this particular object. A step-by-step reconstruction for this triconic target is presented in Reference 19.

Applications to Discrimination

Because the functional form of the range-resolved laser radar cross section $U(z)$ is directly related to the size, shape, and surface-scattering properties of the illuminated target, and because $U(z)$ can be measured to extremely high resolutions, the wavelength-decorrelation technique offers us important information about the details of the target that can be used for discrimination purposes. We now discuss some ways of extracting target information from wavelength-decorrelation signatures.

In the section entitled "Laser Radar Cross Section and Range-Resolved Laser Radar Cross Section," we showed that basic geometrical shapes (such as the sphere, the disk, the cone, and the cylinder) have distinctive signatures. These signatures might be used as a means of identifying targets by their shape, or determining the component shapes making up a target. For example, we could distinguish between the conical target in Figure 35 and the cylindrical target in Figure 36 from their measured range-resolved laser radar cross sections. In general, a cone and a cylinder can be identified by the sloped straight line and the flat straight line, respectively, in their $U(z)$ signatures.

Let us look more closely at how the theoretical $U(z)$ curves in Figure 35 and Figure 36 are related to the shape of the target. In Figure 35, the discontinuity in the slope of the $U(z)$ curve occurs at the range value z where the range plane no longer intersects a complete cone. As z increases past this point, the curve decreases rapidly at first and then falls off gradually to zero at the value of z corresponding to the last illuminated region of the cone. Similar statements apply to the cylinder in Figure 36. Observe that the disk-shaped end cap on the cylinder produces a large, elliptically shaped hump in the $U(z)$ curve. The end points of this hump clearly mark the boundaries of the disk in range. As a general result, discontinuities in the slope of the $U(z)$ curve, or discontinuities in the $U(z)$ curve itself, are related to physical points or regions on the surface of a target. We can use the position of these discontinuities in range to extract information about target dimensions. Thus much can

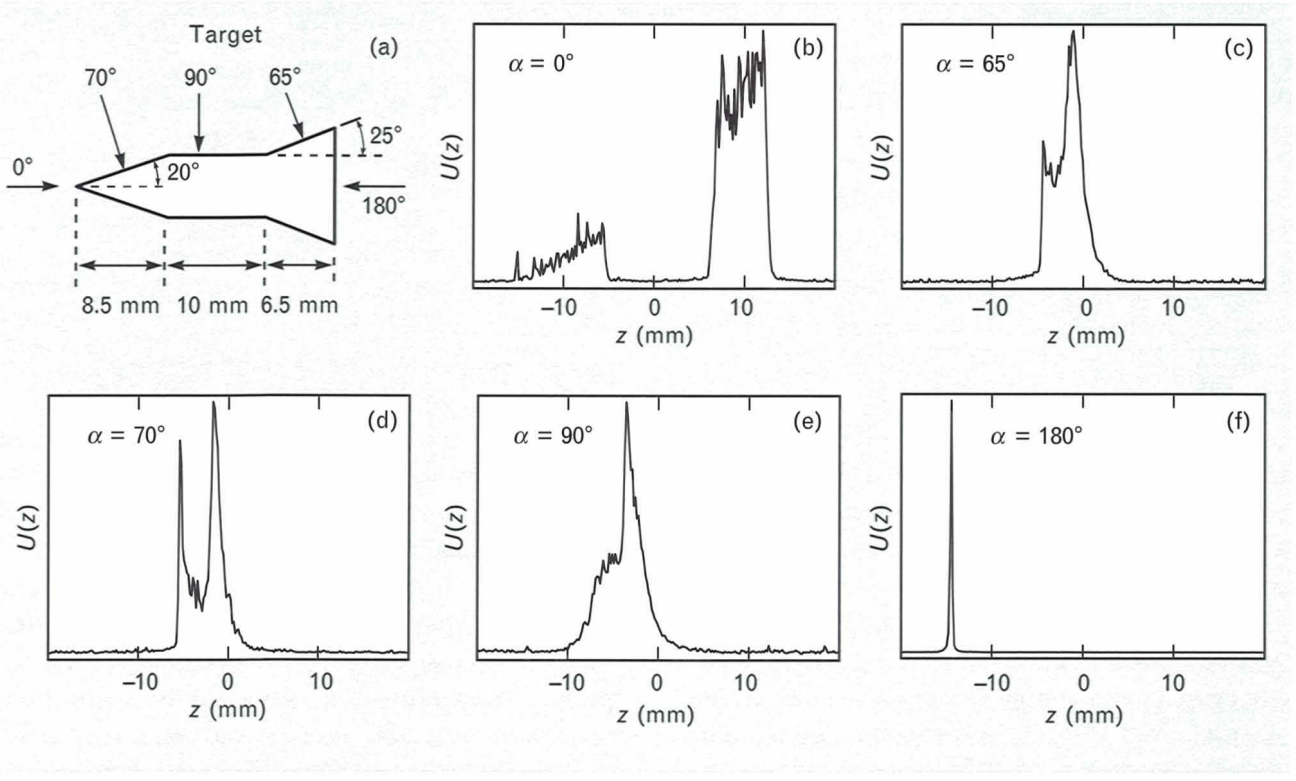

FIGURE 39. Range-resolved laser radar cross section of a triconic target illuminated at various aspect angles α: (a) target dimensions; (b) $\alpha = 0°$; (c) $\alpha = 65°$; (d) $\alpha = 70°$; (e) $\alpha = 90°$; (f) $\alpha = 180°$.

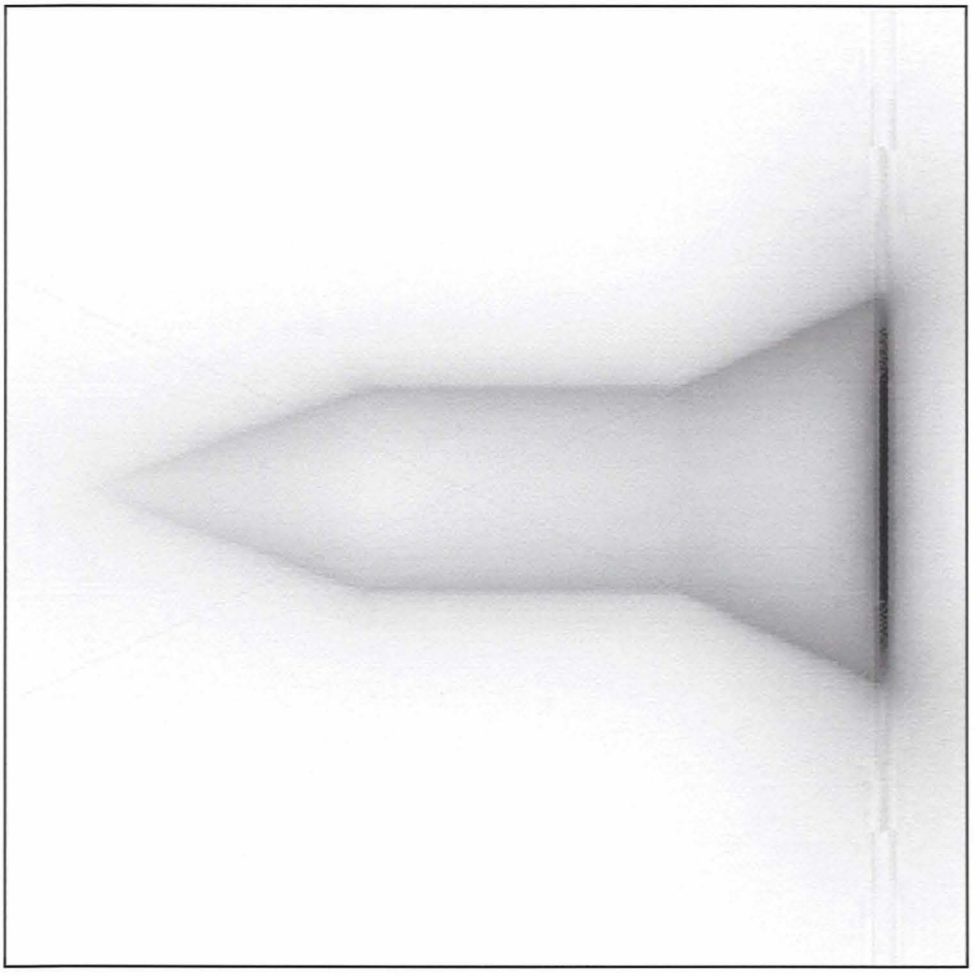

FIGURE 40. Tomographic reconstruction of a triconic from theoretical range-resolved laser radar cross sections for aspect angles ranging between 0° and 180° in 1° increments.

be learned about a target from the functional form of its range-resolved laser radar cross section measured at a single aspect angle.

In many instances, the aspect angle of the target changes as a function of time. As the number of aspect angles increases, we can determine the shape and dimensions of the target with more certainty and characterize more and more complicated targets. Figure 39 shows a set of measurements of $U(z)$ for a 2.5-cm-long triconic target model illuminated at angles of 0°, 65°, 70°, 90°, and 180°. These particular angles were chosen because they correspond to on-axis illumination of the triconic and to broadside illumination of each of the segments of the triconic. The abrupt jumps in $U(z)$ correspond to the reflections from the perpendicular surface components. Because we can relate features of a range-resolved laser radar cross-section signature to physical properties of the target, these features might serve as a basis for automatic-target-recognition algorithms.

When a wide range of aspect angles is available, a three-dimensional image of the target can be reconstructed by using reflective tomography [14, 46–50]. Tomography is a method for reconstructing the shape of an object from a series of projections of that object taken from many different angles. The range-resolved laser radar cross section can be considered such a projection. Figure 40 presents a reconstruction from theoretical $U(z)$ data for a triconic target at 1° increments in aspect angle. Cross shadowing between the three components of the triconic is not accounted for in the calculation of $U(z)$.

In addition to size and shape information, the wavelength-scanning technique yields valuable information about surface coatings [51]. We first consider the case in which the shape is known to be spherical. We used the setup shown in Figure 34 to measure $U(z)$ for a 5-cm-diameter sphere. In Figure 41 we compare the results obtained for two different surface coatings, namely, Krylon 1402 heat-resistant paint and 3M 7210 retroreflective paint. The theoretical $U(z)$ curve for a Lambertian surface is shown for comparison. There is a marked difference in the measured $U(z)$ of the sphere for the two coatings. First, $U(z)$ for the retroreflective paint is larger than $U(z)$ for the heat-resistant paint by approximately 20 dB. Second, there is a difference in the shape of these two curves. In particular, $U(z)$ for the heat-resistant paint rises sharply for values of z near the pole, where the angle of incidence θ is small, which indicates that $f(\theta)$ is larger for small angles of incidence. This result agrees with the independent measurement of $f(\theta)$ presented in the box entitled "Angular-Scattering Measurements." This illustration confirms that the wavelength-decorrelation technique can provide useful information about surface materials.

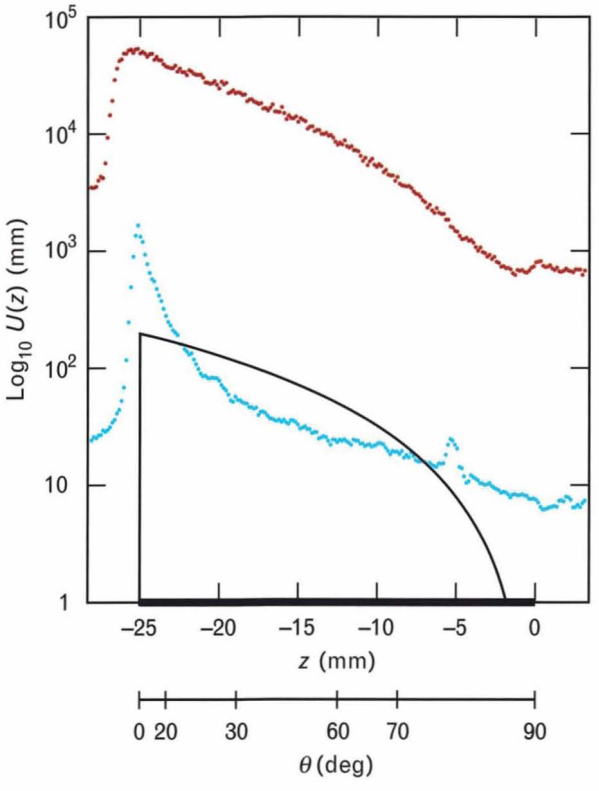

FIGURE 41. Measured range-resolved laser radar cross section of a sphere for two different surface materials: Krylon 1402 heat-resistant paint (blue curve); 3M 7210 retroreflective paint (red curve). The black curve represents the theoretical result for a Lambertian surface. Each value of range z on the sphere corresponds to a unique value of the angle of incidence θ, which allows $f(\theta)$ to be measured.

For the sphere, it is particularly easy to extract the surface-scattering information because each value of the range z maps into a single value of the angle of incidence θ. This fact allows us to invert Equation 15 for the range-resolved laser radar cross section of a sphere and to write $f(\theta)$ explicitly as a function of $U(z)$:

$$f(\theta) = \frac{a}{8\pi^2 z^2} U(z)\Big|_{z=-a\cos\theta} .$$

The above reasoning can also be applied to any axially symmetric object that is illuminated along the axis of symmetry. The range-resolved laser radar cross section then takes the general form given in Equation 13, which can be solved for $f(\theta)$.

In the above situations, on-axis illumination of an axially symmetric target made it possible to determine $f(\theta)$ from a single measurement of $U(z)$. We do not need to have an axially symmetric target, however, to obtain useful information about $f(\theta)$. As a general rule, the target shape determines the position in range of the discontinuities in the $U(z)$ curve, and differences in the angular-scattering properties from target to target produce slower variations and differences in the magnitude of the $U(z)$ curve. Therefore, if two targets are known to have the same shape, then variations in $U(z)$ between these two targets can be related to differences in their surface-scattering properties. Also, if the shape is known, surface properties can be estimated by determining the dominant angles of incidence contributing to a given value of range.

We have stated that the three-dimensional shape of a target can be reconstructed by using reflective tomography, provided that a sufficient range of look angles is available. Reflective tomography, however, also yields information about the surface-scattering properties of the target. When we apply reflective tomography to range-resolved laser radar cross-sec-

tion data, we obtain a three-dimensional object function representing the target reconstruction. Theoretically, this object function is zero-valued for coordinates lying outside the reconstruction. Its values inside the reconstruction are related to the target's surface-scattering properties. We know that the object function tends to fill in for diffuse surfaces and that boundaries are enhanced as the scattering becomes more specular. As an example of a situation that can be treated analytically, the object function for a Lambertian sphere increases linearly from a value of zero at the center to a maximum value at the radius of the sphere [14]. Although much work remains to be done in the interpretation of object functions, reflective tomography does appear to offer the potential for characterizing an object both by its shape and by its surface-scattering properties.

We have discussed some potential uses of the range-resolved laser radar cross section as a discriminant. As illustrated at the bottom of Figure 20, however, significant variation also occurs in the autocorrelation function of the range-resolved laser radar cross section. Therefore, the autocorrelation function might also serve as a discriminant in some applications. An autocorrelation-based system would be the simplest to implement because the additional steps necessary for recovering the Fourier phase would not be carried out.

Another possible approach to discrimination is to develop automatic-target-recognition computer algorithms that are based on features in bispectrum space. The advantage of this approach is that it utilizes the direct-detection signal without losing the Fourier phase information carried by the intensity signal (as is the case for the more elementary spectral-density method), but it does not require the additional steps associated with recovering the Fourier phase $\phi(f_z)$ from the bispectrum.

Finally, to get a more complete description of a target and to maximize the effectiveness of speckle-based discrimination, we could combine the range information obtainable from wavelength decorrelation with the cross-range information available through imaging correlography and the angular dynamics information available through speckle tracking. For example, the speckle-tracking technique can help with the interpretation of wavelength-decorrelation signatures by providing information about the aspect angle α of the target. Additional target information could be obtained by using a bistatic radar configuration and analyzing the wavelength dependence of speckle at more than one receiver location. In the future, other detection schemes, such as wavefront sensing [52, 53], should be considered for the purpose of obtaining the phase information necessary to reconstruct the range-resolved laser radar cross section.

Because of the slow data-acquisition rate associated with our current laboratory system, the wavelength-decorrelation measurements have been limited to stationary targets. Much faster scans are necessary for rotating or translating targets. For us to apply the wavelength-decorrelation technique to moving targets, fast scanning lasers and associated detector arrays must be developed.

Applications of wavelength decorrelation are not limited to target discrimination. Wavelength decorrelation is especially well suited to applications in machine vision, robotics, and metrology, in which the object being probed is located in the vicinity of the laser and noncontacting high-resolution three-dimensional imaging is desired.

Speckle Tracking

In the speckle-tracking technique, we extract information about the angular dynamics of the illuminated target from the motion of the speckle pattern at the receiver. In this section we explain how the motion of the speckle pattern relates to the motion of the target, and then we describe three laboratory techniques for measuring this motion—*spatial cross correlation*, *speckle streaking*, and *temporal cross correlation*. At the end of this section, we give an example of an application of speckle tracking to the determination of the angular dynamics of a spinning and precessing target.

Speckle tracking is based on the fact that the speckle pattern of a rotating object rotates around the object's instantaneous spin axis. Thus the motion of the speckle pattern describes an arc. For the small solid angle subtended by a distant receiver, this arc-like motion appears as a translation of the speckle pattern, except, of course, at positions near the axis of rotation. The

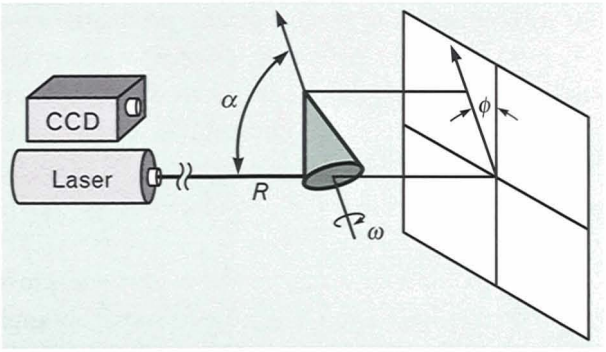

FIGURE 42. Monostatic laser radar configuration for observing speckle motion from a spinning target. The speckle at the receiver plane moves in the direction perpendicular to the projected spin axis ϕ.

direction of speckle motion at the receiver is perpendicular to the projected spin axis ϕ of the object. We can extract information about the angular dynamics of a target by observing the variations in the direction of the projected spin axis with time.

In addition to the direction of speckle motion at the receiver, we can also extract information about the angular motion of a target from variations in the speed of the speckle motion. In a typical application of speckle tracking, the transmitter and the receiver are located in close proximity to each other. Therefore, we assume the monostatic configuration illustrated in Figure 42. For this configuration, the speed v of the speckle motion is related to the object's angular velocity ω, the radar aspect angle α_s with respect to the instantaneous spin axis, and the distance R to the object by the relation

$$v = 2\omega R \sin \alpha_s . \tag{85}$$

Equation 85 indicates that the speckle speed v is proportional to the object's angular velocity ω and the distance R to the object, and that it has its maximum value in the equatorial plane. The speckle speed falls to zero at points lying on the spin axis. As an example of how variations in the speckle speed provide information about angular target dynamics, if ω and R are constant, then we can relate these variations to changes in the aspect angle α_s.

Let us consider the speckle motion in more detail. The angular velocity of speckle motion is obtained by dividing the speckle speed in Equation 85 by the distance R. Note that in the equatorial plane, the angular velocity of the speckle is twice the angular velocity of the object. The factor of 2 can be explained by thinking of the rotating object as a mirror. If a mirror is illuminated normal to its surface and then rotated by a small angle, the back-reflected light

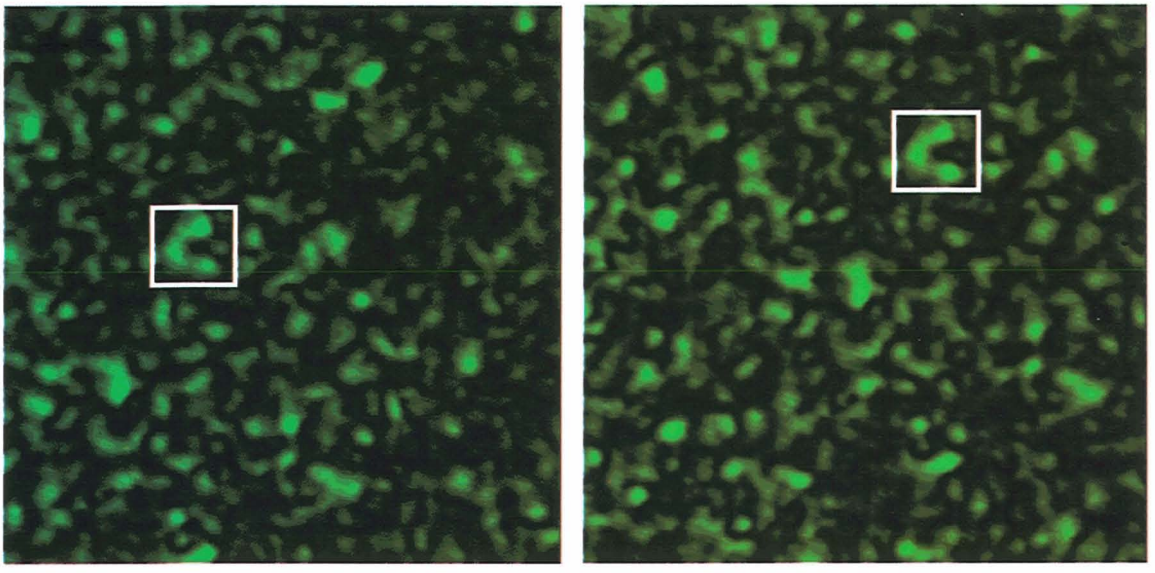

(a) (b)

FIGURE 43. Two successive CCD frames illustrating speckle motion from a spinning target. The boxes indicate the shift in the speckle pattern between frames.

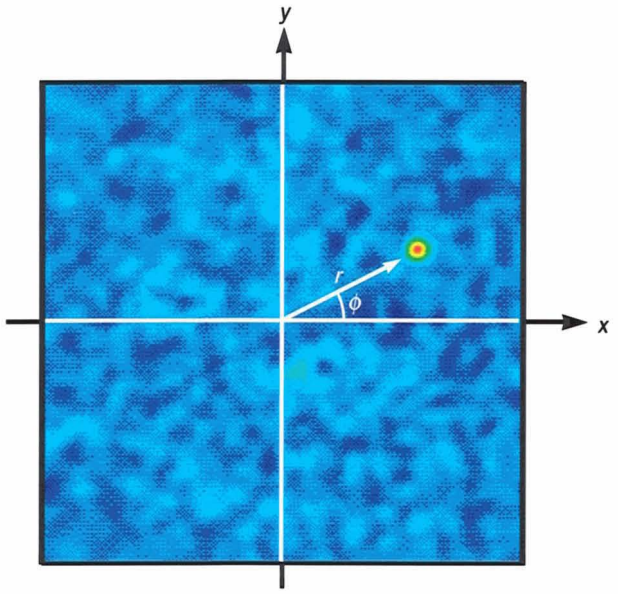

FIGURE 44. Central region of the cross correlation of the two speckle frames shown in Figure 43. The bright spot indicates the distance and the direction of speckle motion.

rotates with respect to the incident beam by twice that angle. Clearly, a speckle pattern cannot rotate at twice the angular velocity of the scattering object and remain constant over a full object revolution. We can see what happens by observing a single bright speckle as the object rotates; as the rotation angle increases, the speckle begins to fade. Thus there is also a decorrelation length associated with how far a speckle moves before it decorrelates. In applications in which the object is large on a wavelength scale, a speckle will move many speckle size units $d_{\perp}$ before decorrelation occurs [7]. Hence we can usually ignore speckle decorrelation caused by target rotation in speckle-tracking applications.

Spatial Cross Correlation

In Figure 43 we illustrate the translational motion of the speckle pattern from a rotating object by showing two CCD frames taken with a small time delay Δt between them. The box placed around the same cluster of speckles in each frame emphasizes the motion of the speckle pattern. To use the information from these two frames in a speckle-tracking application, we need a method for automatically determining the spatial offset between the two speckle patterns. This can be accomplished by calculating the spatial cross correlation of the two speckle frames, as shown in Figure 44. The position of the peak corresponds to the direction and the magnitude of the offset between the two patterns. The brightness of the peak corresponds to the strength of the correlation between the patterns.

We have experimentally tested the spatial-cross-correlation technique by stepping the rotation angle in small increments. The main limitation on accuracy was that atmospheric turbulence caused the speckle pattern to shift slightly during the one-second time delay between CCD frames. In a real-time system or a space-based application, this turbulence would not be the primary limitation on accuracy. Another limitation of the cross-correlation approach is that it is computer intensive, requiring three two-dimensional fast Fourier transforms (FFT) to be performed for each cross correlation. It also requires the capability of taking two short exposure frames in rapid succession.

Speckle Streaking

If the exposure time of the CCD array is too long to freeze the speckle pattern in time, then a streaked image is formed, as illustrated in the speckle frames in the top row of Figure 45. The magnitude of the two-dimensional Fourier transform of these streaked speckle frames, shown in the bottom row of Figure 45, contains a ridge that is perpendicular to the direction of the streaks. Therefore, this ridge points in the direction of the projected spin axis, and variations of this direction from frame to frame provide us with information about the angular dynamics of a target. Speckle streaking is easier to implement than spatial cross correlation because we need only one speckle frame and one FFT for each measurement. Consequently, speckle streaking does not require two exposures that are carefully timed with respect to each other. It is less sensitive to atmospheric turbulence and it is less demanding computationally.

Let us consider the parameters that affect the quality of a speckle-streaking measurement. There are four main parameters to consider: (1) the average speckle intensity, (2) the streak length, (3) the average speckle size, and (4) the array size. We measure the average speckle intensity in units of electrons (photo-

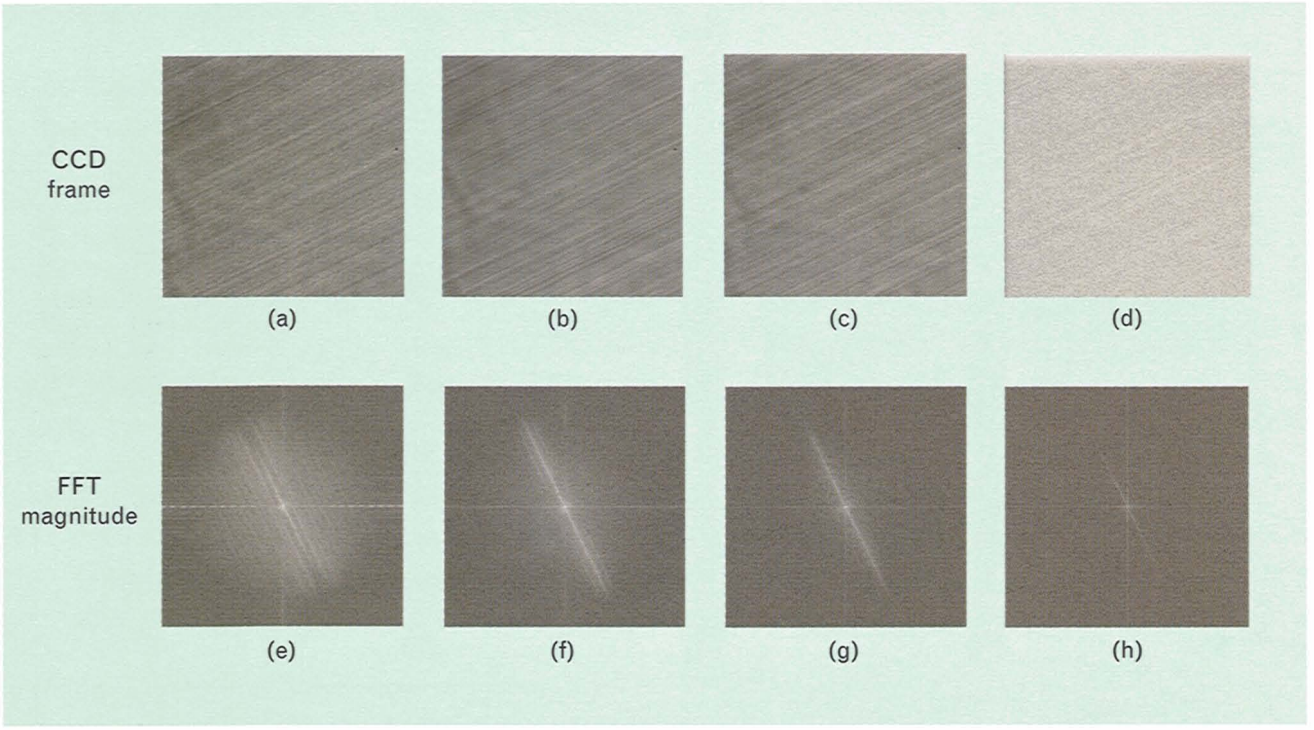

FIGURE 45. Effect of average speckle intensity on the quality of speckle-streaking measurements for a streak length of 100 speckle diameters and an average speckle size of 10 pixels per speckle: (a) streaked frame for 200,000 electrons/pixel; (b) 20,000 electrons/pixel; (c) 2000 electrons/pixel; (d) 200 electrons/pixel; (e) through (h) show the magnitude of the FFT of the streak pattern for parts *a* through *d*, respectively.

electrons) per pixel. This unit takes into account the quantum efficiency η of the detector array, and it is a natural unit of intensity for a CCD array. We measure the streak length in units of the average speckle size $d_{\perp}$ in the direction parallel to the streak, because this quantity is closely associated with the statistics of the speckle streak. The average speckle size is measured in units of pixels per average speckle, and the array size is the number of pixels in the array.

In the top row of Figure 45, we illustrate the effect of changing the average speckle intensity on the appearance of the streaked speckle frames. In this series of measurements the streak length is 100 speckle diameters, the average speckle size is 10 pixels per speckle, and the size of the CCD is 512×512 pixels. The average speckle intensity ranges between a level of approximately 200,000 electrons per pixel (a high level approaching the quantum-well depth of the CCD) to a level of approximately 200 electrons per pixel. The ridge is clearly visible in the Fourier-transform magnitude, shown in the bottom row of Figure 45, even for a mean speckle intensity of 200 electrons per pixel, which is near the noise level of approximately 50 electrons per pixel for our CCD.

We also investigated the effect of varying the other three parameters on the quality of speckle-streaking measurements. We measured the streak direction by using streak lengths ranging between 10 and 10,000 speckle diameters. The speckle contrast (defined as the standard deviation of the intensity divided by the mean of the intensity) is inversely proportional to the square root of the streak length, but even for a streak length of 10,000 there is sufficient contrast for the Fourier transform to provide a good indication of the streak direction. We varied the speckle size between 2 pixels per speckle and 100 pixels per speckle. The smaller speckle sizes provide a better resolution because the available pixels are utilized more efficiently. As expected, the resolution of the angular measurements decreases as the number of pixels in the array decreases. With small speckle sizes, however, useful results can be obtained with arrays as small as 16×16 pixels.

Figure 46 is a block diagram of an algorithm that

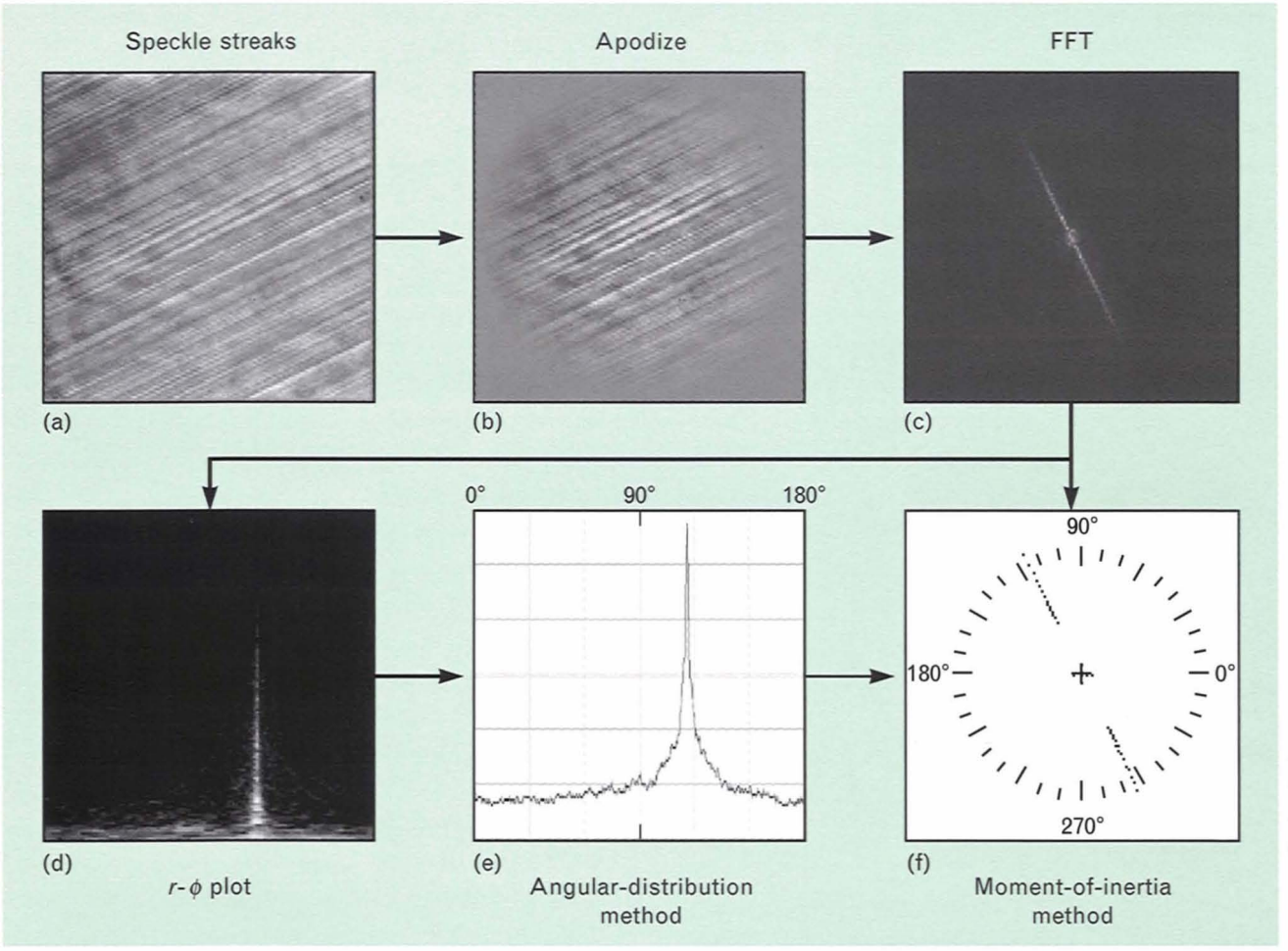

FIGURE 46. Block diagram of the angle-extraction algorithm: (a) streaked speckle frame; (b) radially weighted frame; (c) FFT; (d) representation in radius azimuth-angle space; (e) intensity distribution in azimuth angle; (f) data for moment-of-inertia calculation.

we are developing for automatically computing the streak direction. The input is the streaked speckle frame shown in Figure 46(a). The first step is to eliminate the horizontal and vertical lines that pass through the center of the Fourier transforms shown in the bottom of Figure 45. These artifacts, which arise from the discontinuities at the edges of the input frame, can be eliminated by multiplying the input frame by a radially shaped window function. Figure 46(b) shows the result of this multiplication. The horizontal and vertical lines are no longer present in the magnitude of the Fourier transform displayed in Figure 46(c).

The objective of the algorithm is to obtain as accurate a measurement of the streak direction as possible. To accomplish this objective, we combine two methods. The first method looks for straight lines passing through the origin of the Fourier transform. Essentially, this method divides the image into pie-shaped regions and selects the region with the greatest integrated intensity. To carry out this procedure, we first map the magnitude of the Fourier transform from Cartesian space to radius and azimuth-angle space r-ϕ. The new function, shown in Figure 46(d), is fairly localized in azimuth angle and extends over a large range in the r direction. We improve the signal-to-noise ratio by thresholding or blocking out certain regions of r-ϕ space. For example, low-frequency noise in the streak pattern is eliminated by setting the value of all points below a certain radius to zero. Next, we sum the intensities for each azimuth angle, as illustrated in Figure 46(e). The peak value of the curve

indicates the projected spin direction. For this illustration the angular-distribution method yields an angle of 115.77°. This method is also effective when two or more spinning objects are in the field of view. If their projected spin axes are not equal, then there will be a different peak corresponding to each projected spin axis.

The second method calculates a moment of inertia of the magnitude of the Fourier transform shown in Figure 46(c). Because points farther from the center are weighted more heavily, this method can be biased by noise and irregularities that occur at large radius values. To minimize these effects, we use the results of the first method to select a region over which to calculate the moment of inertia. This region consists of a strip that is centered around the origin and points in the direction of the initial estimate. We use the moment-of-inertia method to try to extend the resolution of the angular-distribution method. The moment-of-inertia method yields a result of 115.81° for the streak shown in Figure 46(a). For this particular data set, the two results differ by only 0.04°. More work is necessary to optimize the angle-extraction algorithm outlined in Figure 46. Currently, we can use speckle streaking to measure the projected spin axis to an accuracy of approximately 0.1°.

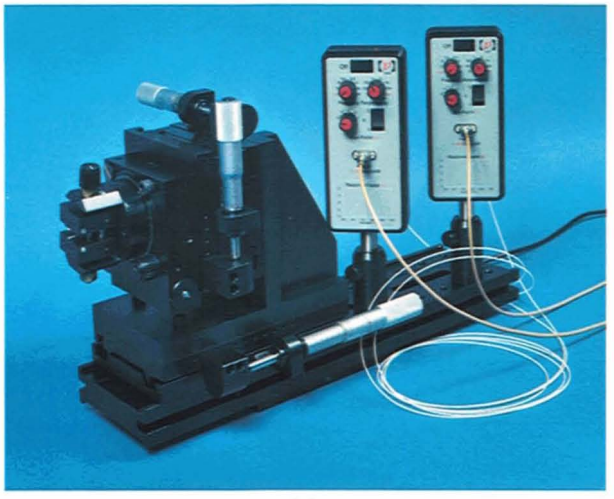

(a)

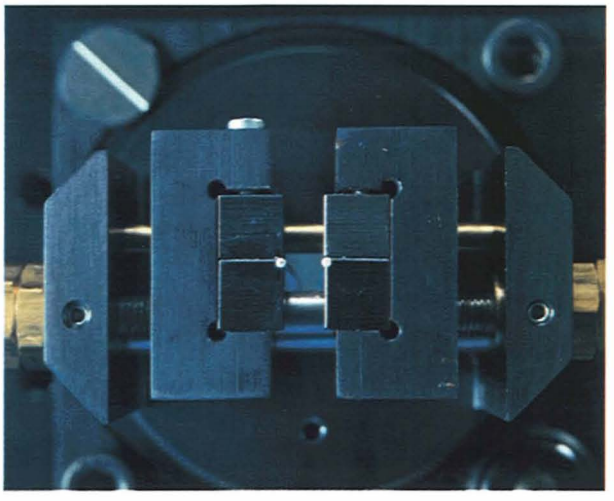

(b)

FIGURE 47. Fiber optic cross correlator for measuring the direction and speed of speckle motion: (a) photograph of the fiber optic cross correlator assembly; (b) close-up of the fiber optic pair.

Although speckle streaking has proven to be a convenient laboratory technique for measuring the projected spin axis, it does have drawbacks. One of these drawbacks is that the sign of the direction of the speckle motion cannot be determined because motion in the reverse direction produces a similar streak pattern. Additionally, it is difficult to measure the speed of the speckle motion with speckle streaking. A limitation of both spatial cross correlation and speckle streaking is that the small physical size of the CCD array does not match with the large speckle size produced in a typical remote-sensing application. To utilize a CCD array we would need to demagnify the speckle pattern, which requires a large imaging aperture. Another possibility would be to construct a large two-dimensional array of detectors. This array would be cumbersome, however, because of the large number of detector elements in the array.

Temporal Cross Correlation

Temporal cross correlation is similar to spatial cross correlation, except that we overcome the need for a many-element detector array by trading off the information obtained from the many-element array at two separate points in time for the information obtained from two or more detectors at many closely spaced points in time. We have implemented temporal cross correlation in the laboratory by using the fiber optic cross correlator shown in Figure 47(a). Figure 47(b) shows two fiber optic cables mounted in the micropositioning assembly. We transmit the light to the detectors by using fibers because they match the speckle

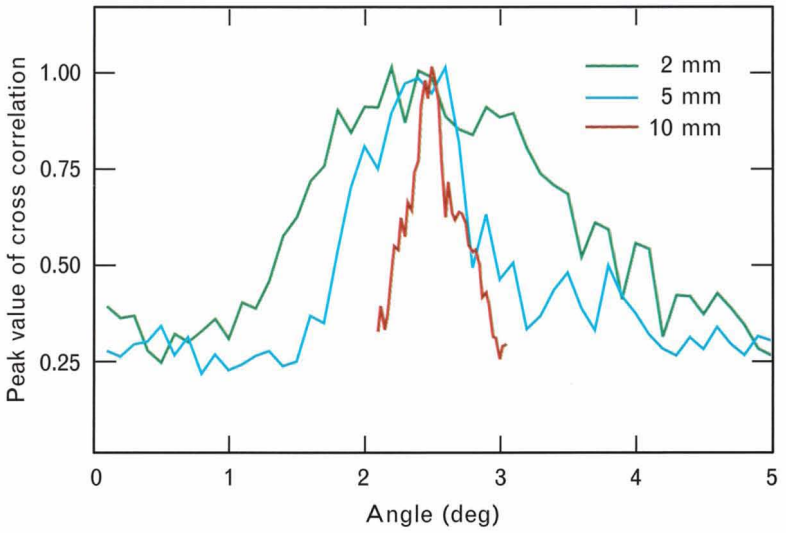

FIGURE 48. Peak value of the cross-correlation function versus rotation angle of the fiber optic pair for three different fiber separations. As the fiber separation increases, the angular resolution for the measurement of the direction of speckle motion improves.

size in our laboratory setting. If the two fibers are lined up with the direction of speckle motion, then the same fluctuating intensity signal passes by each detector, but with a time delay equal to the time that it takes for a point in the speckle pattern to move between the fibers. The cross correlation of the signals from these two fibers contains a large peak with an offset value equal to this time delay. We determine the direction of speckle motion by rotating the fibers until we find the rotation angle that produces the cross correlation with the largest peak value.

Figure 48 illustrates the dependence of the peak of the cross-correlation function on the rotation angle for three different fiber separations. Note that the width of these curves decreases as the fiber separation increases. Hence the angular resolution of the measurements improves for larger separations. Figure 48 illustrates an angular resolution of better than ±0.1° for the 10-mm fiber separation. For a real-time system, we would need a feedback control system to search for, and track, the cross-correlation peak and to optimize the resolution. We could eliminate the need for large rotations of the detector pair by arranging detectors in a ring configuration and cross-correlating the intensity signals from various detector pairs.

Angular Dynamics of Free-Body Motion

A potential application of speckle tracking is the extraction of the angular dynamics of a torque-free rigid body. This type of motion is exhibited by a rotating object in space not being acted on by any internal or external torques. The equations of motion for this situation are well known [54]. Essentially, the motion consists of spin, precession, nutation, and wobble. A general rigid body can be described by its moments of inertia around three principal axes. If the body is set spinning around one of these principal axes, then it will keep spinning around that axis as long as no torques act on it. This motion consists entirely of spin, as depicted in Figure 42. If the body rotates about an axis other than a principal axis, however, then the motion evolves over time.

The simplest type of time evolution occurs for a body whose mass distribution has rotational symmetry, e.g., a cone. For a rotationally symmetric body, one of the principal axes lies along the axis of symmetry. The other two axes lie in a plane that is perpendicular to this axis and passes through the center of mass; because of rotational symmetry, any two orthogonal axes lying in this plane will serve as principal axes. Let us denote the moment of inertia around the

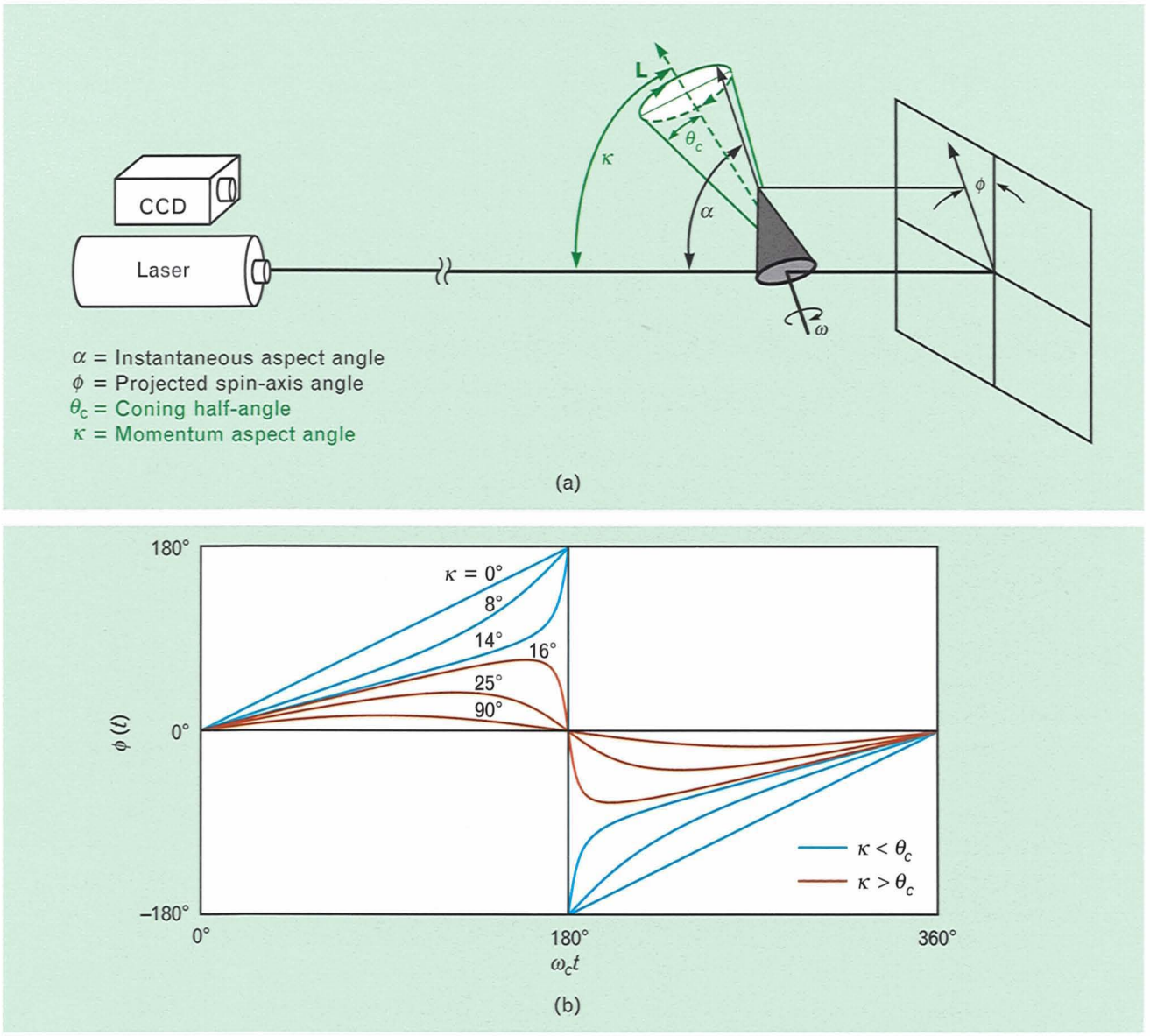

FIGURE 49. Angular dynamics for a rotationally symmetric torque-free rigid body: (a) spinning and precessing body with angular momentum **L**, coning half-angle θ_c, momentum aspect angle κ, instantaneous aspect angle α, and angular velocity of spin ω; (b) time evolution of the projected spin axis ϕ for $\theta_c = 15°$ and various values of κ ranging between 0° and 90°.

axis of symmetry by I_3 and the moment of inertia around the other two axes as $I = I_1 = I_2$. If the cone is set spinning around an axis close to the axis of symmetry, then the spin axis precesses around the angular momentum vector **L** with a cone half-angle θ_c, as shown in Figure 49(a). We denote the angle between the angular momentum vector and the radar line of sight as κ and the instantaneous aspect angle between the axis of the cone and the radar line of sight as α. The projected spin axis ϕ obeys the equation

$$\phi(t) = \phi_0 + \cot^{-1}\left[\frac{\cos\kappa\cos(\omega_c t + \phi_c) + \sin\kappa\dfrac{I\cot\theta_c + I_3\tan\theta_c}{I - I_3}}{\sin(\omega_c t + \phi_c)}\right], \tag{86}$$

where ϕ_c and ϕ_0 are phase offsets in the abscissa and

FIGURE 50. Ferris-wheel target assembly for simulating spin and precession.

ordinate, respectively, and $\omega_c = |\mathbf{L}|/I$ is the angular velocity of the precessional, or coning, motion.

The ratio between the spin rate and the precession rate is

$$\frac{\omega}{\omega_c} = \cos\theta_c \frac{I - I_3}{I_3}.$$

As the ratio ω/ω_c increases, the instantaneous spin axis aligns with the axis of symmetry and Equation 86 can be approximated as

$$\phi(t) = \cot^{-1}\left[\frac{\cos\kappa\cos(\omega_c t) + \sin\kappa\cot\theta_c}{\sin(\omega_c t)}\right], \quad (87)$$

where we have also set the phase offsets ϕ_c and ϕ_0 to zero. We plot Equation 87 in Figure 49(b) for a fixed value of $\theta_c = 15°$ and for values of κ ranging from 0° to 90°. This graph illustrates the possible shape permutations. Of special interest are the distinctly different shapes when the laser is located inside the precession cone $\kappa < \theta_c$ (blue lines) and when the laser is located outside the precession cone $\kappa > \theta_c$ (red lines). In the first case ϕ varies over a full 360°, while in the second case ϕ oscillates around the projected angular momentum vector. This distinction is in contrast with microwave radar measurements of angular target dynamics, in which the two angles κ and θ_c cannot be differentiated based on aspect-angle measurements alone.

We can estimate the parameters κ and θ_c by measuring the projected spin-axis angle ϕ over at least one precession period, and then fitting the data to Equation 87 [23]. More information about target dynamics could be obtained by measuring variations in speckle speed in addition to the time dependence of ϕ. Figure 50 shows a mechanical device (known as the "Ferris wheel") for simulating spin and precession in the laboratory. This device has two motorized rotation stages; one stage spins the target around its axis and the other rotates the target assembly around the ring. We can set the device for any combination of the momentum aspect angle (by rotating the base plate of the Ferris wheel) and the coning half-angle (by using an additional rotation stage to set the axis of the target with respect to the axis of the Ferris wheel).

If an object is not rotationally symmetric and the two moments of inertia I_1 and I_2 are unequal, then nutation occurs in addition to spin and precession. Nutation is an oscillation in the coning half-angle at twice the spin frequency. Figure 51 is a photograph of an instrument we constructed for simulating nutation. This instrument is based on a geometrical construction, known as the *Poinsot construction*, that forms an exact solution of the torque-free rigid-body problem [55]. We use this device in speckle-tracking measurements to study the precision to which angular dynamics can be determined.

Wobble, the final type of motion, arises when the geometrical axis of symmetry does not line up with the principal moment of inertia because of some asymmetry in the mass distribution. This motion occurs at the spin frequency and can be simulated by tilting the geometrical axis of the target in Figures 50 and 51 with respect to the spin axis. When wobble occurs, the motion about a principal axis can still be completely described by the three types of motion—spin, precession, and nutation. Wobble refers to the motion of a point on the surface of the body that occurs

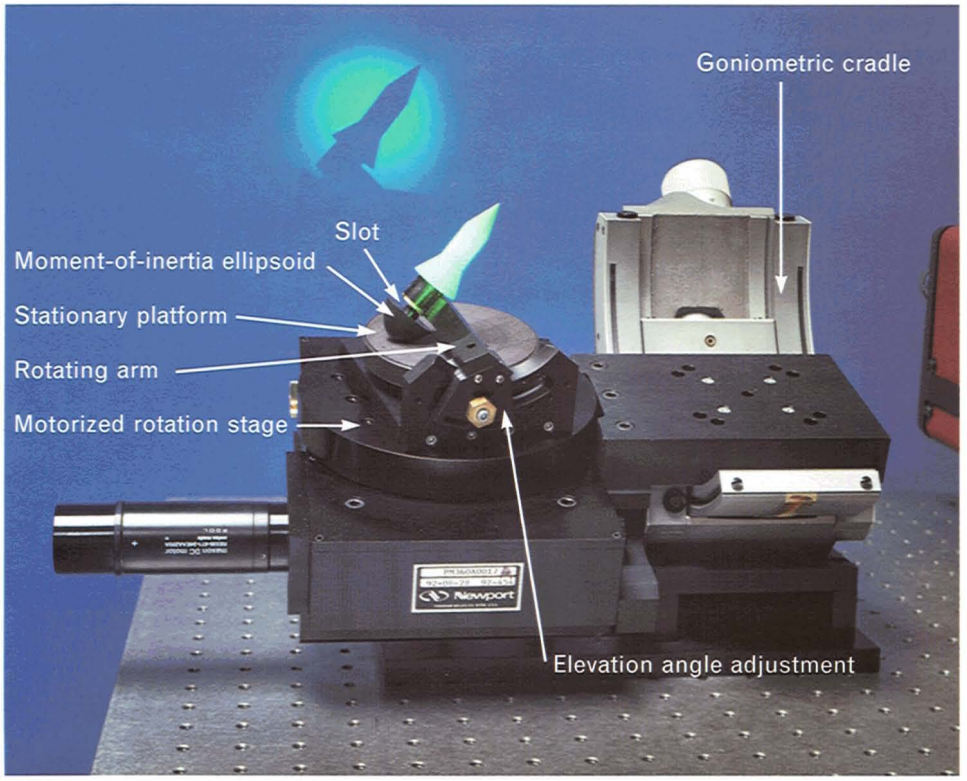

FIGURE 51. Motion simulator for producing spin, precession, and nutation with only one drive motor. The goniometric cradle sets the momentum aspect angle κ. Raising or lowering the stationary platform adjusts the mean value of the coning half-angle θ_C. The elevation angle of the rotating-arm assembly must be adjusted to compensate for the change in height to keep the mean value of θ_C near the middle region of the slot. As the motorized stage rotates, the moment-of-inertia ellipsoid rolls on the stationary platform. The platform is magnetic to keep the ellipsoid from slipping as it rolls. The slot constrains the rotation axis of the ellipsoid to move vertically, while keeping the ellipsoid in contact with the stationary platform, which produces a bobbing motion, or nutation. The center of the ellipsoid coincides with the center of a spherical bearing. A different ellipsoid is required for each set of principal-moment-of-inertia ratios.

because the axis of symmetry does not line up with the principal axis.

For simplicity, we have assumed a monostatic radar configuration in our discussion of speckle tracking. More information is available, however, if detector arrays are located at more than one position in space. For example, we could then combine the separate measurements of the projected spin axis to calculate the actual spin axis. As with wavelength decorrelation, speckle tracking is well suited to potential applications in machine vision, robotics, and metrology. Speckle tracking is especially useful for measuring small changes in angle and for characterizing the relative angular motion between two objects.

Summary

We have developed new techniques for using laser-speckle intensity patterns to determine the size, shape, surface-scattering properties, and angular dynamics of a target to a higher degree of resolution than previously attainable. In the wavelength-decorrelation technique we measure the fluctuations in the speckle intensity caused by changing the laser frequency, and we analyze these fluctuations to determine the range-resolved laser radar cross section $U(z)$ of the target. The functional form of $U(z)$ is directly related to the target's size and shape as well as the angular-scattering distribution of its surface materials. In the laboratory

we take advantage of the large tuning range of the Ti:sapphire laser to achieve submillimeter range resolutions. Wavelength decorrelation can be implemented by using direct detection, coherent detection, or wavefront sensing. With direct detection, additional signal processing such as bispectral analysis is necessary to recover the Fourier phase of $U(z)$.

Mathematically, wavelength decorrelation resembles imaging correlography, which resolves the target in cross range by utilizing the spatial structure of the speckle pattern to form two-dimensional target images (similar to those obtained from a conventional telescope). Imaging correlography, however, offers the potential for higher spatial resolutions of distant targets because detector arrays with large baselines can be used when sampling the speckle pattern.

The speckle-tracking technique relates the motion of the speckle pattern at the receiver to the motion of the target, which allows us to measure a target's projected spin axis to an accuracy better than ±0.1°. We determine the target's angular dynamics by observing how the projected spin axis varies with time. Speckle streaking and temporal cross correlation are convenient methods for measuring speckle motion.

Plans are currently underway to adapt this proven laser-speckle technology to actual dynamic situations and to move toward applications outside the laboratory. These plans include the development of a fast frequency-scanning laser, a customized detector array, and a parallel processor engineered for real-time digital signal processing.

Acknowledgments

This work was sponsored by the U.S. Army Space and Strategic Defense Command. The authors acknowledge Peter A. Lo for implementing the bispectral-analysis technique on the computer, Joseph A. Heanue for his earlier work on reflective tomography, Thomas M. Smith for an introduction to laser radar cross sections, and Suzanne S. Ourfalian for laboratory support. The authors also thank Kent R. Edwards, Hsiao-hua K. Burke, and Charles K. Meins, Jr., of the Signature Studies and Analysis group, and William Z. Lemnios, Wade M. Kornegay, and John A. Tabaczynski of the Radar Measurements division for their ongoing support of the Laser Speckle Laboratory.

REFERENCES

1. "ALCOR Data Users and Radar Operators Manual, K_a and W Bands," MIT Lincoln Laboratory Manual 134 (1 Aug. 1988).
2. L.I. Goldfischer, "Autocorrelation Function and Power Spectral Density of Laser-Produced Speckle Patterns," *J. Opt. Soc. Am.* **55**, 247 (1965).
3. P.S. Idell, J.R. Fienup, and R.S. Goodman, "Image Synthesis from Nonimaged Laser-Speckle Patterns," *Opt. Lett.* **12**, 858 (1987).
4. D.G. Voelz, J.D. Gonglewski, and P.S. Idell, "Image Synthesis from Nonimaged Laser-Speckle Patterns: Comparison of Theory, Computer Simulation, and Laboratory Results," *Appl. Opt.* **30**, 3333 (1991).
5. J.N. Cederquist, J.R. Fienup, and J.C. Marron, "High Resolution Imaging by Phase Retrieval and Discrimination Using Speckle, Vol. 1," Final Report No. 201600-11-F, Environmental Research Institute of Michigan, Ann Arbor, MI (1989).
6. N. George, "The Wavelength Sensitivity of Back-Scattering," *Opt. Commun.* **16**, 328 (1976).
7. N. George, "Speckle from Rough, Moving Objects," *J. Opt. Soc. Am.* **66**, 1182 (1976).
8. N. George, A.C. Livanos, J.A. Roth, and C.H. Papas, "Remote Sensing of Large Roughened Spheres," *Opt. Acta* **23**, 367 (1976).
9. N. George, "Speckle," *SPIE* **243**, 124 (1980).
10. L.G. Shirley, "Speckle Decorrelation Techniques for Remote Sensing of Rough Objects," in *OSA Annual Mtg. Tech. Dig.* **18** (Optical Society of America, Washington, 1989), p. 208.
11. L.G. Shirley, "Speckle Decorrelation," *Proc. IRIS Targets, Backgrounds, and Discrimination* **1**, 123 (1990).
12. D.J. Schertler and N. George, "Comparison of Wavelength Scanning and Pulse Echo Systems in Remote Sensing," *Opt. Commun.* 77, 91 (1990).
13. L.G. Shirley, "Remote Sensing of Object Shape Using a Wavelength Scanning Laser Radar," in *OSA Annual Mtg. Tech. Dig.* **17** (Optical Society of America, Washington, 1991), p. 154.
14. L.G. Shirley and J.R. Vivilecchia, "Target Characterization Using a Wavelength Scanning Laser Radar," *Proc. Second Annual Automatic Target Recognizer System and Technology Conf.* (1992).
15. J.C. Marron and K.S. Schroeder, "Three-Dimensional Lensless Imaging Using Laser Frequency Diversity," *Appl. Opt.* **31**, 255 (1992).
16. J.C. Marron and T.J. Schulz, "Three-Dimensional, Fine-Resolution Imaging Using Laser Frequency Diversity," *Opt. Lett.* **17**, 285 (1992).
17. J.C. Marron, "Wavelength Decorrelation of Laser Speckle from Three-Dimensional Diffuse Objects," *Opt. Commun.* **88**, 305 (1992).
18. L.G. Shirley and P.A. Lo, "Bispectral Analysis of the Wavelength Dependence of Laser Speckle: Application to Remote Sensing of Object Shape," in *Signal Recovery and Synthesis IV Tech. Dig.* **11** (Optical Society of America, Washington, 1992), p. 17.
19. L.G. Shirley and P.A. Lo, "Bispectral Analysis of the Wavelength Dependence of Speckle: Remote Sensing of Object Shape," accepted for publication in *Opt. Soc. Am. A.* **10** (1993).
20. H.J. Tiziani, "A Study of the Use of Laser Speckle to Measure Small Tilts of Optically Rough Surfaces Accurately," *Opt. Commun.* **5**, 271, (1972).

21. J.H. Churnside, "Speckle from a Rotating Diffuse Object," *J. Opt. Soc. Am.* **72**, 1464 (1982).
22. A. Hayashi, and Y. Kitagawa, "High-Resolution Rotation-Angle Measurement of a Cylinder Using Speckle Displacement Detection," *Appl. Opt.* **22**, 3520 (1983).
23. L.G. Shirley, G.R. Hallerman, and H.C. Payson, "Target Dynamics from Speckle Motion," MIT Lincoln Laboratory video, Apr. 1991.
24. L.G. Shirley, H.C. Payson, and G.R. Hallerman, "High-Precision Target Dynamics Using a Speckle-Tracking Laser Radar," in *OSA Annual Mtg. Tech. Dig.* **17** (Optical Society of America, Washington, 1991), p. 142.
25. J.W. Goodman, *Introduction to Fourier Optics* (McGraw-Hill, New York, 1968).
26. J.D. Gaskill, *Linear Systems, Fourier Transforms, and Optics* (Wiley, New York, 1978).
27. L.G. Shirley and N. George, "Diffuser Radiation Patterns over a Large Dynamic Range. 1: Strong Diffusers," *Appl. Opt.* **27**, 1850 (1988).
28. C.E. Halford, W.L. Gamble, and N. George, "Experimental Investigation of the Longitudinal Characteristics of Laser Speckle," *Opt. Eng.* **26**, 1263 (1987).
29. F.E. Nicodemus, "Reflectance Nomenclature and Directional Reflectance and Emissivity," *Appl. Opt.* **9**, 1474 (1970).
30. F.E. Nicodemus, J.C. Richmond, J.J. Hsia, I.W. Ginsberg, and T. Limperis, *Geometrical Considerations and Nomenclature for Reflectance* (U.S. Government, Washington, 1977).
31. G.T. Ruck, D.E. Barrick, W.D. Stuart, and C.K. Krichbaum, *Radar Cross Section Handbook, Vols. 1–2* (Plenum Press, New York, 1979).
32. W.R. Rambauske and R.R. Gruenzel, "Distribution of Diffuse Optical Reflection around Some Stereometric Surfaces," *J. Opt. Soc. Am.* **55**, 315 (1965).
33. J.C. Dainty, ed., *Laser Speckle and Related Phenomena* (Springer-Verlag, Berlin, 1984).
34. J.W. Goodman, *Statistical Optics* (Wiley, New York, 1985).
35. W.F. McGee, "Complex Gaussian Noise Moments," *IEEE Trans. Inform. Theory* **17**, 149 (1971).
36. L.G. Shirley and N. George, "Speckle from a Cascade of Two Thin Diffusers," *J. Opt. Soc. Am. A* **6**, 765 (1989) .
37 I.S. Reed, "On a Moment Theorem for Complex Gaussian Processes," *IRE Tran. Inform. Theory* **8**, 194 (1962).
38. A.L. Kachelmyer, "Range-Doppler Imaging with a Laser Radar," *Lincoln Lab J.* **3**, 87 (1990).
39. J.R. Fienup, "Reconstruction of an Object from the Modulus of Its Fourier Transform," *Opt. Lett.* **3**, 27 (1978).
40. H. Stark, ed., *Image Recovery: Theory and Application* (Academic Press, New York, 1987).
41. C.L. Nikias and M.R. Raghuveer, "Bispectrum Estimation: A Digital Signal Processing Framework," *Proc. IEEE* **75**, 869 (1987).
42. J.M. Mendel, "Tutorial on Higher-Order Statistics (Spectra) in Signal Processing and System Theory: Theoretical Results and Some Applications," *Proc. IEEE* **79**, 278 (1991).
43. A.W. Lohmann and B. Wirnitzer, "Triple Correlations," *Proc. IEEE* **72**, 889 (1984).
44. H. Bartelt, A.W. Lohmann, and B. Wirnitzer, "Phase and Amplitude Recovery from Bispectra," *Appl. Opt.* **23**, 3121 (1984).
45. C.A. Haniff, "Least-Squares Fourier Phase Estimation from Modulo 2π Bispectrum Phase," *J. Opt. Soc. Am. A* **8**, 134 (1991).
46. H.H. Barrett and W. Swindell, *Radiological Imaging, Vols. 1–2* (Academic Press, New York, 1981).
47. C.K. Chan, and N.H. Farhat, "Frequency Swept Tomographic Imaging of Three-Dimensional Perfectly Conducting Objects," *IEEE Trans. Antennas Propag.* **29**, 312 (1981).
48. F.K. Knight, S.R. Kulkarni, R.M. Marino, and J.K. Parker, "Tomographic Techniques Applied to Laser Radar Reflective Measurements," *Linc. Lab. J.* **2**, 143 (1989).
49. F.K. Knight, D.I. Klick, D.P. Ryan-Howard, and J.R. Theriault, Jr., "Visible Laser Radar: Range Tomography and Angle-Angle-Range Detection," *Opt. Eng.* **30**, 55 (1991).
50. B.T. Binder, *Laser Radar Tomography: The Effects of Speckle*, Ph.D. thesis, MIT, Cambridge, MA (1991).
51. L.G. Shirley, G.R. Hallerman, and J.R. Vivilecchia, "Determination of Angular Surface Scattering from Measurements of Range-Resolved Laser Radar Cross Section," in *OSA Annual Mtg. Tech. Dig.* **23** (Optical Society of America, Washington, 1992), p. 205.
52. J.W. Hardy, "Active Optics: A New Technology for the Control of Light," *Proc. IEEE* **66**, 651 (1978).
53. H.T. Barclay, P.H. Malyak, W.H. McGonagle, R.K. Reich, G.S. Rowe, and J.C. Twichell, "The SWAT Wavefront Sensor," *Lincoln Lab. J.* **5**, 115, (1992).
54. J. Wittenburg, *Dynamics of Systems of Rigid Bodies* (B.G. Teubner, Stuttgart, 1977).
55. H. Goldstein, *Classical Mechanics* (Addison-Wesley, Reading, MA, 1959).

LYLE G. SHIRLEY
is a staff member in the Signature Studies and Analysis group. His primary research interests are in wave phenomena, random processes, and signal processing. Lyle was born and raised in Idaho. After completing the first year of his undergraduate studies, he served a two-year mission in Austria for The Church of Jesus Christ of Latter-day Saints. He received an A.S. degree from Ricks College in 1978 and a B.S. degree in physics from Brigham Young University in 1980. He completed an M.S. degree in physics from Brigham Young University in 1984 (with a thesis on acoustics) and a Ph.D. in optics from the University of Rochester in 1988. Lyle then joined Lincoln Laboratory, where he began an investigation of the information that laser speckle carries about the scattering object. In 1989 he proposed setting up an optics laboratory for developing speckle-based discrimination and imaging techniques. The Laser Speckle Laboratory became operational in October of 1990. Since then, Lyle has divided his time between planning and directing the experimental research and continuing the theoretical analysis. He and his wife Laurelyn have five children.

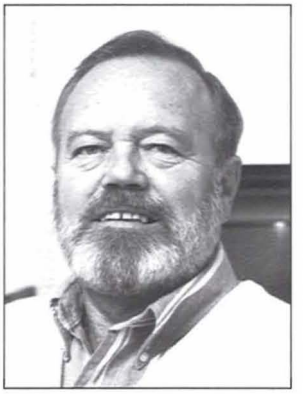

EMORY D. ARIEL
is an assistant staff member in the Signature Studies and Analysis group. His research interests are in optomechanical devices. He received a B.S. degree in mechanical engineering from Northeastern University, and he has been at Lincoln Laboratory since 1959. His personal interests are in ballroom dancing, western dancing, sport fishing, boating, and fun times with his grandchildren.

GREGORY R. HALLERMAN
is an assistant staff member in the Signature Studies and Analysis group. His research has been in the areas of speckle-discrimination technology and reflectance spectroscopy. Greg joined Lincoln Laboratory in 1990. He received a B.S. degree in optics from the University of Rochester, and is currently working toward a master's degree in electrooptics at Tufts University. As an undergraduate, he worked for the University of Rochester's Laboratory for Laser Energetics, where he helped develop liquid crystal polarizer/isolators and liquid crystal waveplates. In his spare time, Greg competes in track and field, and he has won New York state championships in the decathlon and pentathlon.

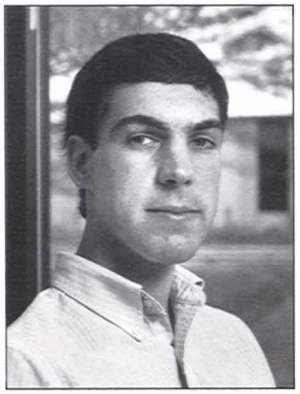

HAROLD C. PAYSON
is an assistant staff member in the Signature Studies and Analysis group. When he joined Lincoln Laboratory in 1988 his initial work involved celestial mechanics. Since the start of the Laser Speckle Laboratory, his research in speckle techniques for discrimination has led him into areas such as speckle tracking, computer-aided tomography, and three-dimensional computer visualization. He received a B.S. degree in physics from Rensselaer Polytechnic Institute (RPI) in 1988. While at RPI he spent one year studying at the Swiss Federal Institute of Technology in Zürich, Switzerland, where he concentrated in high-energy physics and spent a summer working at CERN on the vertex detector of the L3 project of LEP. Since joining Lincoln Laboratory he has taken graduate courses in electrooptics at Tufts University.

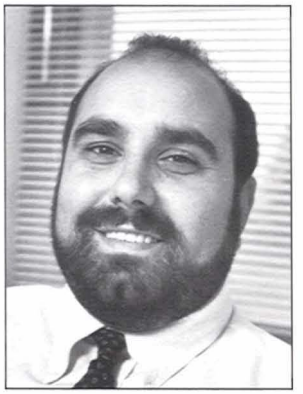

JOHN R. VIVILECCHIA
is an assistant staff member with the Signature Studies and Analysis group. He received his B.S. degree in applied physics with a minor in optics from the University of Lowell. He is currently taking graduate courses at Tufts University, where he is working toward a master's degree in electro-optical engineering. His current area of research is in exploring the use of laser speckle as a discrimination tool. Previously, he worked with the High Energy Laser Beam Control and Propagation Group at Lincoln Laboratory, performing research in the field of adaptive optics. He has been at Lincoln Laboratory since 1987. A lifelong resident of Massachusetts, John enjoys outdoor activities, boating, and travel in his spare time.